

CHARACTERISING PATIENT SPECIFIC SOFT TISSUE DEFORMATION IN THE RESIDUAL LIMB UNDER COMPRESSIVE LOADS

BY

MAHAMANDIGE KAUSHINI SANKALANI MENDIS

STUDENT ID: 2224860

SUPERVISED BY:

DR. RAMI AL-DIRINI AND DR. DAVID HOBBS

THESIS SUBMITTED TO THE COLLEGE OF SCIENCE AND ENGINEERING IN PARTIAL
FULFILMENT OF THE REQUIREMENTS FOR THE DEGREE OF MASTER OF
ENGINEERING (BIOMEDICAL) AT FLINDERS UNIVERSITY, ADELAIDE, AUSTRALIA

DECLARATION

I hereby declare that I am the sole author of this thesis and that neither any part of this thesis nor the whole of the thesis has been submitted for a degree or diploma to any other university or institution.

I declare that this work was carried out under the supervision of Dr. Rami Al-Dirini and Dr. David Hobbs as part of fulfillment of the requirements of the Master of Engineering (Biomedical) degree.

I declare that to the best of my knowledge, my thesis does not intrude upon anyone's copyrights or violate any proprietary rights. Any ideas, techniques, or any other material from the work of other people included in my thesis, published or otherwise, are fully acknowledged in accordance with the standard referencing practices.

I declare that this is a true copy of my thesis, including the final revisions as approved by my supervisors.

Mahamandige Kaushini Sankalani Mendis

College of Science and Engineering

Flinders University

EXECUTIVE SUMMARY

A prosthetic socket can be considered as the primary link between the prosthesis and the residual limb in a lower limb amputated patient. Within the first two years post-amputation, the residual limb soft tissues tend to change in the aspects of shape, volume, composition, and sensitivity due to environmental, mechanical, and surgical factors. As these changes could occur within a single day, or within several months, a single mechanical design is not capable of interpreting the high rate of change of the stump. Thus, patients tend to wear temporary sockets within this time period. Patients wear a permanent socket at a later stage following amputation when the stump reaches its maturity. Even though the matured residual limb continues to change due to fluid movements and temperature variations, a single mechanical design can cope up with the low rate of change of the stump. The project considered the patient-specific soft tissue deformations at the matured stage of the residual limb under compressive loads.

The elevated stresses and strains caused by imperfect permanent socket fittings contribute to a range of short- and long-term complications and affect patient satisfaction in physical, mental, and financial aspects. The project intends to improve the current socket designing and manufacturing process, which depends on prosthetists' experience and unreliable feedback from patients towards an engineering-driven framework to benefit the patient's health, healthcare system and the economy.

Biomechanical modelling has been used over the past two decades to model the residual limb soft tissue mechanics in order to eliminate the ill-fitting sockets. The efficacy and fidelity of biomechanical models require accurate information on the geometry and material properties of soft tissues. The main limitation of the previous work was the consideration of literature reported material properties; most of the researchers were leaned towards assuming linear, elastic, isotropic and homogenous material properties for the residual limb soft tissues. Hence, the project's aim was to estimate patient specific soft tissue deformations of the residual limb employing medical image data acquired while performing quasi-static loading experiments, which could assist in estimating patient specific material properties in the future.

The project considered the magnetic resonance imaging (MRI) scans related to three patients where each patient had to undergo a series of uniaxial quasi-static compression tests. The MRI scans were obtained using an MRI compatible sphygmomanometer (Cone Instruments, USA) which covered the patient's residual limb at 0 *mmHg*, 30 *mmHg*, 60 *mmHg* and 100 *mmHg* pressures, respectively. The MRI scans were segmented through Simpleware ScanIP (Synopsys, California, USA) to obtain surface and solid geometries of the uncompressed and the compressed states of the residual limb.

Rigid iterative closest point (ICP) algorithms were performed to register the uncompressed to each of the compressed surface geometries of the residual limb. Non-rigid ICP was then used to calculate soft tissue deformation at the entire residual limb surface for each of the compressed states. The area in contact with the sphygmomanometer was extracted to derive the force applied at each compressed state. Finally, the patient specific soft tissue deformations of the residual limb were characterized by fitting piecewise linear models to force-deformation data acquired for each patient. All data processing were performed using MATLAB (MathWorks, Massachusetts, USA).

The force-deflection plots indicated unique shapes for each patient confirming the discrepancies between the soft tissue deformations between patients. The obtained soft tissue deformations could aid substantially in biomechanical modelling of residual limb soft tissues. The study anticipates developing accurate computational models of the mechanical contact between the residual limb and encasing socket. Such models can aid current socket design and customization process in an effort to reduce the risk of tissue injury, to lessen the time, materials and workforce required for design and fabrication of a best-fit prosthetic socket, and to improve patient satisfaction rates. The study anticipates employing more patients in the future to understand the variability within the patient population.

TABLE OF CONTENTS

Declaration	I
Executive Summary	II
List of Figures	VII
List of Tables	XI
Introduction	1
Research Background	1
Lower Limb Amputation	1
Lower Limb Prosthetics	2
Socket	11
Research Problem	15
Research Aim	15
Overview of the Research Methodology	15
Thesis Outline	17
Literature Review	18
Residual Limb	18
Lower Limb Biomechanics and Soft Tissue Deformation	18
Material Properties of Soft Tissues in the Residual Limb	19

Finite Element Method and Material Properties of Soft Tissues in the Residual Limb	20
Material Properties of Soft Tissues in the Residual Limb	21
Isotropic and Linear Elastic Material Properties	21
Hyperelastic Material Properties	25
Method	32
Compression Test and Magnetic Resonance Imaging	32
Compression Test	32
Magnetic Resonance Imaging	33
Generation of Surface and Solid Geometries	33
Iterative Closest Point Algorithm	40
Rigid ICP Registration	40
Non-rigid ICP Registration	46
Deformation Field	49
Area of the Deformation Field	52
Results	54
Soft Tissue Deformations of the First Patient’s Residual Limb Under Compressive Loads	54
Soft Tissue Deformations of the Second Patient’s Residual Limb Under Compressive Loads	60
Soft Tissue Deformations of the Third Patient’s Residual Limb Under Compressive Loads	65

Discussion	70
Conclusion	78
References	79
Appendices	87
Appendix 1	87
Appendix 2	88
Appendix 3	88
Appendix 4	89
Appendix 5	90
Appendix 6	91
Appendix 7	91
Appendix 8	92
Appendix 9	93

LIST OF FIGURES

Figure 1: Manual Steps of the Socket Manufacturing Process; A – Bandaging Plaster on to the Stump; B – Reducing Positive Mold Circumference; C – Marking the Critical Zones; D – Manipulating the Critical Zones (Colombo et al. 2013)	8
Figure 2: Socket Development Process	9
Figure 3: Transtibial and Transfemoral Socket Types (Paternò et al. 2018)	12
Figure 4: PTB Sockets (Physiopedia Contributors, 2020)	13
Figure 5: Process of Achieving Soft Tissue Deformations from MRI Scans	16
Figure 6: Internal Pressure and Relative Deformation vs Time (Gefen 2009)	18
Figure 7: Stress-Strain Curve for Linear Elastic Material (Kelly 2013)	21
Figure 8: Stress-Strain Curve for Hyperelastic Material (Omidi et al. 2014)	25
Figure 9: Schematic Diagram of Obtaining Medical Images (Cone Instruments 2021; Foisneau-Lottin et al. 2003)	32
Figure 10: MRI visualization on Simpleware ScanIP	34
Figure 11: Defined Masks on Simpleware ScanIP	35
Figure 12: Defining the Bone using the Paint Tool	36
Figure 13: Filling the Bone using the Flood Fill Tool	36
Figure 14: Segmentation before using the 3D Wrap Filter	37
Figure 15: Flesh and Bone Geometries Resulted from Segmentation.....	38

Figure 16: Bone Geometries Resulted from Segmentation	38
Figure 17: Flesh Layer After Performing Boolean Operation	39
Figure 18: Schematic Diagram of Rigid ICP Registration on Tibia	41
Figure 19: Tibia before Rigid ICP Registration - Source Tibia	43
Figure 20: Tibia after Rigid ICP Registration - Realigned Tibia	43
Figure 21: Rigid ICP Registration on Tibia	44
Figure 22: Flesh before Rigid ICP Registration - Source Flesh	45
Figure 23: Flesh after Rigid ICP Registration - Realigned Flesh	45
Figure 24: Realignment of Flesh through Rigid ICP Registration.....	46
Figure 25: Schematic of Non-rigid ICP Registration on Flesh	47
Figure 26: Non-rigid ICP Registration on Flesh	48
Figure 27: Registered and targetFleshV Variables with Similar Matrix Sizes	49
Figure 28: Triangle Midpoints (xq) with Interpolated Values (vq)	50
Figure 29: Triangle Midpoints (xq) with Filtered Interpolated Values (vq_n)	51
Figure 30: Filtered Triangle Midpoints (xq) with Filtered Interpolated Values (vq_n)	52
Figure 31: Maximum Soft Tissue Deflection vs Force Graph of the First Patient.....	55
Figure 32: 50 th Percentile of Soft Tissue Deflection vs Force Graph of the First Patient.....	56
Figure 33: 70 th Percentile of Soft Tissue Deflection vs Force Graph of the First Patient.....	56

Figure 34: 90th Percentile of Soft Tissue Deflection vs Force Graph of the First Patient.....57

Figure 35: 50th, 70th and 90th percentile of Soft Tissue Deformation vs Force Graph related to the First Patient58

Figure 36: The Areas of Soft Tissue Deformation related to 50th, 70th and 90th Percentile of the First Patient.....59

Figure 37: Maximum Soft Tissue Deflection vs Force Graph of the Second Patient60

Figure 38: 50th Percentile of Soft Tissue Deflection vs Force Graph of the Second Patient61

Figure 39: 70th Percentile of Soft Tissue Deflection vs Force Graph of the Second Patient62

Figure 40: 90th Percentile of Soft Tissue Deflection vs Force Graph of the Second Patient62

Figure 41: 50th, 70th and 90th percentile of Soft Tissue Deformation vs Force Graph related to the Second Patient63

Figure 42: The Areas of Soft Tissue Deformation related to 50th, 70th and 90th Percentile of the Second Patient64

Figure 43: Maximum Soft Tissue Deflection vs Force Graph of the Third Patient65

Figure 44: 50th Percentile of Soft Tissue Deflection vs Force Graph of the Third Patient66

Figure 45: 70th Percentile of Soft Tissue Deflection vs Force Graph of the Third Patient67

Figure 46: 90th Percentile of Soft Tissue Deflection vs Force Graph of the Third67

Figure 47: 50th, 70th and 90th percentile of Soft Tissue Deformation vs Force Graph related to the Third Patient68

Figure 48: The Areas of Soft Tissue Deformation related to 50th, 70th and 90th Percentile of the Third Patient69

Figure 49: Maximum Soft Tissue Deflection vs Force Graph for the Three Patients71

Figure 50: 50th Percentile of Soft Tissue Deflection vs Force Graph for the Three Patients72

Figure 51: 70th Percentile of Soft Tissue Deflection vs Force Graph for the Three Patients73

Figure 52: 90th Percentile of Soft Tissue Deflection vs Force Graph for the Three Patients74

LIST OF TABLES

Table 1: Lower Extremity Amputation Levels (Bastas 2019).....	4
Table 2: Types of Alignments in Prosthesis Fabrication Process (Ikeda et al. 2012)	10
Table 3: Material properties and associated constituents of Several Soft Tissue Types (Fung 2013; Silver, Christiansen & Buntin 1989; Woo, Gomez & Akeson 1985).....	19
Table 4: Material Properties of Soft Tissues in the Residual Limb - Isotropic and Linear Elastic..	23
Table 5: Material Properties of Soft Tissues in the Residual Limb - Hyperelastic.....	28
Table 6: 50th, 70th and 90th percentile of Soft Tissue Deformation related to the First Patient	55
Table 7: 50th, 70th and 90th percentile of Soft Tissue Deformation related to the Second Patient	61
Table 8: 50th, 70th and 90th percentile of Soft Tissue Deformation related to the Third Patient	66

INTRODUCTION

RESEARCH BACKGROUND

LOWER LIMB AMPUTATION

DEFINITION

Lower limb amputation refers to the surgical procedure which removes a single part or multiple parts of the lower limb (Esquenazi & Yoo 2016). It remains a key threat towards the activities of daily living as it majorly impacts a person's ability to walk and maintaining body balance.

INCIDENCE OF LOWER LIMB AMPUTATION AND PROSTHETIC USAGE

Lower limb amputations accounts for more than four fifths of total amputations. While the prevalence of the lower limb amputations has been reported high across the globe, United States reports over 150,000 lower limb amputations yearly (Dillingham Pezzin & Shore 2005; Molina & Faulk 2020). More than 8000 annual lower limb amputations have been reported from Australia, which approximates to a lost lower limb each hour by an Australian (Dillion et al. 2017). The most common lower limb amputation occurs at the transtibial level (below the knee, between the ankle joint and the knee joint) and corresponds to more than 50% of the amputee population. Amputations occur at the transfemoral level (above the knee, between the knee joint and the hip joint) approximates 30% of the amputee population (Edwards 2002).

Several studies have reported diminishing major lower limb amputation rates and rising minor lower limb amputation rates. Improvements in preventive health care structures and novel surgical and non-surgical corrective techniques can be identified as the key drivers supporting the shift from major to minor amputations (Behrendt et al. 2018; Kröger et al. 2017; May et al. 2016).

It has been reported that a significant number of patients with lower limb amputations do not use a prosthesis regardless of its advantages. The recorded rates of prosthesis usage in patients with lower limb amputation deviate from 49% (Schoppen et al. 2003) to 95% (Pezzin et al. 2004).

CAUSES FOR LOWER LIMB AMPUTATION

Vascular diseases, injuries, congenital abnormalities, infections, gangrene, and tumor removing surgeries has been identified as the prominent causes for lower limb amputations (Cowie et al. 2010; Krajbich et al. 2018).

Patients with congenital lower limb deficiency, infections, gangrene, and cancer represent the least amount of the total lower limb amputee population. Partial or complete loss of the fibula has been identified as the most common congenital abnormality in the lower limbs. Lower limb amputations due to injuries account for approximately 40% of the total lower limb amputations, which generally occur in younger people between the ages of 21 and 50. The leading cause of lower limb amputations is vascular diseases, particularly atherosclerosis in patients with diabetes which corresponds to over 50% of lower limb amputated patients (Edwards 2002; Ziegler-Graham et al. 2008).

LOWER LIMB PROSTHETICS

DEFINITION

An artificial substitution for a missing part of the body is known as a prosthesis. Thus, a prosthesis which replaces any part of the lower limb could be identified as a lower limb prosthesis. Lower limb prosthesis consists of artificial components that are capable of replacing the hip, thigh, knee, leg, ankle, and foot.

PRE-PROSTHETIC TRAINING AND PROSTHETIC EVALUATION

The patient's history would be evaluated after amputation to decide the patient's candidateship for a lower limb prosthesis. Subsequently, the patient's physical and mental status are evaluated

to determine the suitable prosthetic prescription. The assessment includes the patient's cognitive skills, function of the upper limbs and the opposite lower limb, residual limb characteristics and body weight.

The patient with the lower limb amputation would be then classified to a particular functional level (K level) according to the patient's potential for prosthetic ambulation. The potential candidates are prepared in the pre-prosthetic training period through performing day to day activities, shaping of the residual limb, and learning about muscle strengthening, pain management and skin care (Orendurff et al. 2016; Andrews, Nanosand & Hoskin 2017).

TEMPORARY AND PERMANENT PROSTHESIS

In the early stages of the healing process after the amputation surgery, ace wraps are used as a support to hold bandages and splints in place. Consequently, an elastic shrinker (an elastic sock) is used to regulate swelling, promote healing, and assist in shrinking and shaping the residual limb. A rigid protective device is used in this stage to protect the patient's residual limb.

The initial prosthetic fitting is referred to as preparatory or temporary prosthesis. Within the initial years post-amputation, the residual limb soft tissues tend to change in the aspects of volume, shape, composition, and sensitivity due to environmental, mechanical, and surgical factors within a single day, or within several months. Patients wear temporary sockets within this time period, as a single mechanical design cannot account with the high rate of changes of the stump. The temporary prosthesis is designed to be strong and can be adjusted for alignment, fit and componentry.

The final prosthetic fitting is referred to as definitive or permanent prosthesis. Patients wear a permanent socket at a later stage when the stump reaches its maturity. Even though the stump continues to change due to fluid movements and temperature changes even after reaching maturity, the rate of change of the stump in this later stage is possible to be accounted through a single mechanical design.

THE PROSTHESIS PRESCRIPTION

The level of lower limb amputation determines the components required to be prescribed for the lower limb prosthesis. The Table 1 has summarized different levels of amputations related to the lower extremity.

Table 1: Lower Extremity Amputation Levels (Bastas 2019)

Foot	Partial toe	Amputation of any part of one or more toes
	Toe disarticulation	Amputation at a metatarsophalangeal joint
	Partial foot or Ray resection	Amputation of a toe and its associated metatarsal
	Transmetatarsal	Amputation at the midsection of all metatarsals
	Tarsometatarsal disarticulation or Lisfranc	Amputation of all the toes and metatarsals at the tarsometatarsal joints
	Midtarsal disarticulation or Chopart	Amputation of the forefoot at themidtarsal joint
Ankle	Ankle disarticulation or Syme	Amputation at the ankle joint which the heel pad is preserved
Leg	Long transtibial	Amputation of a lower limb below the knee including more than 50% of tibial length
	Short transtibial	Amputation of a lower limb below the knee including between 20% to 50% of tibial length
Knee	Knee disarticulation	Amputation at the knee joint
Thigh	Long transfemoral	Amputation of a lower limb above the knee including more than 60% of femoral length
	Short transfemoral	Amputation of a lower limb above the knee including between 35% to 60% of femoral length
Hip	Hip disarticulation	Amputation at the hip joint

	Hemipelvectomy		Amputation of the hemipelvis and the associated lower limb
	Hemicorporectomy Translumbar	or	Amputation of the pelvis at the L4-L5 level

COMPONENTS OF A LOWER LIMB PROSTHESIS

The components of a lower limb prosthesis depend on the level of lower limb amputation. The following components form a lower limb prosthesis (Balk et al. 2018):

1. Socket
2. Liner
3. Suspension
4. Hip, Knee, Ankle and Foot
5. Frame
6. Specialized Components

The primary link between an amputated residual limb and a prosthesis is known as a prosthetic socket. The socket should ensure the patient's ability to function comfortably and effectively under the two force systems: the weight of the body due to gravity and the forces applied to the residual limb through the socket contact (Childers & Wurdeman 2015). To accommodate the patient specific residual limb shape, nerve and skin patterns, sockets are custom-designed and manufactured.

The prosthetic liner acts as a protective layer between the residual limb skin and the socket, enhancing comfort and maintaining a more consistent fit. Liners could be classified to three main groups as TPE (Thermoplastic Elastomer) liners, silicon liners and urethane liners considering the level of softness and the level of durability (Klute, Glaister & Berge 2010).

The suspension of a lower limb prosthesis prevents the socket from falling off from the residual limb when it is moved during gait. The quality of the suspension mechanism is responsible for

improving the energy transfer between the residual limb and the socket, enhancing the prosthesis control, and reducing discomfort. The main suspension systems consist of:

- Cuffs, Straps and Belts
- Lanyard
- Self-suspending socket
- External sleeve
- Pin and lock
- Suction without a liner
- Suction with a liner
- Negative pressure
- Osseointegration

The residual limb shape and the size are the key factors that contribute to suspension prescription. Other factors include the patient's body strength, hand dexterity, eyesight, and body balance (Engstrom & Van de Ven 1999).

The prosthetic hip, knee, ankle, and foot components are capable of mimicking their respective biological functions. According to the amputation level of the patient, either a single component or combination of components are used on the patient to provide him/her a safe, symmetrical, and smooth passage during gait.

The prosthetic components are linked together using the prosthetic frame. The two key forms of prosthetic frames are named as exoskeletal and endoskeletal. The rarely used exoskeletal frame is comprised of a rigid outer lamination and a light-weight inner filler. The frequently used endoskeletal frame uses pylons to connect the prosthetic components. The pylons can be constructed from aluminum, titanium, stainless steel or any hybrid of these materials (Oleiwi & Ahmed 2016).

A prosthesis could be used with or without any specialized components. The use of cosmesis is utterly a personal choice as it does not help the functioning of a prosthesis. A cosmesis mimics

the form of a biological lower limb and could be included with freckles, veins, and hair. Microchips and artificial intelligence (AI) chips allow the prosthesis to adapt to the patient's walking speed and style in activities including hiking, jogging, and swimming.

FABRICATION OF THE LOWER LIMB PROSTHESIS

The prosthesis fabrication steps include:

1. Casting
2. Positive mold
3. Rectification
4. Assembling
5. Alignments
6. Cosmetics

The prosthesis fabrication initiates with the socket development process. The positive mold of the residual limb can be manufactured following an entirely manual (traditional) or a partly manual (partly automatic) procedure. In the traditional process, the technician measures the residual stump of the patient and bandages plaster directly on to the stump to create the negative cast. Then, the negative cast is filled with plaster to create the positive mold. The partly automatic process generates the positive mold based on both manual and CAD/CAM (Computer-Aided Design/Computer-Aided Manufacturing) systems (Colombo et al. 2013).

The positive mold is rectified corresponding to the residual stump measurements and patient's characteristics by adding and removing plaster to obtain the optimal socket fit. The rectification consists of three key stages:

1. Reducing the circumference of the positive mold according to the residual stump conditions.
2. Identifying and marking the critical zones.

3. Adding and removing plaster to increase or decrease pressure according to the critical zones.

Image removed due to copyright restriction.

Figure 1: Manual Steps of the Socket Manufacturing Process; A – Bandaging Plaster on to the Stump; B – Reducing Positive Mold Circumference; C – Marking the Critical Zones; D – Manipulating the Critical Zones (Colombo et al. 2013)

Subsequently, a test socket is fabricated using a transparent material permitting the orthopedic technician a complete view of the socket. The test socket is also denoted by the names check socket and diagnostic socket as it allows the clinician to test, check or diagnose the socket through fitting it on patient's residual limb. After evaluating the optimal socket fit, a definitive socket is constructed using carbon and resin: fiberglass, carbon fiber or nylon (Engstrom & Van de Ven 1999).

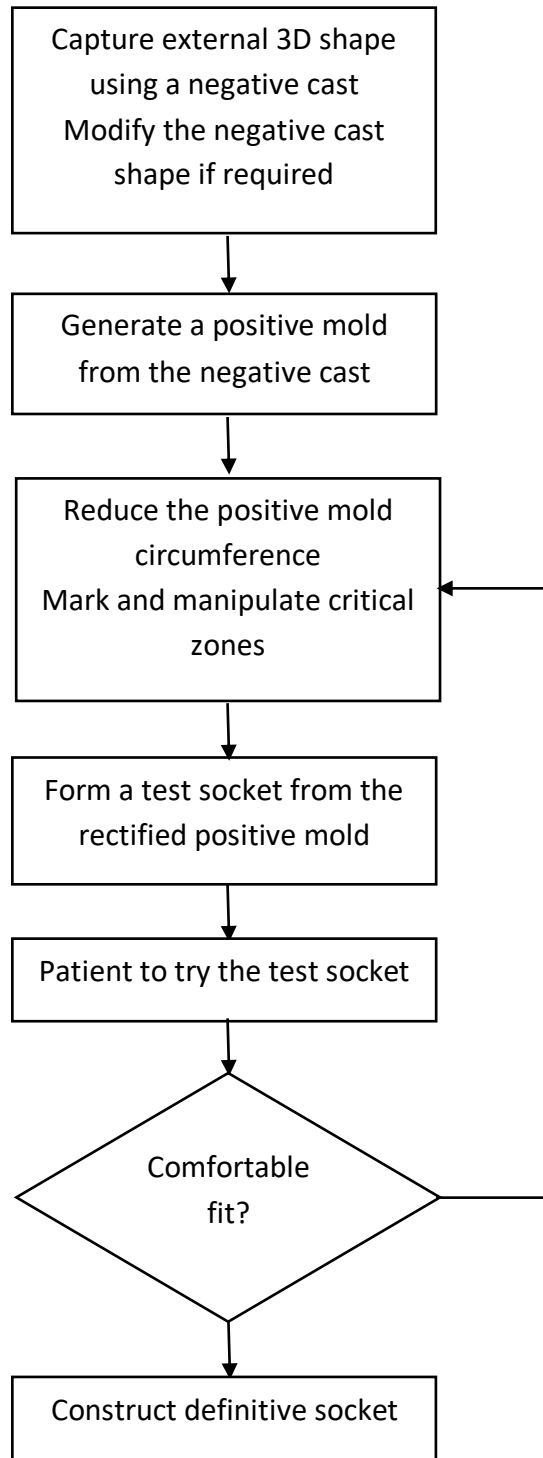


Figure 2: Socket Development Process

The socket development process ends with the construction of the definitive socket as shown in the flow chart (Figure 2). The other components of the lower limb prosthesis are assembled onto the socket to start the prosthesis alignment process. Alignments are done in three steps to ensure the appropriate functioning of the lower limb prosthesis with respect to the biomechanical structure of the body (Ikeda et al. 2012).

Table 2: Types of Alignments in Prosthesis Fabrication Process (Ikeda et al. 2012)

Alignment Type	Description	Parameters
Initial Bench	On the bench (without the user)	Socket design Prosthesis components Shoe style
Static Alignment	In sitting and standing position (with the user)	Prosthesis height Prosthesis inclination Prosthesis translation
Dynamic Alignment	While walking (with the user)	Prosthesis height Prosthesis inclination Prosthesis translation

The final step of the fabrication process is the construction of the cosmetic which may or may not be performed considering the patient's choice. The prosthesis cosmetic differs mainly due to the color or texture. The quality of the cosmetic depends on the financial status and the preference of the patient.

SOCKET

TYPES OF SOCKETS

The project considers the sockets used for the two most common lower limb amputations: transfemoral and transtibial amputations. The Figure 3 explains the existing socket types for patients with transfemoral and transtibial amputations.

As the name suggests, the Specific Surface Bearing (SSB) sockets apply or relief pressure at specific surface areas, while the Total Surface Bearing (TSB) sockets can distribute pressure evenly. Since SSB sockets reduced the loaded overall anatomical area, such regions had to endure high pressure values which caused a variety of superficial (ulcers and other skin problems) and deep tissue injuries. Due to the ability of TSB sockets to load the total residual stump area, the drawbacks of SSB sockets were eliminated through low local stresses, improving the patient comfort and socket fit (Highsmith, J.T. & Highsmith, M.J. 2007). Both transtibial and transfemoral sockets can be categorized either as a SSB or a TSB socket; most of the Ischial Containment Sockets (ICS) are TSB sockets, while most of the Sub – Ischial sockets are SSB sockets.

The most common and standard SSB socket for patients with transtibial amputation is the Patella Tendon Bearing (PTB) socket. As indicated by the name itself, the PTB socket loads at the patellar tendon which is located below the patellar. The PTB socket was later modified into two versions as, Patellar Tendon Bearing-SupraCondylar (PTB-SC) and Patellar Tendon Bearing-SupraCondylar SupraPatellar (PTB-SCSP). The PTB, PTB-SC and PTB-SCSP sockets are mainly differed by their suspension generation (Physiopedia Contributors, 2020):

- PTB – At the distal part of the thigh
- PTB-SC – At the medial and lateral areas of the femoral condyles
- PTB-SCSP – At the medial and lateral areas of the femoral condyles and at the suprapatellar area

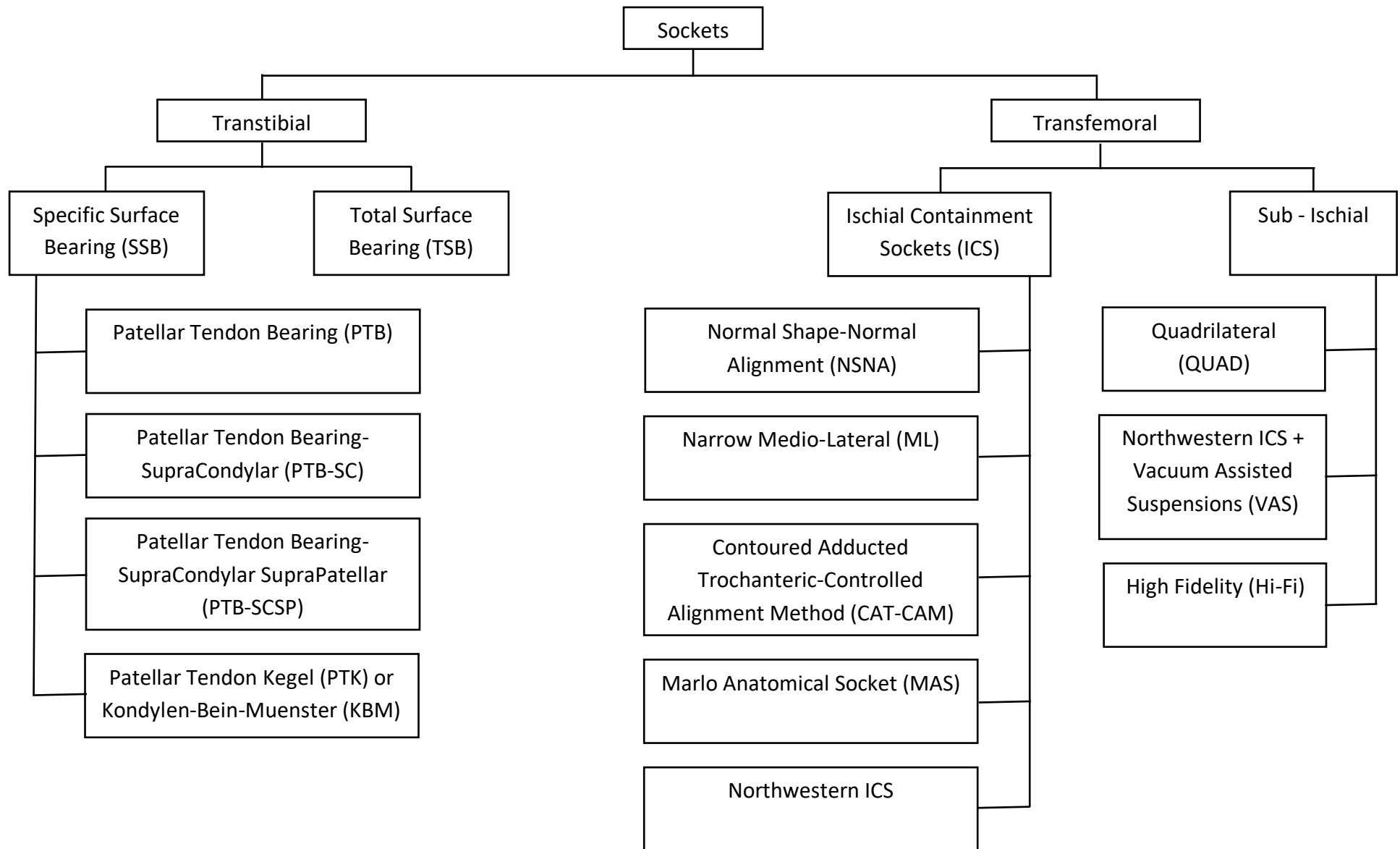


Figure 3: Transtibial and Transfemoral Socket Types (Paternò et al. 2018)

Image removed due to copyright restriction.

PTB

PTB - SC

PTB - SCSP

Figure 4: PTB Sockets (Physiopedia Contributors, 2020)

The sub-ischial quadrilateral (QUAD) socket concerns patients with transfemoral amputation and loads weight on to the ischial tuberosity through ischial support at the posterior shelf of the socket. Since QUAD is a SSB socket, it was recently replaced by ICS which loads weight to the whole stump surface without localizing the ischial tuberosity. ICSs can be developed in different configurations as Normal Shape-Normal Alignment (NSNA) socket (Long 1975), narrow Medio-Lateral (ML) socket (Rubin, Fischer & Dixon 1986), Contoured Adducted Trochanteric-Controlled Alignment Method (CAT-CAM) socket, Marlo Anatomical Socket (MAS) socket, and Northwestern ICS (Andrew 2008). Recent studies have proposed two solutions for sub-ischial sockets which could improve the comfort, stability and gait of the patient named as sub-ischial Northwestern socket (Fatone & Caldwell 2017) and High Fidelity (Hi-Fi) socket (Alley et al. 2011).

COMPLICATIONS DUE TO IMPERFECT SOCKET FIT

As a socket signifies the primary link between the natural (amputated residual limb) and artificial (prosthetic device) surfaces, a significant attentiveness should be made to the socket design in order to achieve a functional and comfortable lower limb prosthesis. The success or failure of the prosthesis depends on the several socket characteristics (Mak, Zhang & Boone 2001): socket fit, load transmission, stability, and control.

According to the current statistics, it has been reported that a significant number of patients with lower limb amputations do not use a prosthesis regardless of its advantages. This could be either due to lack of knowledge, ineligibility, insufficient prosthetic training, financial concerns, or low satisfaction level. The low satisfaction level of the lower limb prosthesis is mainly due to socket related issues including complications in skin tissues, poor biomechanical functionality, inadequate comfort, and obstructions in balance and control (Dillingham et al. 2001).

The socket design determines a range of parameters in the residual limb: temperature fluctuations, volume fluctuations, distribution of normal stress and strain, and distribution of shear stress and strain. Decreased volume of the residual limb could reduce the socket fit and change the distribution of normal and shear stresses and strains on the residual limb. This could generate friction between the socket and the residual limb causing increased temperature which would eventually produce sweat, irritation and, odor (Paternò et al. 2018).

With the variations in displacement between the residual limb and the socket governed by aforementioned parameters, intolerable pressure and deformation levels can be generated. This could contribute to the onset and propagation of a series of short-term and long-term complications. Recorded short-term complications include abrasions, blisters, callosities, and pressure ulcers in skin tissues, while long-term complications include scoliosis, osteoarthritis, and osteoporosis (Harker 2006).

RESEARCH PROBLEM

Biomechanical modelling has been used over the past two decades to model the residual limb soft tissue mechanics in order to eliminate the ill-fitting sockets. The efficacy and fidelity of biomechanical models require accurate information on the geometry and material properties of soft tissues. The main limitation of the previous work was the consideration of literature reported material properties; most of the researchers were leaned towards assuming linear, elastic, isotropic and homogenous material properties for the residual limb soft tissues.

RESEARCH AIM

To estimate patient-specific soft tissue deformations for the residual limb employing medical image data acquired while performing quasi-static loading experiments.

OVERVIEW OF THE RESEARCH METHODOLOGY

The project considered MRI scans related to three patients where each patient had to undergo a series of uniaxial quasi-static compression tests. The MRI scans were obtained using an MRI compatible sphygmomanometer which covered the patient's residual limb at 0 mmHg , 30 mmHg , 60 mmHg and 100 mmHg pressures, respectively. The MRI scans were segmented through Simpleware ScanIP to obtain surface and solid geometries of the uncompressed and the compressed states of the residual limb.

Rigid ICP algorithms were performed to register the uncompressed to each of the compressed surface geometries of the residual limb. Non-rigid ICP was then used to calculate soft tissue deformation at the entire residual limb surface for each of the compressed states. The area in contact with the sphygmomanometer was extracted to derive the force applied at each compressed state. Finally, the patient-specific soft tissue deformations of the residual limb were characterized by fitting piecewise linear models to force-deformation data acquired for each patient. All data processing were performed using MATLAB. Figure 5 illustrates the overall methodology for the research in this thesis.

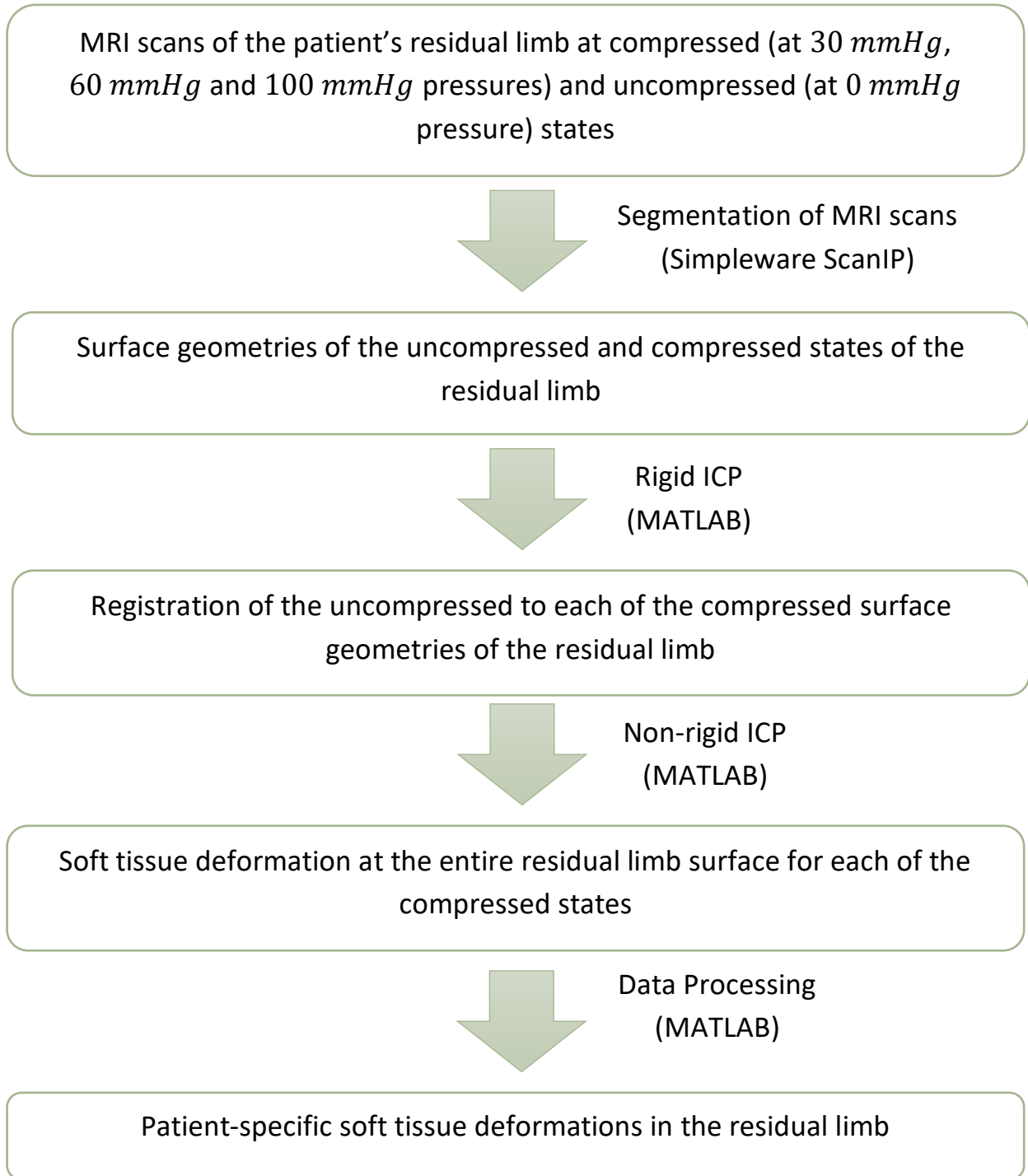


Figure 5: Process of Achieving Soft Tissue Deformations from MRI Scans

THESIS OUTLINE

In addition to the **introduction** chapter, the thesis submitted consists of five chapters. The second chapter presents a **review of previous literature** on different material properties for residual limb soft tissues in lower limb amputated patients. Chapter three aims to describe the **methodology** of the research and includes a detailed description about the process of achieving soft tissue deformations from MRI scans. Chapter four describes the **results** of the research which comprises the deformation fields and force-deflection plots achieved for each patient. Chapter five **discusses** the outcomes of the three patients and limitations related to the research. The **conclusion** chapter summarizes the potential usage of the attained soft tissue deformations towards residual limb soft tissue material properties and biomechanical modelling, and presents the anticipated future works.

LOWER LIMB BIOMECHANICS AND SOFT TISSUE DEFORMATION

When a patient with a lower limb prosthesis is standing or walking, the weight of the body is transferred to the socket through the residual limb, and the forces generated by the ground are transferred to the residual limb through the socket. As this takes place, soft tissues (primarily muscles, fat, and skin) undergo large deformations at locations where the bony prominences are bearing high loads or are covered with thin layers of soft tissues. Consequently, the main factors contributing to the initiation of soft tissue injury could be identified as the magnitude, the direction, and the duration of the applied load (Linder-Ganz et al. 2006; Gefen 2009).

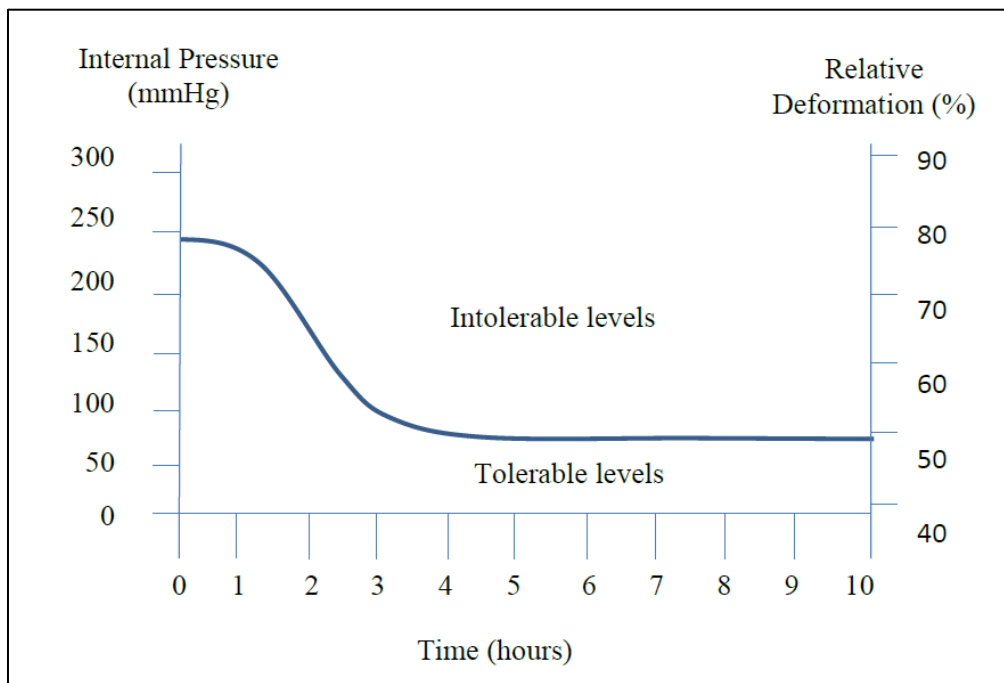


Figure 6: Internal Pressure and Relative Deformation vs Time (Gefen 2009)

Researchers have found that high pressures can directly damage cells, leading to an almost instantaneous soft tissue injury, while moderate pressures may result in equally severe injuries, if maintained over extended periods of time. The Figure 6 demonstrates the inverse relationship between the magnitude of the applied pressure and the period of time soft tissues can withstand a pressure before developing an injury (Linder-Ganz et al. 2006; Gefen 2009).

MATERIAL PROPERTIES OF SOFT TISSUES IN THE RESIDUAL LIMB

Soft tissues are capable of binding, supporting, and protecting human body structures and organs. Soft tissues include muscles, tendons, ligaments, blood vessels, nerves, skins, and articular cartilages among many others. The material properties of the soft tissues are highly influenced by the complex fiber reinforced composite structure composed of collagen, elastin, and extra cellular matrix. The Table 3 describes several material properties and associated constituents of some soft tissue types.

Table 3: Material properties and associated constituents of Several Soft Tissue Types (Fung 2013; Silver, Christiansen & Buntin 1989; Woo, Gomez & Akeson 1985)

Material	Ultimate Tensile Strength (MPa)	Ultimate Tensile Strain (%)	Collagen (% dry weight)	Elastin (% dry weight)
Tendon	50 - 100	10 - 15	75 - 80	0 - 3
Ligament	50 - 100	10 - 15	70 - 80	10 - 15
Aorta	0.3 - 0.8	50 - 100	25 - 35	40 - 50
Skin	1 - 20	30 - 70	60 - 80	5 - 10
Articular Cartilage	9 - 40	6 - 120	40 - 70	N/A

FINITE ELEMENT METHOD AND MATERIAL PROPERTIES OF SOFT TISSUES IN THE RESIDUAL LIMB

Finite Element Method (FEM) or Finite Element Analysis (FEA) is used more prominently in the engineering specialties including biomedical, aviation, civil, and structural (Magomedov, Khaliev & Elmurzaev 2020). FEM is widely used for modeling biomechanical systems mathematically due to the following advantages (Rzymkowski 2000):

- FEM can construct detailed models considering major (segment structure) to minor (cell structure) differences in human body.
- FEM can place detailed stress and strain distributions to any particular body segment.

Understanding on load distributions and magnitudes related to the soft tissues could be gained when FEM is applied to the residual limb of a patient with lower limb amputation. This knowledge could assist in socket optimization, allowing accelerated rehabilitation with increased patient satisfaction in financial, physical, and mental aspects.

Studies using FEM could be divided into three main stages as preprocessing, solution and postprocessing. The initial stage of preprocessing includes modelling the structure, applying the material properties, defining interactions between the structure segments, applying mesh (mesh type and mesh size), applying boundary, and loading conditions. The middle stage of solution generates an errorless complete analysis, while the final stage of postprocessing gathers the solutions and presents them in an understandable manner (Magomedov, Khaliev & Elmurzaev 2020).

According to the preprocessing stage of FEM, it is essential to apply structural material properties of soft tissue in the residual limb in order to optimize prosthetic sockets for patients with lower limb amputation using FEM.

ISOTROPIC AND LINEAR ELASTIC MATERIAL PROPERTIES

Isotropic materials are included with material properties that are independent of the direction of examination; material properties are identical in all directions. Following responses are considered when describing a material as linear elastic (Hall, Lindsay & Krayenhoff 2012; Kelly 2013):

- The stress is proportional to strain ($\sigma \propto \varepsilon$)
- The material will continue to deform with increasing load.
- The material returns to its original shape when the loads are removed, and the unloading path is the same as the loading path.

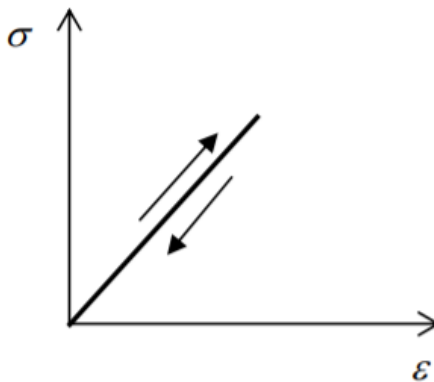


Figure 7: Stress-Strain Curve for Linear Elastic Material (Kelly 2013)

The stress-strain curve with loading and unloading pathways is shown in Figure 6. Linear elasticity could be defined for either an isotropic, orthotropic (material properties change in mutually perpendicular directions), or anisotropic (material properties change in all directions) material. Young's modulus (E) and Poisson's coefficient (ν) are used to characterize isotropic linear elastic materials.

$$E = \frac{\sigma}{\varepsilon}$$

Equation 1

$$\nu = -\frac{\varepsilon_{trans}}{\varepsilon_{axial}}$$

Equation 2

Where, E = Young's Modulus, σ = Stress, ε = Strain, ν = Poisson's Coefficient, ε_{trans} = Transverse Strain and ε_{axial} = Axial Strain.

Linear elasticity has been assumed for residual limb soft tissues in many studies during the early years (between 2000 to 2005), and on few studies after the year 2005 (Zhang and Roberts 2000; Zachariah and Sanders 2000; Wu et al. 2003; Lin et al. 2004; Lee et al. 2004; Jia et al. 2004; Jia et al. 2005; Ramírez and Vélez 2012; Velez Zea et al. 2015; Cagle et al. 2018). The studies have either considered above knee or below knee amputated patients, and several studies have considered the PTB and KBM sockets. Imaging modalities including plain radiography (X – ray), computed tomography (CT) and magnetic resonance imaging (MRI) has been used to generate the geometry. The Young's Modulus has deviated vastly from 100 *KPa* to 2490 *KPa* in the studies to assess the maximum normal and shear stresses corresponding to the different loading conditions. The ratio between the transverse and axial strain is denoted by the Poisson's ratio, and considers the material's compressibility. Due to the high-water content in soft tissue, they are often considered as incompressible ($\nu = 0.5$). The values between 0.45 and 0.49 have been used for Poisson's ratio in the mentioned studies as the limiting value of 0.5 is capable of producing numerical singularities in FEM analysis (Dickinson, Steer & Worsley 2017).

Table 4: Material Properties of Soft Tissues in the Residual Limb - Isotropic and Linear Elastic

Reference	Amputation	Geometry Source	Number of Samples	Loading	Material properties of Soft Tissues	Metric
Zhang and Roberts 2000	BKA	Biplanar	3	Static 800N axial load	$E = 160 - 260 \text{ KPa}$ $\nu = 0.49$	Maximum Normal Stress 90 kPa
	(PTB Socket)	X - ray				Maximum Shear Stress 50 kPa
Zachariah and Sanders 2000	BKA	CT	1	Static 800N axial load	$E = 965 \text{ KPa}$ $\nu = 0.45$	Maximum Normal Stress 201.5 kPa Maximum Shear Stress 33.2 kPa
Wu et al. 2003	BKA	CT	1	Static 235 N axial load - two leg stance	$E = 100 - 400 \text{ KPa}$ $\nu = 0.49$	Maximum Normal Stress KBM 250 kPa and TSB 240 kPa
	(KBM and PTB Sockets)			Static 470 N axial load - one leg stance		Maximum Shear Stress KBM 130 kPa and TSB 60 kPa
Lin et al. 2004	BKA	CT	1	Static 600 N axial load - one leg stance	$E = 60 - 2490 \text{ KPa}$ $\nu = 0.45$	Maximum Normal Stress 783 kPa Maximum Shear Stress 373 kPa
Lee et al. 2004	BKA	MRI	1	3 quasi - static force and moment points in gait cycle (heel strike, mid stance and toe-off)	$E = 200 \text{ KPa}$ $\nu = 0.49$	Maximum Normal Stress 185 kPa Maximum Shear Stress 67 kPa
Jia et al. 2004	BKA	MRI	1	3 quasi - dynamic force and moment points in	$E = 200 \text{ KPa}$	Maximum Normal Stress 340 kPa

	(PTB Socket)			gait cycle (heel strike, mid stance and toe-off)	$\nu = 0.49$	Maximum Shear Stress 85 <i>kPa</i>
Jia et al. 2005	BKA (PTB Socket)	MRI	1	3 quasi - dynamic force and moment points in gait cycle (heel strike, mid stance and toe-off) and knee flexion	$E = 200 \text{ KPa}$ $\nu = 0.49$	Maximum Normal Stress 323 <i>kPa</i>
Ramírez and Vélez 2012	AKA	CT	4	Socket preloading and quasi – static two leg stance (0.5 of the body weight)	$E = 200 \text{ kPa}$ $\nu = 0.475$	Principle Maximum Compressive Strain 31 – 74% Principle Maximum Tensile Strain 18 – 64% Maximum Von Mises Stress 120 – 860 <i>kPa</i>
Velez Zea et al. 2015	AKA	CT	5	Patient specific socket preloading, relaxation, and stance loading	$E = 200 \text{ KPa}$ $\nu = 0.475$	Maximum Normal Stress 81.7 – 151 <i>kPa</i> Maximum Shear Stress 14 – 55.5 <i>kPa</i>
Cagle et al. 2018	BKA	MRI	3	Axial force, vertical force, horizontal force, and sagittal moment representing heel strike, mid stance and toe-off	$E = 300 \text{ KPa}$ $\nu = 0.45$	Maximum Normal Stress 98 <i>kPa</i> Maximum Resultant Shear Stress 50 <i>kPa</i>

HYPERELASTIC MATERIAL PROPERTIES

As the linear elastic models are more suitable for small strain predictions, hyperelastic models have been evolved as a generalization of linear elastic models to accommodate non – linear and large strain predictions (Bergström 2015; Kelly 2013). Significant amount of effort has put into develop different hyperelastic theories throughout the years. The main benefits of hyperelastic models include the convenience in calibration, computational efficiency, accessible in commercial FE software (Bergström 2015).

The strain energy density function (W) is used in hyperelastic models to derive the relationship between the stress and strain. Even though the hyperelastic material strains are high (between 100% to 700%), the correlation between stress and strain can be accurately modeled using the SED function. Thus, several hyperelasticity models have been generated through the SED function which are accurate over different ranges of strain ((Bergström 2015; Dickinson, Steer & Worsley 2017; Omid et al. 2014).

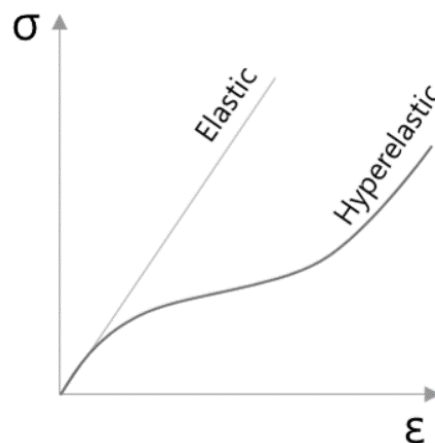


Figure 8: Stress-Strain Curve for Hyperelastic Material (Omid et al. 2014)

THE NEO-HOOKEAN MODEL

The simplest form of all commonly used hyperelastic models could be identified as the Neo-Hookean (NH) model (Bergström 2015). The NH model is based on two material parameters: shear modulus (G) and bulk modulus (K).

$$G = \frac{\tau}{\gamma}$$

Equation 3

$$K = -V \frac{\Delta P}{\Delta V}$$

Equation 4

Where, G = Shear Modulus, τ = Shear Stress, γ = Shear Strain, K = Bulk Modulus, V = Initial Volume, ΔV = Change in Volume and ΔP = Change in Pressure

The strain energy density function of the NH model can be expressed as:

$$W = \frac{G}{2} (I_1 - 3) + \frac{1}{D_1} (J - 1)^2$$

Equation 5

Where W = Strain Energy Density Function, G = Shear Modulus, I_1 = First Invariant of Principle Stretch Ratios, D_1 = Volumetric Constructive Model Parameter and J = Total Volume Ratio.

The NH model can be presented both for compressible and incompressible deformations. Since the incompressible version would have zero difference in volume ($\Delta V = 0$) for any pressure change, the case is considered as $K \rightarrow \infty$. D_1 is denoted as the incompressible parameter in the strain energy density function (W) of the NH model, since the second term becomes zero with the unity total volume ratio ($J = 1$).

THE MOONEY-RIVLIN MODEL

The Mooney-Rivlin (MR) model is an extension of the NH model. There are 4 types MR models based on the order of the formation: two parameter MR model, three parameter model, five parameter model, and nine parameter model (Bergström 2015).

The relationship between shear modulus and deformation constructive model parameters in the two parameter MR model could be represented as:

$$G = 2(C_{10} + C_{01})$$

Equation 6

Where G = Shear Modulus and C_{ij} = Deformation Constructive Model Parameter.

Hyperelasticity has been assumed for residual limb soft tissues in many studies after the year 2007 (Portnoy et al. 2008; Portnoy et al. 2009; Portnoy et al. 2011; Lacroix & Patiño 2011; Zhang et al. 2013). The studies have either considered above knee or below knee amputated patients and have used imaging modalities of CT and MRI to generate the geometry. Most of the studies have used three parameter MR model (Portnoy et al. 2009; Portnoy et al. 2011), while a few studies have used two parameter MR model (Portnoy et al. 2008; Zhang et al. 2013).

Table 5: Material Properties of Soft Tissues in the Residual Limb - Hyperelastic

Reference	Amputation	Geometry Source	Number of Samples	Loading	Material properties of Soft Tissues	Metric
Portnoy et al. 2008	BKA	MRI	1	Static 0.9 mm axial displacement	NH Model (Muscle): $G = 8.5 \text{ kPa}$ $D_1 = 0 \text{ MPa}^{-1}$ Two Parameter MR Model (Skin): $C_{10} = 85.5 \text{ kPa}$ $C_{01} = 21.4 \text{ kPa}$ $\nu \approx 0.5$	Maximum Strain Energy Density 104 kJm^{-3} Maximum Principle Tensile Strain 129% Maximum Principle Compressive Strain 85% Maximum Shear Strain 106% Maximum Principle Tensile Stress 263 kPa Maximum Principle Compressive Stress 240 kPa Maximum Shear Stress 23 kPa Maximum Von Mises Stress 215 kPa
Portnoy et al. 2009	BKA	MRI	1	Static 0.9 mm axial displacement	Three Parameter MR Model (Muscle): $C_{10} = 2.3 - 8.1 \text{ kPa}$ $C_{11} = 0 \text{ kPa}$	Maximum Strain Energy Density 104 kJm^{-3} Maximum Principle Tensile Strain 129% Maximum Principle Compressive Strain 85% Maximum Shear Strain 106%

					$D_1 = 4.4 - 1.2 MPa^{-1}$ Three Parameter MR Model (Fat): $C_{10} = 0.143 kPa$ $C_{11} = 0 kPa$ $D_1 = 70.2 MPa^{-1}$ Three Parameter MR Model (Skin): $C_{10} = 9.4 kPa$ $C_{11} = 82 kPa$ $D_1 = 0 MPa^{-1}$	Maximum Principle Tensile Stress $263 kPa$ Maximum Principle Compressive Stress $240 kPa$ Maximum Shear Stress $23 kPa$ Maximum Von Mises Stress $215 kPa$
Portnoy et al. 2011	BKA	MRI	1	30° and 90° knee flexion angles - sitting	Three Parameter MR Model (Muscle): $C_{10} = 4.25 kPa$	Maximum Principle Compressive Stress $102 kPa$ Maximum Principle Tensile Stress $66.6 kPa$

					$C_{11} = 0 \text{ kPa}$ $D_1 = 24.34 \text{ MPa}^{-1}$ Three Parameter MR Model (Fat): $C_{10} = 2.97 \text{ kPa}$ $C_{11} = 0 \text{ kPa}$ $D_1 = 34.8 \text{ MPa}^{-1}$ Three Parameter MR Model (Skin): $C_{10} = 9.4 \text{ kPa}$ $C_{11} = 82 \text{ kPa}$ $D_1 = 0 \text{ MPa}^{-1}$	Maximum Von Mises Stress 129 kPa Maximum Shear Stress 67.2 kPa Maximum Injury Rate $-8.67 \text{ mm}^3 \text{ min}^{-1}$
Lacroix & Patiño 2011	AKA	CT	5	Axial load onto the socket within 15 s with	Three Parameter MR Model: $C_{10} = 4.25 \text{ kPa}$	Maximum Normal Stress 4 kPa Average Maximum Longitudinal Shear Stress 1.4 kPa

				velocity from 6 to 9 $mm s^{-1}$ – socket donning	$C_{11} = 0 \text{ kPa}$ $D_1 = 2.36 \text{ MPa}^{-1}$	<p>Average Maximum Circumferential Shear Stress 0.6 kPa</p> <p>Maximum Principle Tensile Strain 18 – 64%</p> <p>Maximum Principle Compressive Strain 31 – 74%</p> <p>Maximum Von Mises Stress 5 – 24 kPa</p>
Zhang et al. 2013	AKA	CT	1	50 N axial socket preloading and 3 quasi-static force and moment points in gait cycle (heel strike, mid stance and toe-off)	<p>Two Parameter MR Model:</p> $C_{10} = 85.5 \text{ kPa}$ $C_{01} = 21.4 \text{ kPa}$ $\nu = 0.459$	<p>Maximum Normal Stress 119 kPa</p> <p>Maximum Longitudinal Shear Stress 25.7 kPa</p> <p>Maximum Circumferential Shear Stress 104 kPa</p>

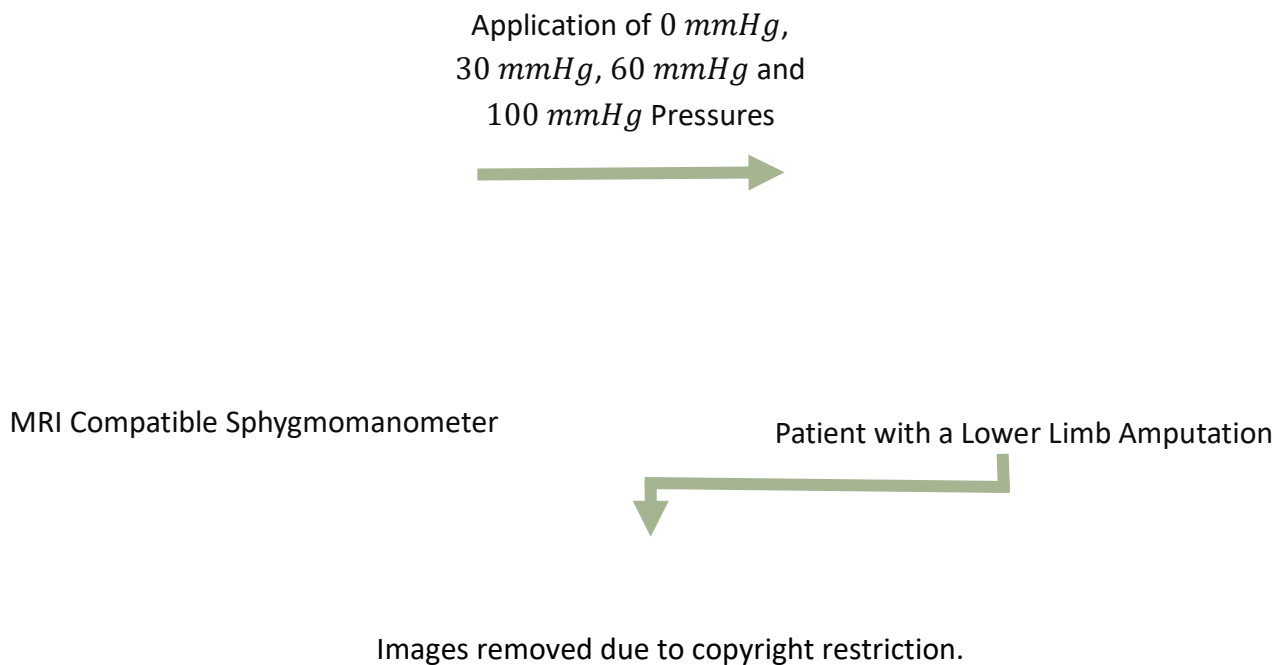
METHOD

COMPRESSION TEST AND MAGNETIC RESONANCE IMAGING

The project considered the MRI scans related to three patients where each patient had to undergo a series of uniaxial quasi-static compression tests.

COMPRESSION TEST

The data required to characterize soft tissue deformations of the patient's residual limb were obtained through a series of four uniaxial quasi-static, uniaxial compression tests. In each test, a known pressure was applied to the patient's residual limb, which caused its deformation.



MRI of the Residual Limb at 0 *mmHg* MRI of the Residual Limb at 30 *mmHg* MRI of the Residual Limb at 60 *mmHg* MRI of the Residual Limb at 100 *mmHg*

Figure 9: Schematic Diagram of Obtaining Medical Images (Cone Instruments 2021; Foisneau-Lottin et al. 2003)

The pressure was applied through an MRI compatible sphygmomanometer (Cone Instruments, USA) which covered most of the residual limb. The applied pressures were at 0 *mmHg*, 30 *mmHg* and 100 *mmHg* respectively.

MAGNETIC RESONANCE IMAGING

Imaging modality controls what part of the body is being excited during the imaging process. Imaging modalities of plain radiography (Zhang and Roberts 2000), CT (Zachariah and Sanders 2000; Wu et al. 2003; Lin et al. 2004; Lacroix & Patiño 2011; Ramírez and Vélez 2012; Zhang et al. 2013; Velez Zea et al. 2015) and MRI (Lee et al. 2004; Jia et al. 2004; Jia et al. 2005; Portnoy et al. 2008; Portnoy et al. 2009; Portnoy et al. 2011; Cagle et al. 2018) have been used to generate the residual limb geometries of lower limb amputated patients.

MRI scans of the residual limb were taken at each of the mentioned quasi-static pressures using a Siemens 3T MRI Scanner. Each of the MRI scans were included with 40 transverse slices, 448 sagittal slices and 448 frontal slices. The study was approved by the Southern Adelaide Clinical Human Research Ethics Committee (HREC/18/SAC/225). The Figure 9 describes the process of obtaining medical images through a schematic diagram.

GENERATION OF SURFACE AND SOLID GEOMETRIES

The strong magnetic field of MRI is capable of exciting the water molecules or the hydrogen atoms within the body, which would release different waveforms based on the excitation level. The released energy through waveforms is detected and reflected on the MRI scans through grey levels. The anatomical structures with more water or air content (cancellous bone) would look brighter, while the anatomical structures with less water or air content (cortical bone) would appear darker in the MR images (Berger 2002). The knowledge regarding the grey levels of cancellous and cortical bones were used to distinguish bone (hard tissues), as the generation of surface and solid geometries required to identify between the hard and soft tissues.

The most significant step when converting an MRI image to either a surface or FE model is image segmentation: the separation of images into regions of interest that correspond to a specific anatomical structure. Image segmentation could be based on measurements taken from the image including grey level, colour, texture, depth, or motion. Since an MRI is visualized in grey levels, it can be segmented manually using the knowledge of correspondence between the anatomical structures and grey levels.

The MRI scans which were taken at each of the mentioned quasi-static pressures were segmented manually through Simpleware ScanIP (Synopsys, California, USA) to obtain surface and solid geometries of the uncompressed and the compressed states of the residual limb for the project.

To date, the most commonly used image segmentation techniques for medical images include characteristic feature thresholding or clustering, edge detection and region extraction (Zanaty and Ghoniemy 2016). Simpleware ScanIP was also comprised with automated and semi-automated tools (threshold, region grow, flood fill, etc.) to obtain the regions of interest in a fast and accurate manner. However, most of these automated or semi-automated tools were not able to be used while segmenting MRI scans, as a specific grey level did not distinguish between

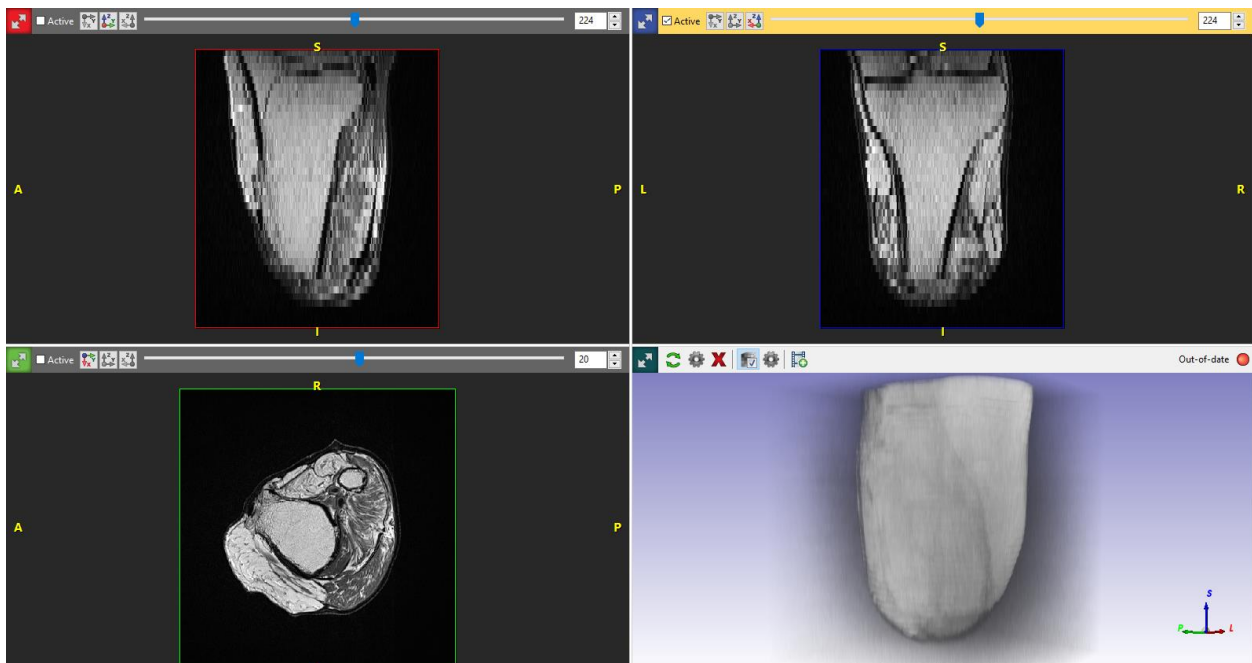


Figure 10: MRI visualization on Simpleware ScanIP

the bones and the soft tissues. Therefore, the MRI scans related to this study required manual segmentation.

Four separate MRI scans were available for the patient. Each MRI scan included 40 DIACOM (Digital Imaging and Communications in Medicine) images, as they were imaged in an axial direction with thin slices. Edges of the anatomical structures were able to be identified as Simpleware ScanIP allows greyscale-based slice to slice propagation and visualize the image in all three directions (Figure 10). Manual segmentation of each data set through Simpleware ScanIP was a labor-intensive process and required a substantial amount of time.

Different masks were created to define the boundaries for flesh and bones. For the MRIs that visualized the femur, four masks were created indicating tibia, fibula, femur, and flesh, while other MRI scans were only segmented for three masks (tibia, fibula, and flesh). Figure 11 demonstrates an MRI with three masks: tibia in pink, fibula in orange and flesh in blue.

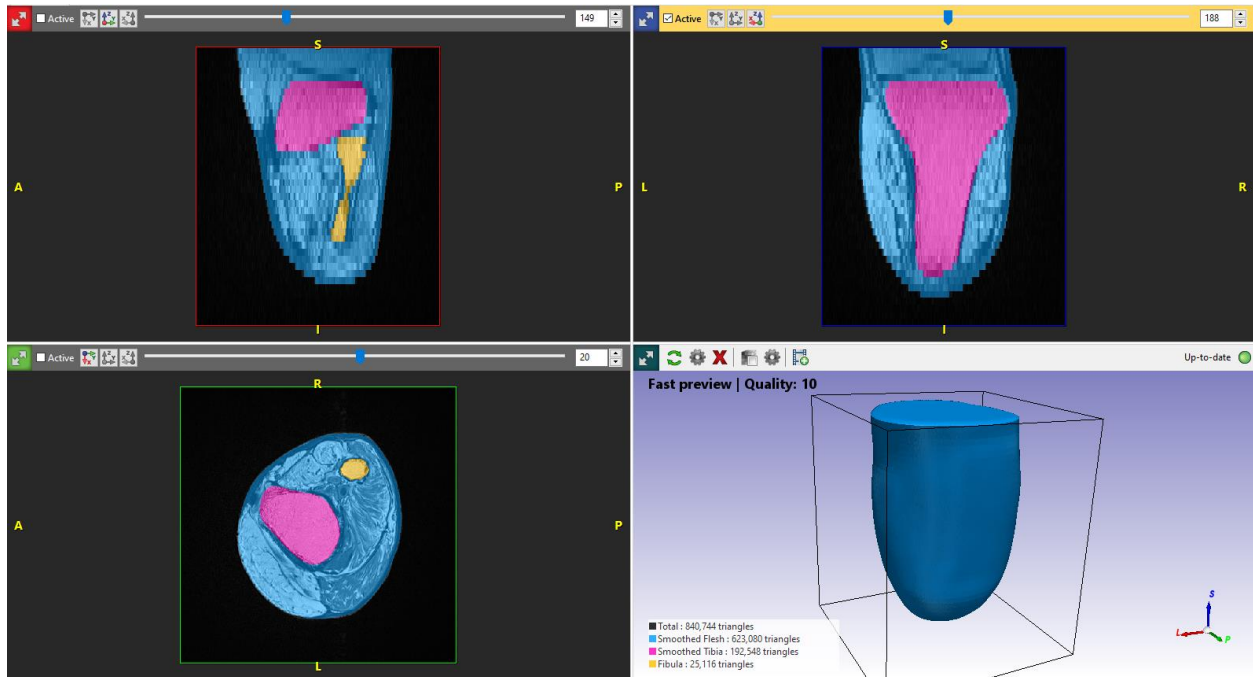


Figure 11: Defined Masks on Simpleware ScanIP

The Simpleware ScanIP tools of threshold (paint with threshold and threshold) were not used as they generated inconsistent segmentation results. Initially the paint tool was used to define the

edge of the considered anatomical structure (Figure 12), and then the flood fill tool was used to fill the shape in (Figure 13).

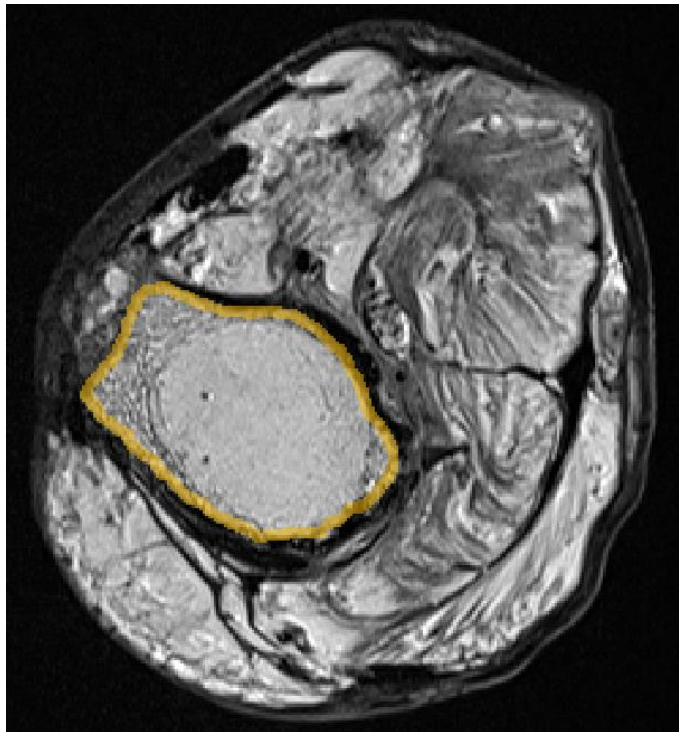


Figure 12: Defining the Bone using the Paint Tool

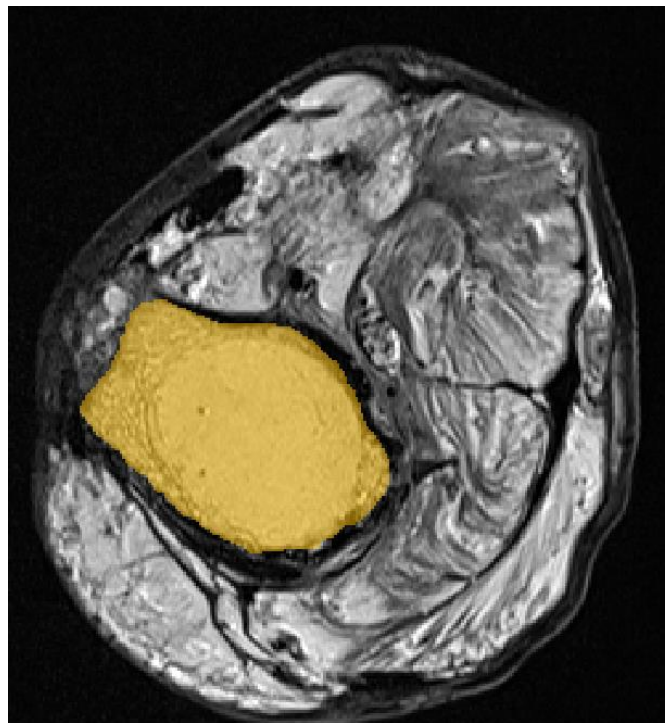


Figure 13: Filling the Bone using the Flood Fill Tool

3D wrap filter was used after segmenting the images slice wise, dropping nearly half of the in between slices (Figure 14). The 3D wrap filter is capable of creating a mask from cross sections rather than having to paint each slice of the image data.

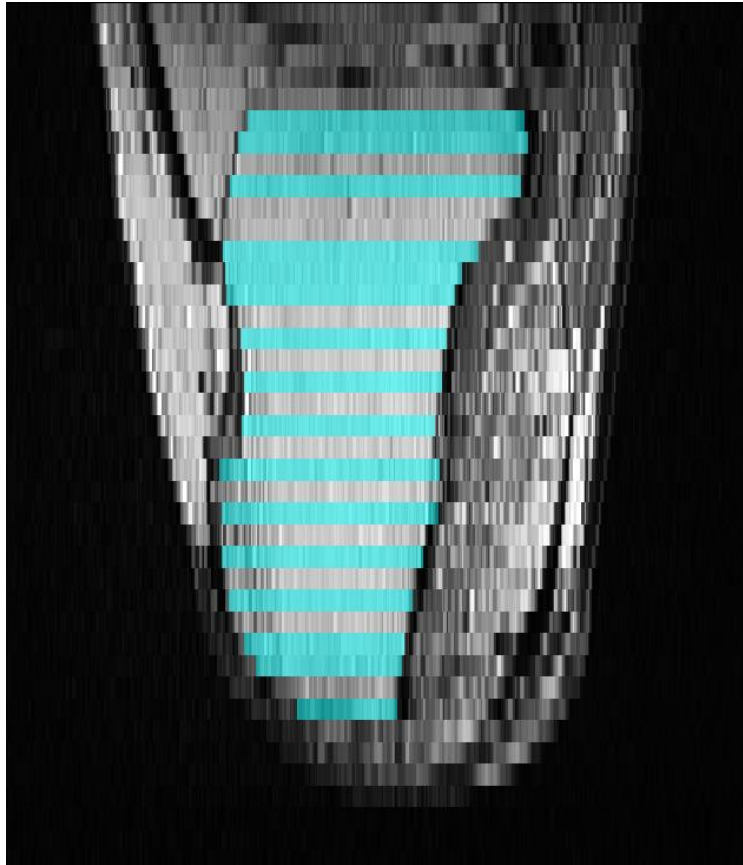


Figure 14: Segmentation before using the 3D Wrap Filter

Each of the anatomical structures were smoothed using recursive gaussian filter after using the 3D wrap tool. After segmenting the required anatomical structures, Boolean operations were performed to subtract the bone masks from the flesh mask. Figure 15 demonstrates the 3D geometries resulting from image segmentation of both flesh and bone; the bones are not visible as they are obscured by flesh. Figure 16 shows bone geometries resulted from image segmentation: tibia in red, fibula in green and femur in brown. Figure 17 image shows the flesh layer after performing the Boolean operation.

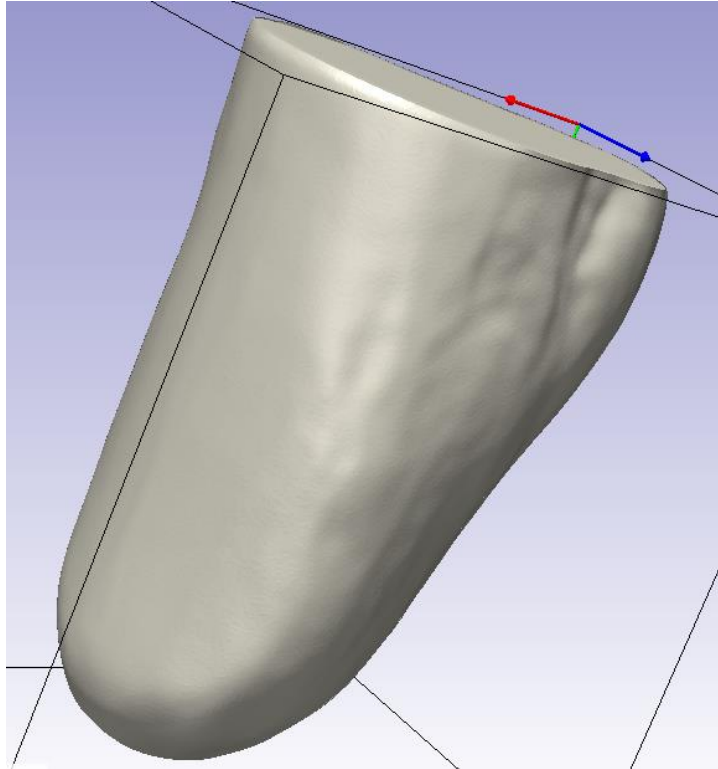


Figure 15: Flesh and Bone Geometries Resulted from Segmentation

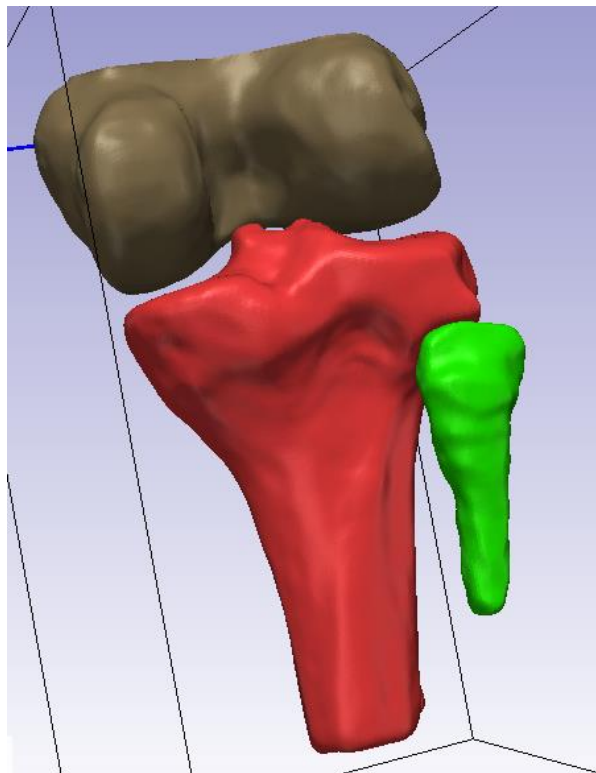


Figure 16: Bone Geometries Resulted from Segmentation

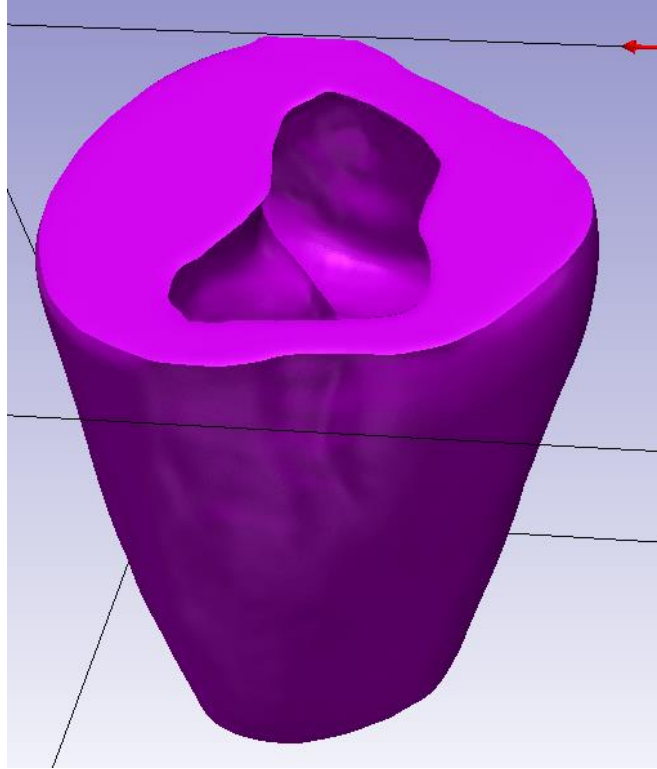


Figure 17: Flesh Layer After Performing Boolean Operation

The segmentation processes related to the considered residual limbs of the three lower limb amputated patients were distinct from one another. One of the patients had a very bright region on his MRI scan, which was later identified as a section of heel pad. Based on patient's testimony, it was realized that the surgeons have cut the heel pad and inserted on to the stump of the patient, as the patient had required more flesh on the stump to be acceptable for prosthesis.

Finally surface and solid geometries were created which were later saved as STL and INP files respectively to be used on MATLAB.

ITERATIVE CLOSEST POINT ALGORITHM

The iterative closest point (ICP) algorithm is capable of generating the transformation between the source and target point clouds through nearest neighbor approach between the corresponding entities. The target point cloud is always kept fixed, while the source point cloud is transformed to align with the target point cloud.

The ICP algorithm consists of two key steps: data association and transformation. At first, the points from the source point cloud would consider the closest points from the target point cloud. Then, the initial transformation would be computed based on this initial data association configuration. The transformation to minimize the distance between the corresponding points is done in two stages (Rusinkiewicz & Levoy 2001):

1. Translation - Computation of center of masses of corresponding points.
2. Rotation - Computation of the optimal rotation between the corresponding points.

The process would be repeated through recomputing the data association and recomputing the transformation until convergence between the source and target point clouds.

The project utilized the ICP algorithm in two approaches: rigid and non-rigid registrations. The rigid ICP registration denotes the basic version of ICP, while the non-rigid ICP registration is a procedure where a search based on spatial proximity generates the correspondence of points, and the transformation of each point is modelled by general deformation (Cheng et al. 2017).

RIGID ICP REGISTRATION

In the project rigid ICP algorithm was performed to register the uncompressed (geometry at *0mmHg* pressure – Model_0mmHg) to each of the compressed surface geometries (geometries at *30mmHg*, *60mmHg* and *100mmHg* pressures – Model_30mmHg, Model_60mmHg and Model_100mmHg) of the residual limb. The rigid ICP was performed only on the bone of the

residual limb – tibia. Since tibia does not change its shape when a pressure is applied, tibia's change in space was able to be measured through rigid ICP registration.

The process of rigid ICP registration, non-rigid ICP registration and deformation field calculation has only considered the compressed surface geometry at 30 *mmHg* (Model_30mmHg) to describe the methods related to MATLAB. The compressed surface geometries at 60 *mmHg* and 100 *mmHg* (Model_60mmHg and Model_100mmHg) were also processed in a similar way to obtain the required results.

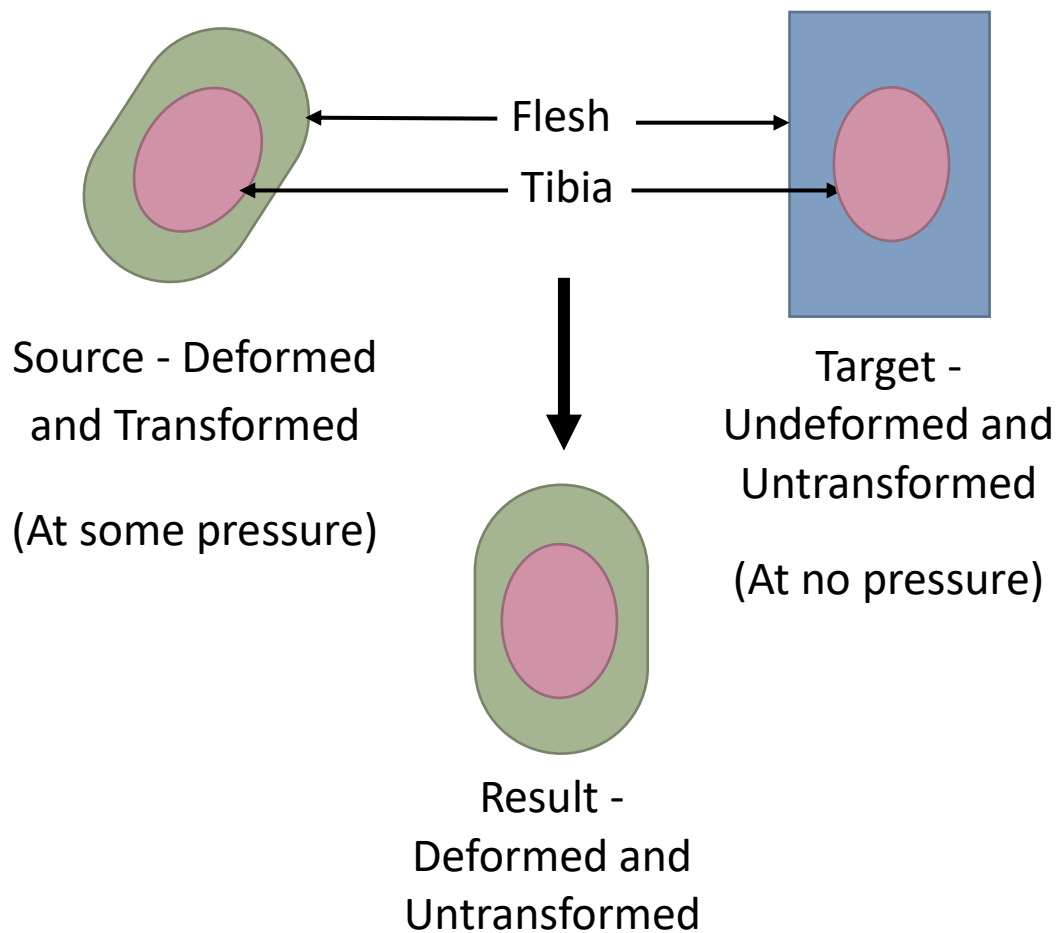


Figure 18: Schematic Diagram of Rigid ICP Registration on Tibia

According to Figure 18, the source was considered as the surface geometry at some pressure (Model_30mmHg), and the target was considered as the surface geometry at no pressure (Model_0mmHg). Thus, the source was deformed as well as transformed due to the applied pressure, while the target was undeformed and untransformed with zero pressure. The shape change in flesh is denoted by the word “Deformed”, and the change in space (translation and rotation) relative to the geometry at no pressure is denoted by the word “Transformed”. The transformation matrix obtained through rigid ICP algorithm is applied to the deformed and transformed state to make it deformed but untransformed.

The following function was used in MATLAB to perform rigid ICP registration on tibia. The function is capable of rotating, translating, and scaling a source three-dimensional point cloud, to fit a target three-dimensional point cloud with similar shapes (Manu 2021a).

$$[error, Reallignedsource, transform] = rigidICP(target, source)$$

The inputs of the function are the target vertices of $N \times 3$ size (N points in N rows and 3 columns for X , Y and Z coordinates), and the source vertices of $M \times 3$ size (M points in M rows and 3 columns for X , Y and Z coordinates). The outputs of the function includes the minimized value of dissimilarity measure (error), the points of the transformed source, and the transformation. The transformation is comprised with three variables accounting for the rotation (T), scaling (b), and translation (c).

$$Reallignedsource = (b \times source \times T) + c$$

The code on Appendix 1 was used to perform rigid ICP registration on tibia when the target tibia is at 0 mmHg, and the source tibia is at 30 mmHg.

Figure 19 demonstrates the tibia before the rigid ICP registration: source tibia (tibia related to Model_30mmHg) and Figure 20 demonstrates the tibia after the rigid ICP registration: realigned tibia. Figure 21 demonstrates the target tibia, source tibia (tibia related to Model_0mmHg) and the realigned tibia on the same plot. The realigned tibia has been obtained through using the transformation matrix between the target and source tibia, on the source tibia itself.

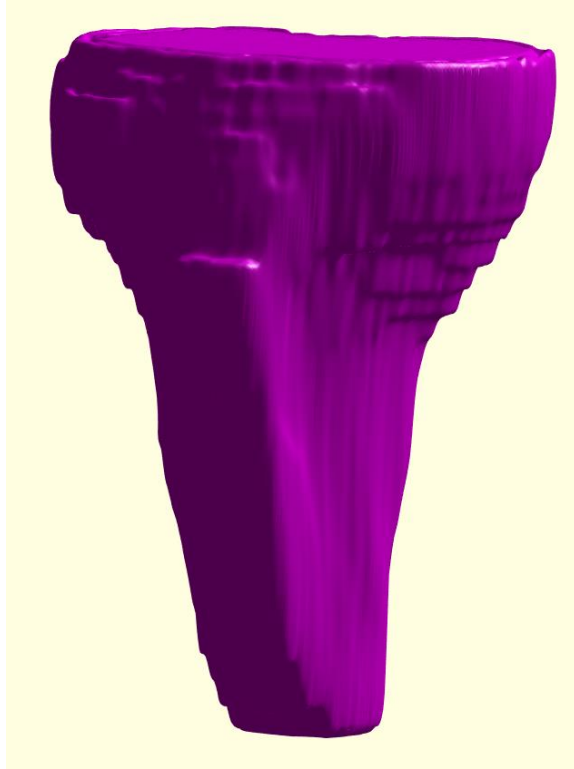


Figure 19: Tibia before Rigid ICP Registration - Source Tibia

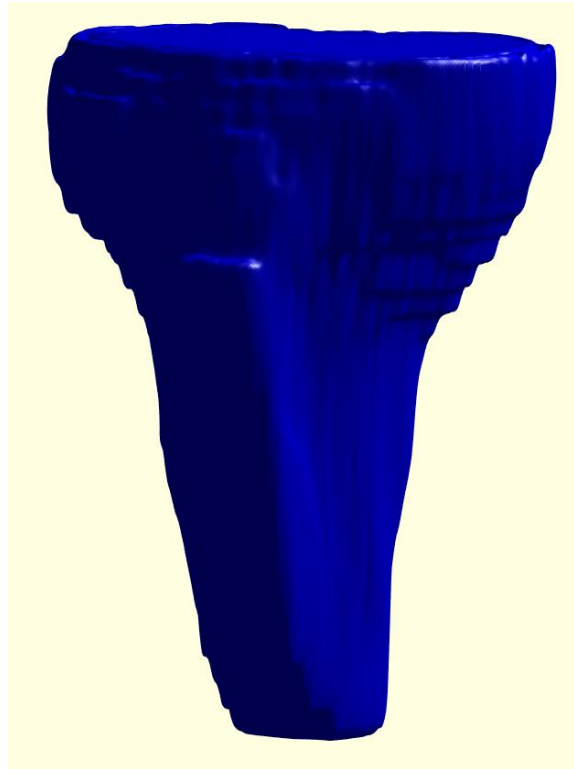


Figure 20: Tibia after Rigid ICP Registration - Realigned Tibia



Figure 21: Rigid ICP Registration on Tibia

To complete the registration of the entire residual limb models, the transformation matrix gained through the rigid ICP registration was reconstructed and applied to the source flesh at 30 *mmHg* using the code on Appendix 2.

Figure 22 demonstrates the flesh before the rigid ICP registration: source flesh (flesh related to Model_30mmHg) and Figure 23 demonstrates the flesh after the rigid ICP registration: realigned flesh through the transformation matrix. Figure 24 shows the source flesh and the realigned flesh on the same plot.

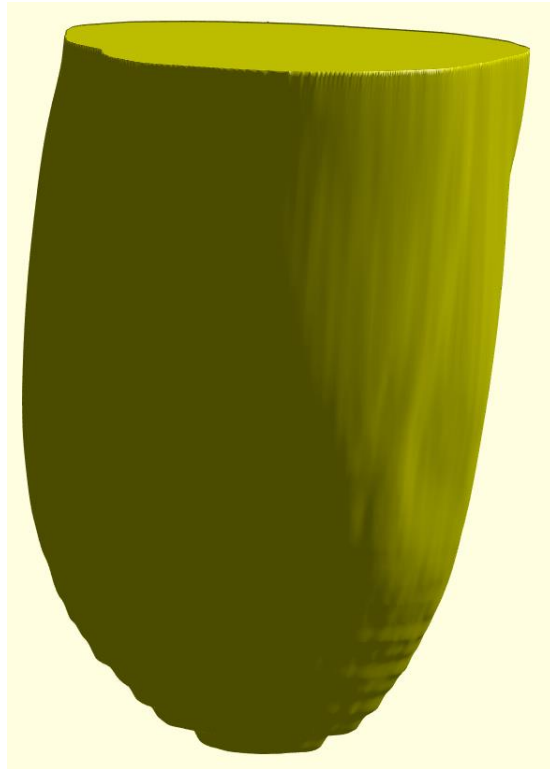


Figure 22: Flesh before Rigid ICP Registration - Source Flesh

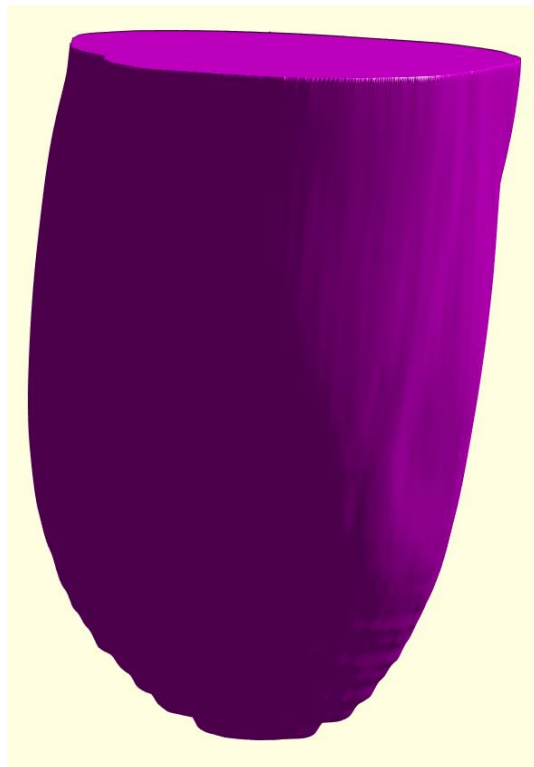


Figure 23: Flesh after Rigid ICP Registration - Realigned Flesh

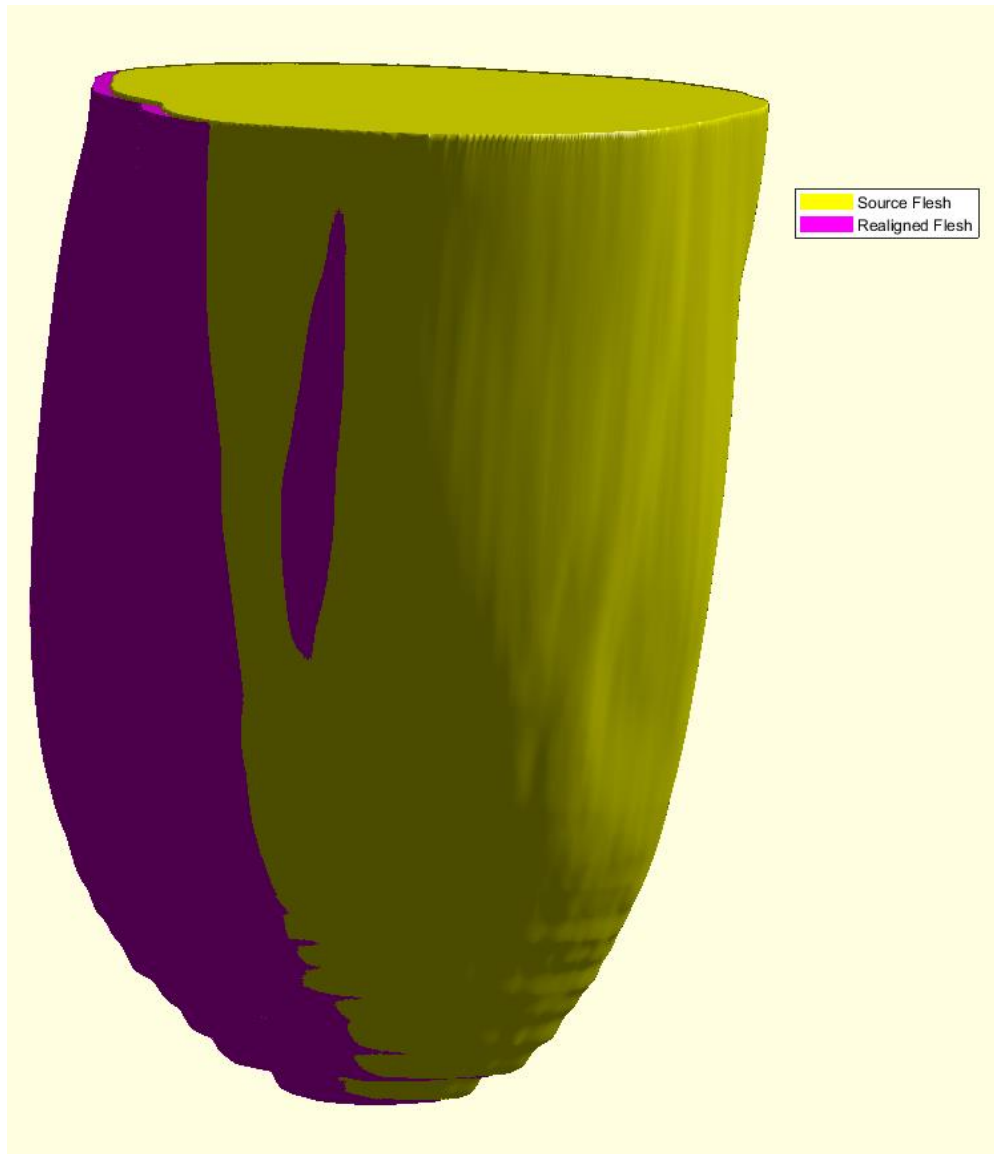


Figure 24: Realignment of Flesh through Rigid ICP Registration

NON-RIGID ICP REGISTRATION

After performing rigid ICP registration on tibia and applying the transformation matrix to the flesh of the compressed model (Model_30mmHg), non-rigid ICP registration was applied on flesh to calculate soft tissue deformation at the entire residual limb surface for each of the compressed states. The source of the non-rigid ICP registration was the target of the rigid ICP registration – the residual limb at no pressure which was undeformed and untransformed (Model_0mmHg).

The target was the result obtained from the rigid ICP registration, which was in the deformed but untransformed state. Since both source and target were neither translated nor rotated, non-rigid ICP registration was performed on flesh to calculate the deformation field (Figure 25).

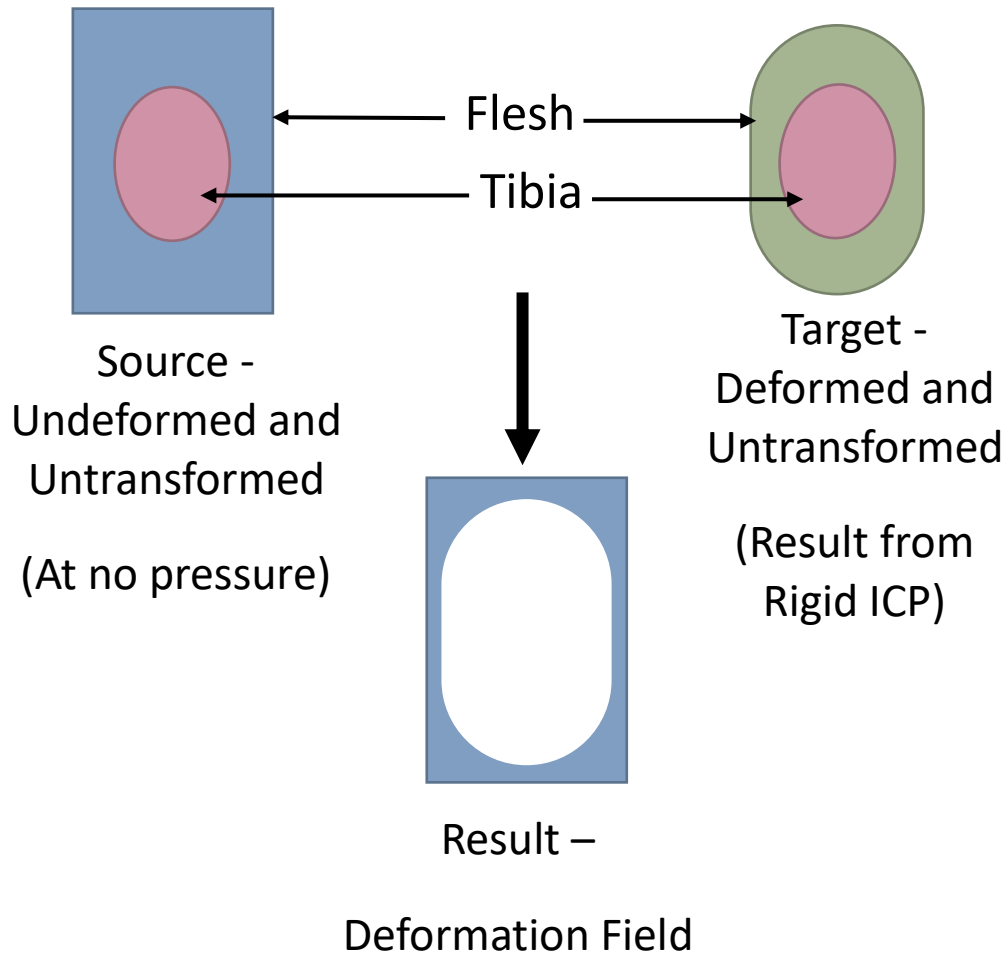


Figure 25: Schematic of Non-rigid ICP Registration on Flesh

The following function was used in MATLAB to perform non-rigid ICP registration on flesh. The function is capable of aligning and non-rigidly deforming a source mesh to a target mesh ((Manu 2021b)).

```
[registered]
= nonrigidICP(targetV, sourceV, targetF, sourceF, iterations, flag_prealigndata)
```

The inputs of the function are the target nodes of $N \times 3$ size (N points in N rows and 3 columns for X , Y and Z coordinates), source vertices of $M \times 3$ size (M points in M rows and 3 columns for X , Y and Z coordinates), target elements, source elements, iterations, and flag for pre-aligned data. The function prefers iterations to be within 10 and 30, while the flag for pre-aligned data can be set as 1 if the data is already aligned, and 0 if the data is not aligned. The output of the function is the registered source vertices on the target mesh; faces of the source mesh are not affected by the non-rigid ICP registration.



Figure 26: Non-rigid ICP Registration on Flesh

The code on Appendix 3 was used to perform non-rigid ICP registration on flesh when the target flesh is the aligned flesh at 30 *mmHg*, and the source flesh is at 0 *mmHg* (Model_0mmHg). The number of iterations was set at 10, while the flag for pre-aligned data was set as 1, as the data was already aligned. Figure 26 demonstrate the source flesh and target flesh from the top and side views after 10 iterations of non-rigid ICP registration.

DEFORMATION FIELD

The distance between the undeformed and untransformed flesh at 0 *mmHg* (Model_0mmHg) and deformed and untransformed flesh at 30 *mmHg* was initially calculated. In order to calculate the distance between two shapes, the number of nodes in both shapes required to be exactly the same, corresponding to the same anatomical landmark (Figure 27). The output of the non-rigid ICP generated registered source nodes on target mesh, which was denoted as *registered*. Thus, the vertices of the deformed and untransformed flesh at 30 *mmHg* was considered as *registered*, while the vertices of the undeformed and untransformed flesh at 0 mmHg was denoted by *targetFleshV*.



Figure 27: Registered and targetFleshV Variables with Similar Matrix Sizes

The code on Appendix 4 was used to obtain the distance between the two shapes. After using the distance formula, a for loop was used to filter the compressions and tensions of the deformation field. Even though a series of uniaxial compression tests were applied on the residual limbs, the rigid and non-rigid ICP registrations could place the deformed and untransformed flesh at 30 mmHg with minor inaccuracies. These node placements could measure the distance between the two shapes as negative, presuming tensions. Thus, the code filtered the tensions, and revalued the corresponding distances accordingly.

The *boundary* function on MATLAB is capable of returning a triangulation representing a single conforming three-dimensional boundary around a point cloud. In order to create a triangulation around the vertices in *registered*, the *boundary* function was used with a shrink factor of 0.95. In order to calculate the midpoint in each triangle within the triangulation, a for loop was created and the calculated midpoints were incorporated on to the variable *xq*. The *griddatan* function was used to fit a hypersurface to the points on *registered* with the values calculated on *dsqrt*,

and to interpolate the surface at the xq points to return the interpolated values of vq (Appendix 5). Figure 28 represents the xq points with the vq value on them. It could be seen that the vq values differ approximately from 0 to 3 according to the level of deformation.

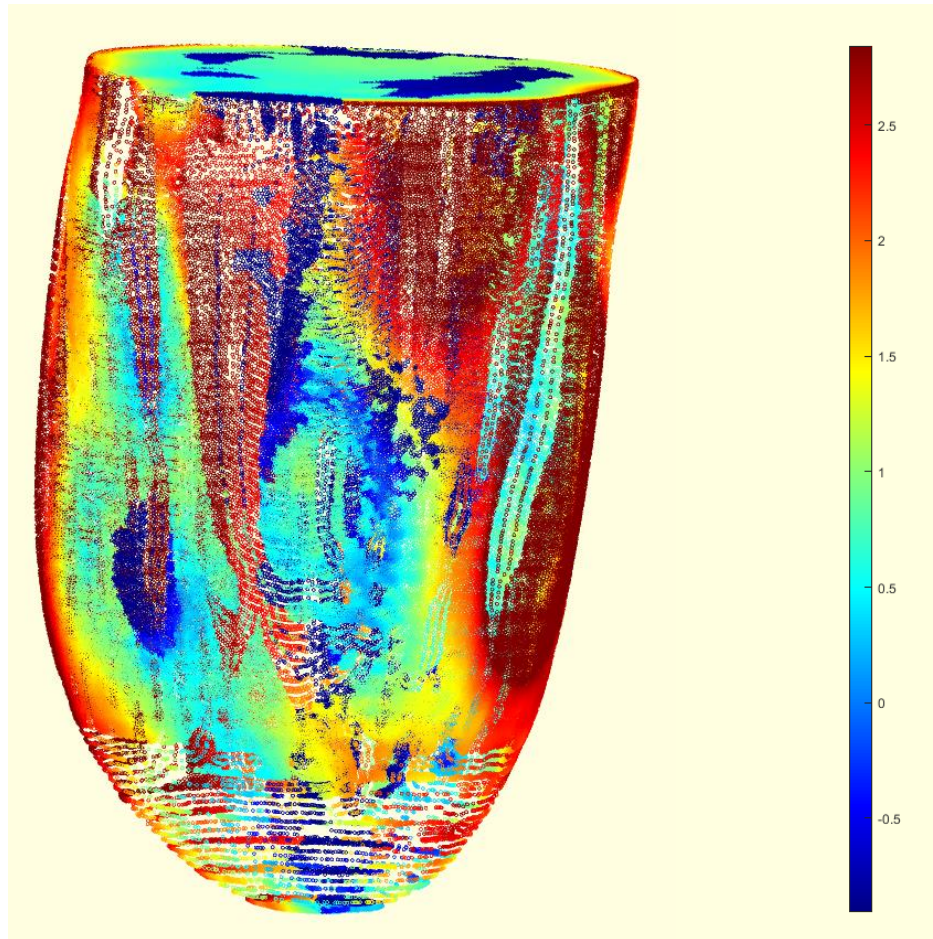


Figure 28: Triangle Midpoints (xq) with Interpolated Values (vq)

In order to visualize the most compressed areas of the residual limb, a for loop was created to extract the interpolated deformations greater than 3 (Appendix 6). Figure 29 demonstrates the xq points with the filtered vq values (vq_n) on them. The xq points with vq values lesser than 3 are represented as zero deformation ($vq = 0$).

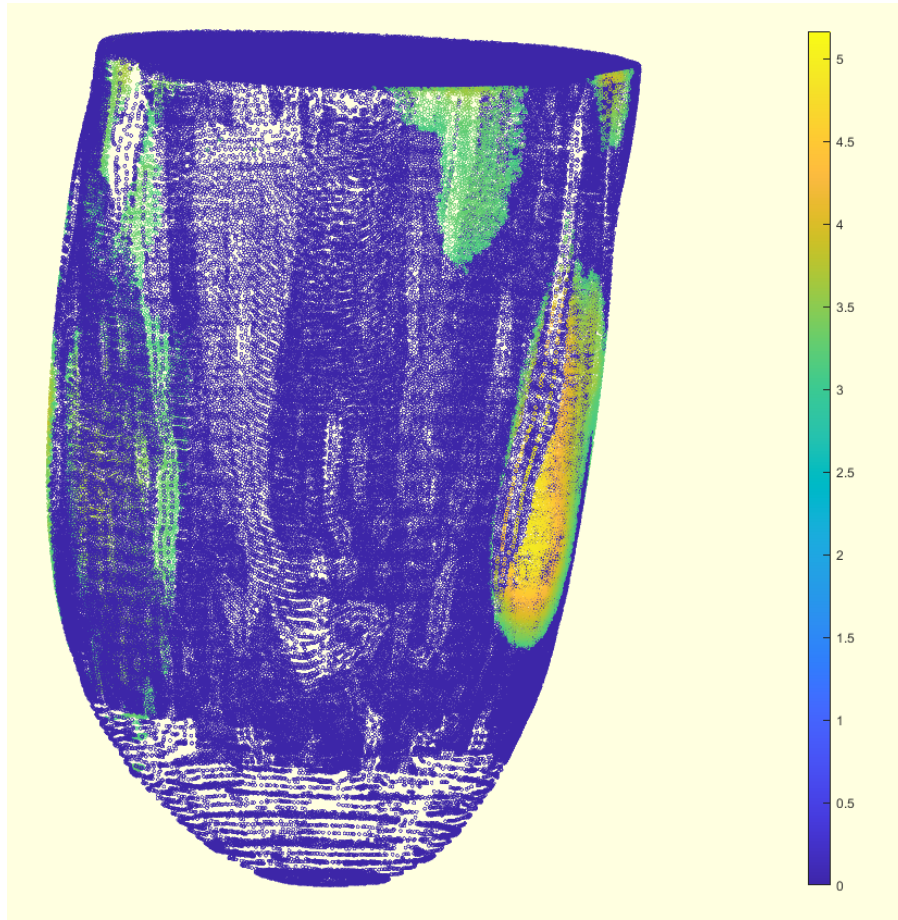


Figure 29: Triangle Midpoints (xq) with Filtered Interpolated Values (vq_n)

In order to eliminate the xq points with vq values lesser than 3 from the plot, a for loop was created, which assigned zero to the xq points when the associated filtered interpolated value (vq_n) is zero (Appendix 7) The Figure 30 demonstrates the filtered xq points with the filtered vq values (vq_n) on them.

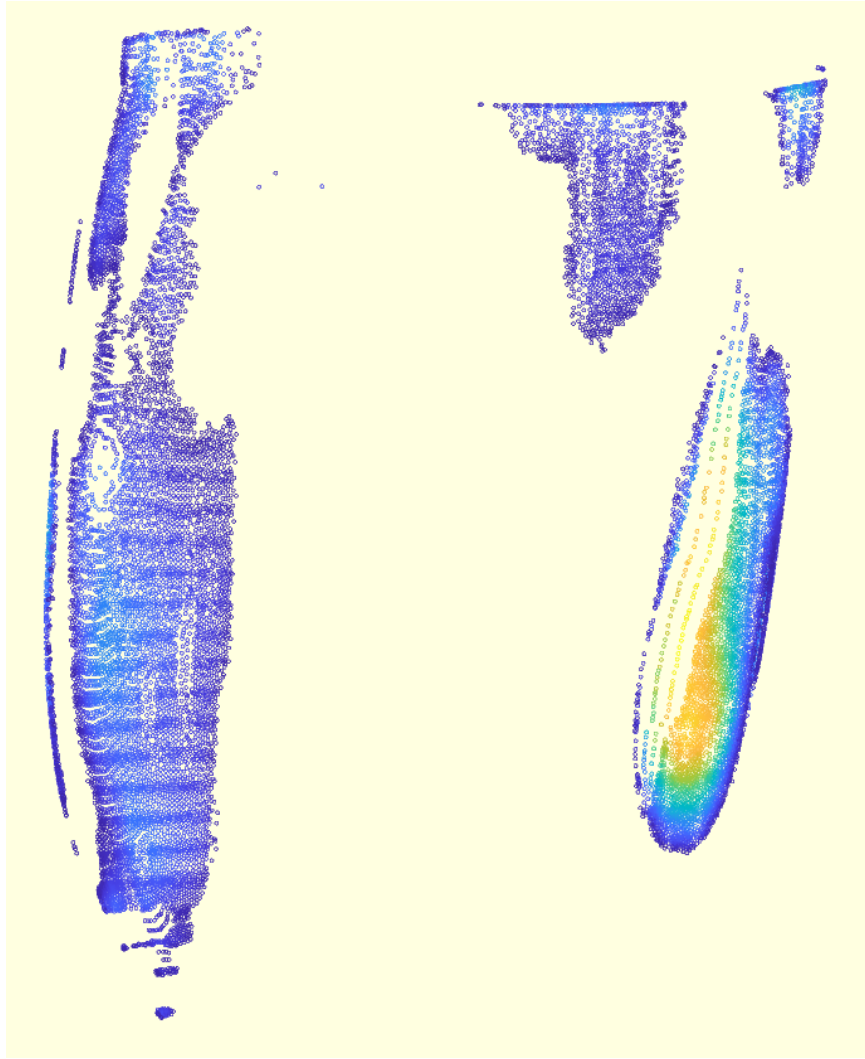


Figure 30: Filtered Triangle Midpoints (xq) with Filtered Interpolated Values (vq_n)

AREA OF THE DEFORMATION FIELD

The area related to the deformation field was calculated consequently obtaining the deformation field of the patient residual limb with an applied pressure of 30 mmHg via the MRI compatible sphygmomanometer.

The code on Appendix 8 was used to create a for loop in order to generate the variable *connectsR_n*, which included the triangulation of the filtered triangle midpoints (xq). This was

achieved using an if loop within the for loop to filter the *connectsR* values with non-zero filtered interpolated values (*vq_n*).

If the coordinates of the triangle are represented in $p(x_1, y_1, z_1)$, $q(x_2, y_2, z_2)$ and $r(x_3, y_3, z_3)$, the area of a triangle can be calculated using the following equation:

$$Area = \frac{1}{2} \sqrt{\begin{vmatrix} x_1 & x_2 & x_3 \\ y_1 & y_2 & y_3 \\ 1 & 1 & 1 \end{vmatrix}^2 + \begin{vmatrix} y_1 & y_2 & y_3 \\ z_1 & z_2 & z_3 \\ 1 & 1 & 1 \end{vmatrix}^2 + \begin{vmatrix} z_1 & z_2 & z_3 \\ x_1 & x_2 & x_3 \\ 1 & 1 & 1 \end{vmatrix}^2}$$

The required coordinates of triangles were found using a for loop, which recorded the coordinates within the output of the non-rigid registration (*registered*), when the *connectsR_n* was not equal to zero (when the value of *vq* was higher than 3) using the code on Appendix 9.

The contact areas at each of the compressed states (30 *mmHg*, 60 *mmHg* and 100 *mmHg*) were estimated for all three patients.

RESULTS

The project processed results related to three patients. The patient-specific soft tissue deformations in the residual limb were obtained for three patients.

SOFT TISSUE DEFORMATIONS OF THE FIRST PATIENT'S RESIDUAL LIMB UNDER COMPRESSIVE LOADS

The area in contact with the sphygmomanometer of the first patient was extracted as 476.45 cm^2 . Since, pressure can be identified as the force for an object that is spread over a surface area, the force applied at each of the compressed state was derived using the following formula:

$$F = PA$$

Equation 7

Where F = Force, P = Pressure, and A = Surface area.

The maximum tissue deformations measured at 30 mmHg , 60 mmHg and 100 mmHg were 4.9 mm , 5.4 mm , and 6.3 mm , respectively. It was assumed that the location of the maximum deformation coincided with the center of the area in contact with the inflated side of the sphygmomanometer. The collected soft tissue deformations of the residual limb were characterized by fitting a piecewise linear model to force-deformation data (Figure 33).

The Table 6 demonstrates the 50th, 70th and 90th percentile of soft tissue deformation related to the first patient for each compressed state.

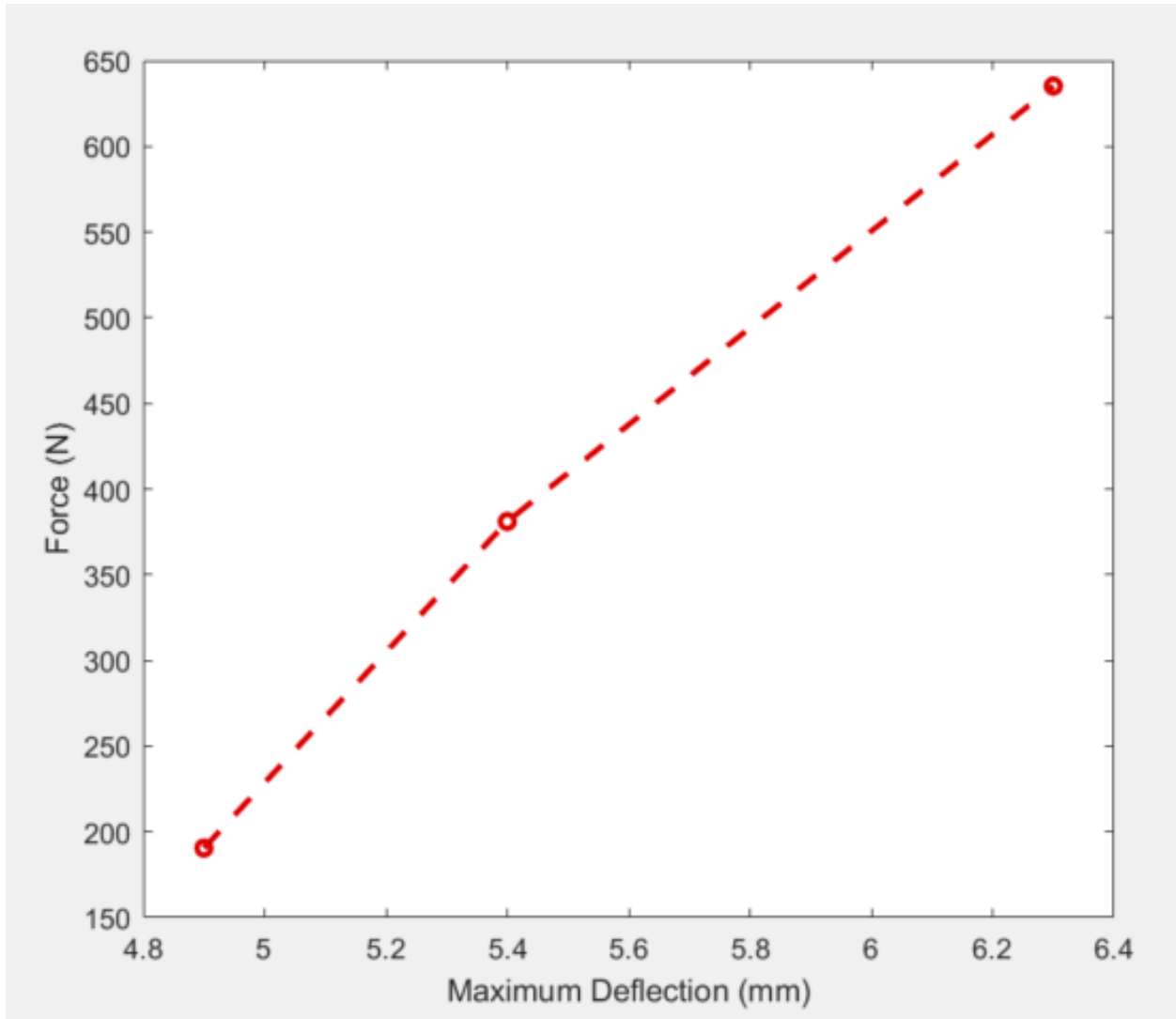


Figure 31: Maximum Soft Tissue Deflection vs Force Graph of the First Patient

Table 6: 50th, 70th and 90th percentile of Soft Tissue Deformation related to the First Patient

Percentile of Tissue Deformation (%)	At 30 mmHg	At 60 mmHg	At 100 mmHg
50	0.93 mm	1.05 mm	1.23 mm
70	2.75 mm	2.92 mm	3.16 mm
90	4.36 mm	5.15 mm	5.84 mm

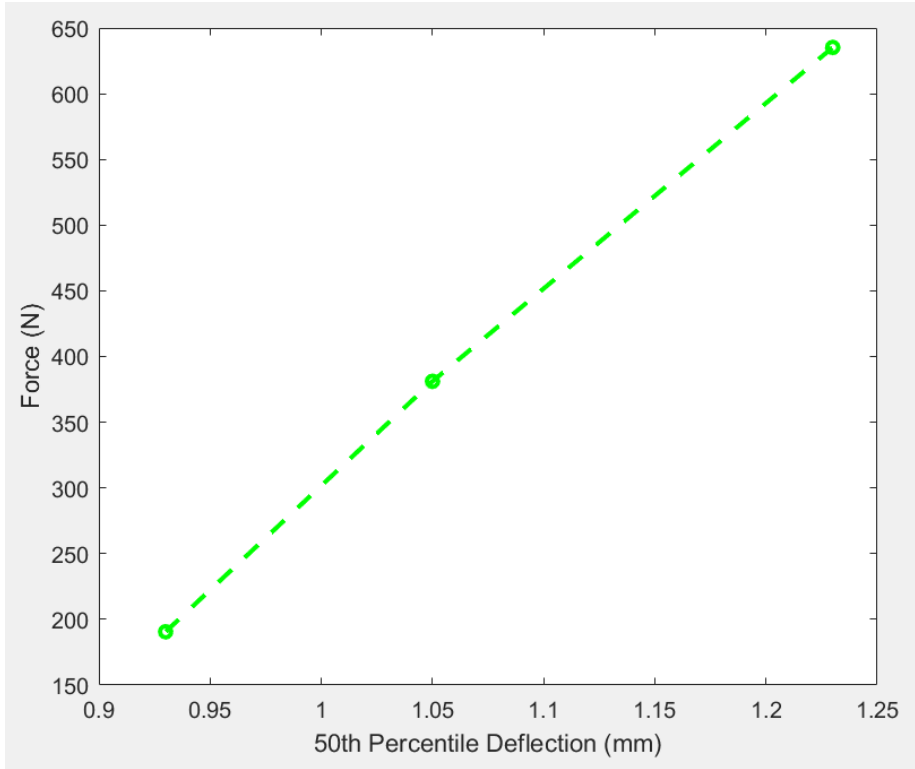


Figure 32: 50th Percentile of Soft Tissue Deflection vs Force Graph of the First Patient

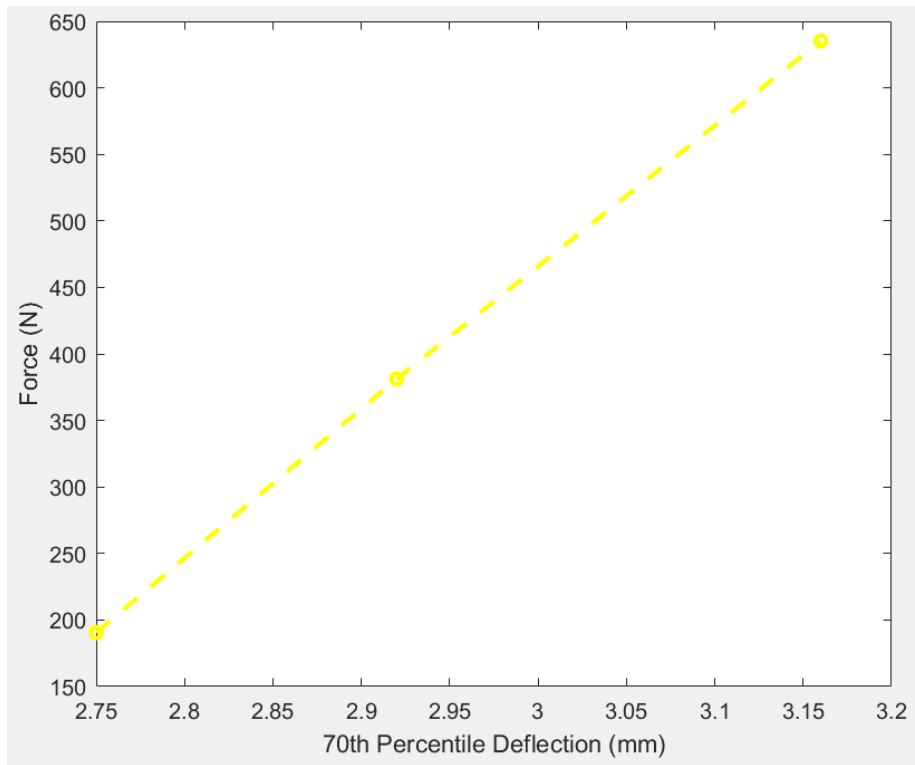


Figure 33: 70th Percentile of Soft Tissue Deflection vs Force Graph of the First Patient

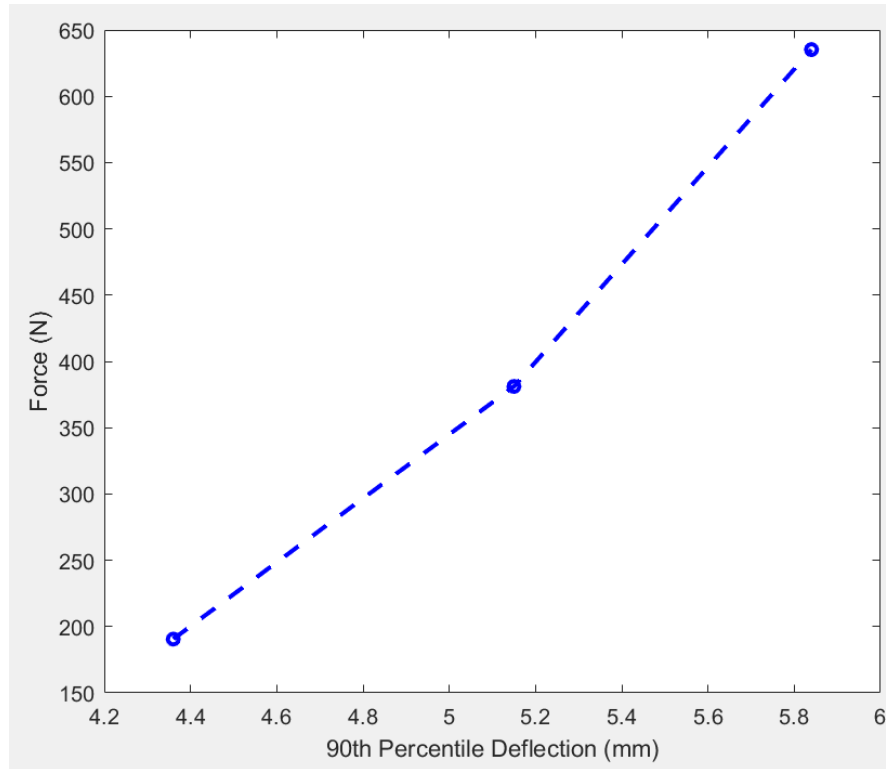


Figure 34: 90th Percentile of Soft Tissue Deflection vs Force Graph of the First Patient

Figure 34, Figure 35, and Figure 36 demonstrates the 50th, 70th and 90th percentiles of soft tissue deformations with respect to the calculated forces of the first patient. Figure 37 demonstrates each percentile of soft tissue deformation related to the first patient on the same plot.

Further, the Figure 38 demonstrates the areas of deformation related to each percentile: red indicates the 90th percentile of the tissue deformation, yellow areas indicate the 70th percentile of tissue deformation and green areas indicate 50th percentiles of the tissue deformation.

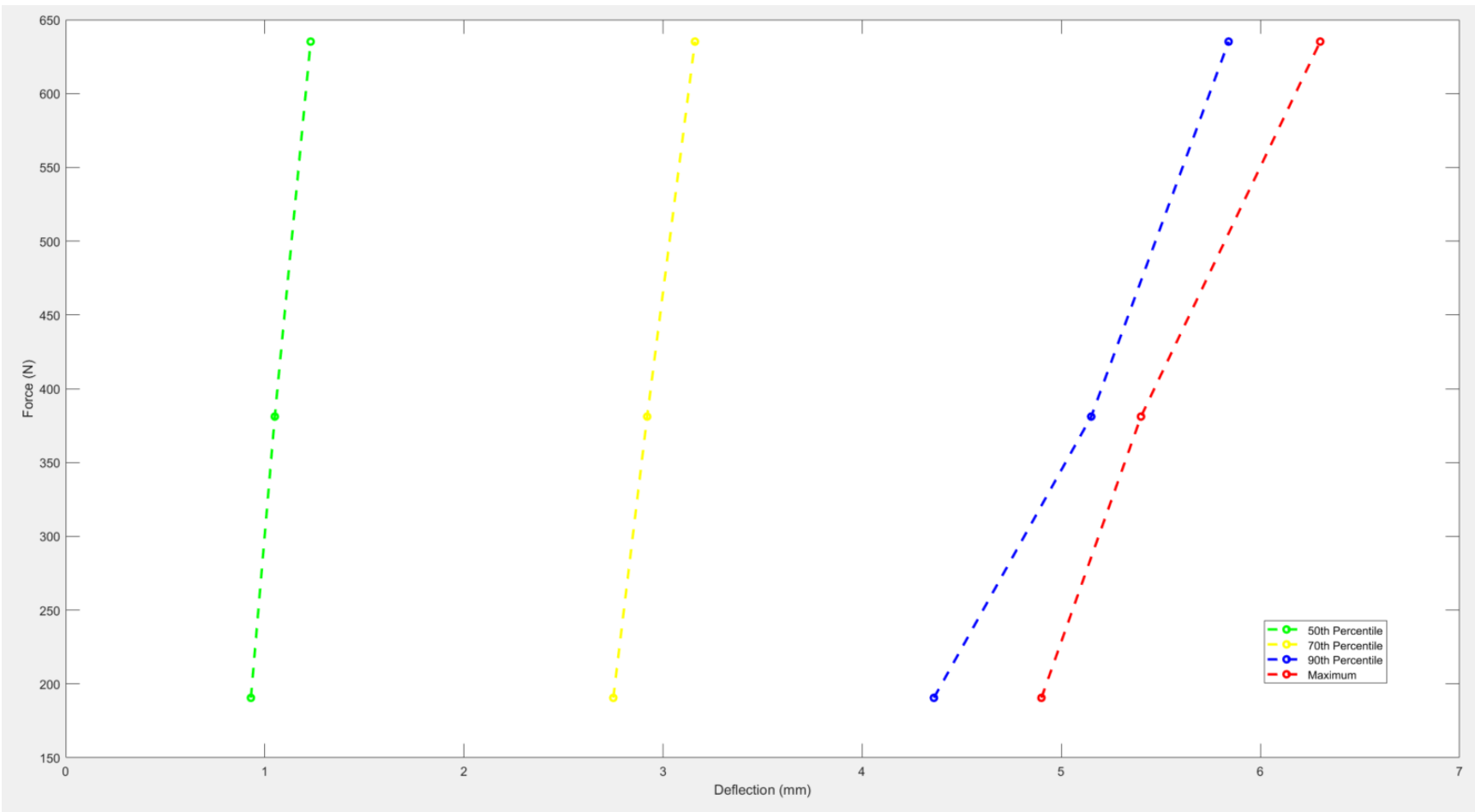


Figure 35: 50th, 70th and 90th percentile of Soft Tissue Deformation vs Force Graph related to the First Patient

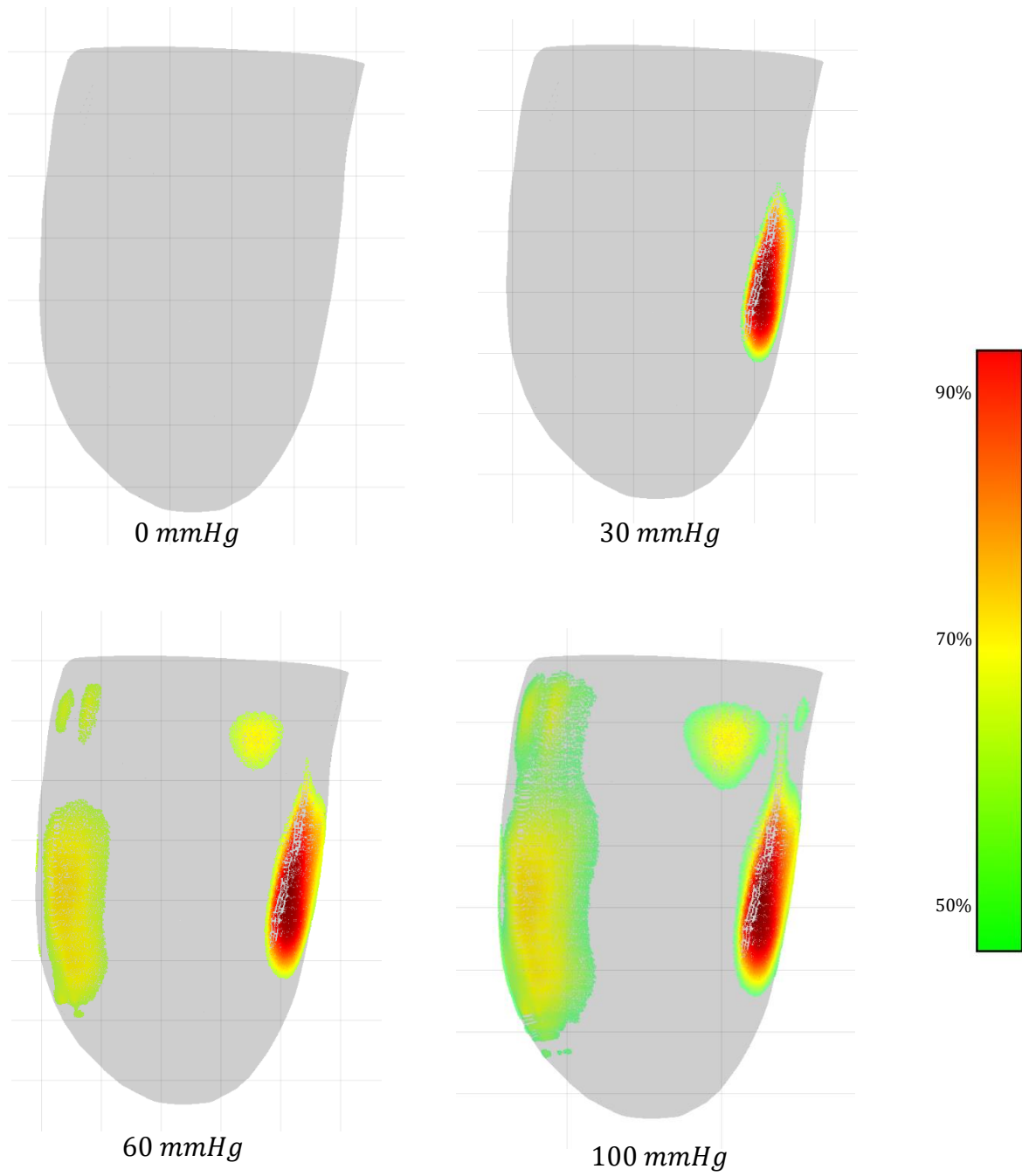


Figure 36: The Areas of Soft Tissue Deformation related to 50th, 70th and 90th Percentile of the First Patient

SOFT TISSUE DEFORMATIONS OF THE SECOND PATIENT'S RESIDUAL LIMB UNDER COMPRESSIVE LOADS

The area in contact with the sphygmomanometer of the second patient was extracted as 512.35 cm^2 .

The maximum tissue deformations measured at 30 mmHg , 60 mmHg and 100 mmHg were 4.8 mm , 5.3 mm , and 6.2 mm , respectively. Assuming that the location of the maximum deformation coincided with the center of the area in contact with the inflated side of the sphygmomanometer, the collected soft tissue deformations of the second patient's residual limb were characterized by fitting a piecewise linear model to force-deformation data (Figure 39).

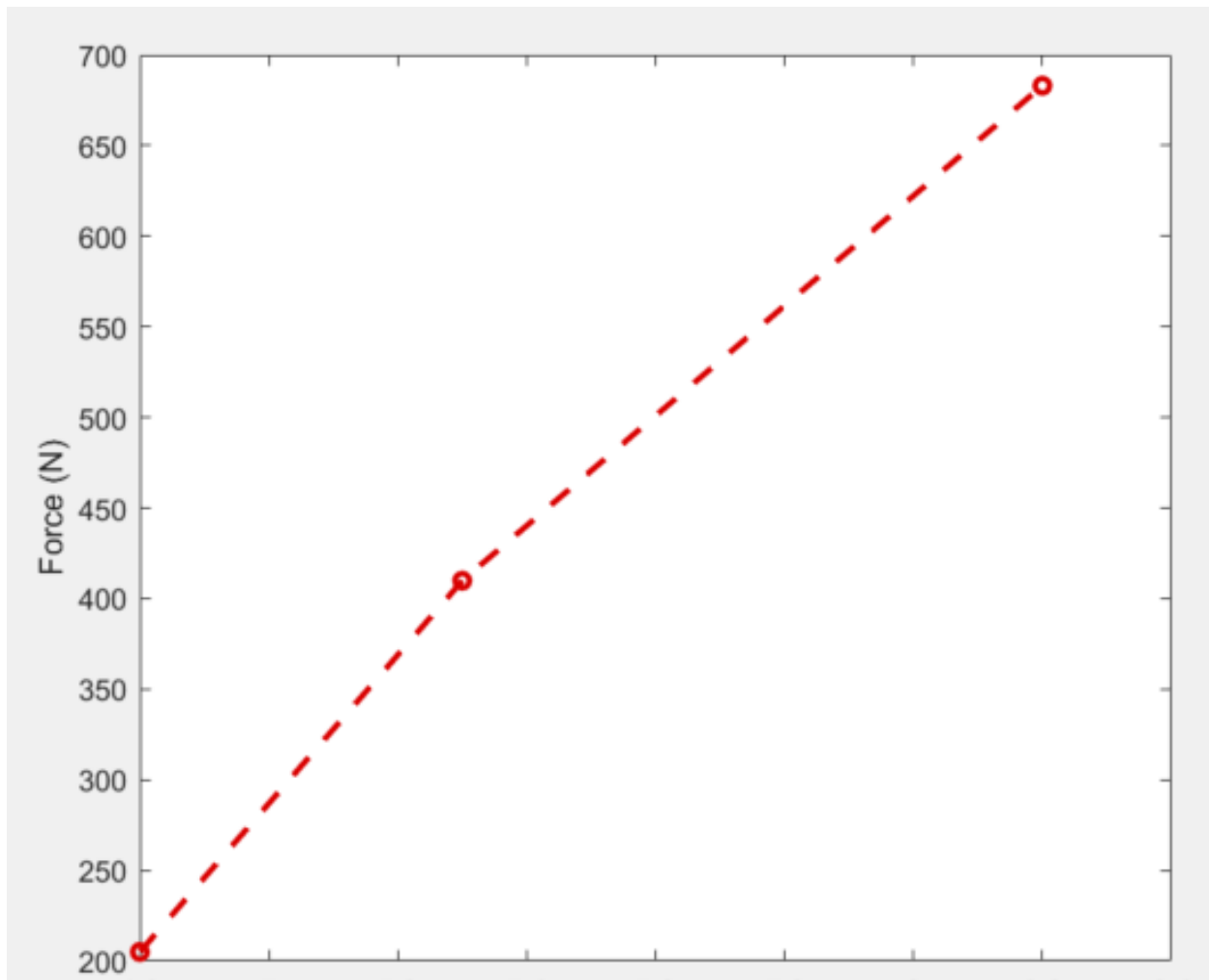


Figure 37: Maximum Soft Tissue Deflection vs Force Graph of the Second Patient

The Table 7 demonstrates the 50th, 70th and 90th percentile of soft tissue deformation related to the second patient for each compressed state.

Table 7: 50th, 70th and 90th percentile of Soft Tissue Deformation related to the Second Patient

Percentile of Tissue Deformation (%)	At 30 mmHg	At 60 mmHg	At 100 mmHg
50	1.24 mm	1.65 mm	1.96 mm
70	2.84 mm	3.16 mm	3.82 mm
90	4.45 mm	4.92 mm	6.01 mm

Figure 40, Figure 41, and Figure 42 demonstrates the 50th, 70th and 90th percentiles of soft tissue deformations with respective to the calculated forces of the second patient. Figure 43 demonstrates each percentile of soft tissue deformation related to the second patient on the same plot.

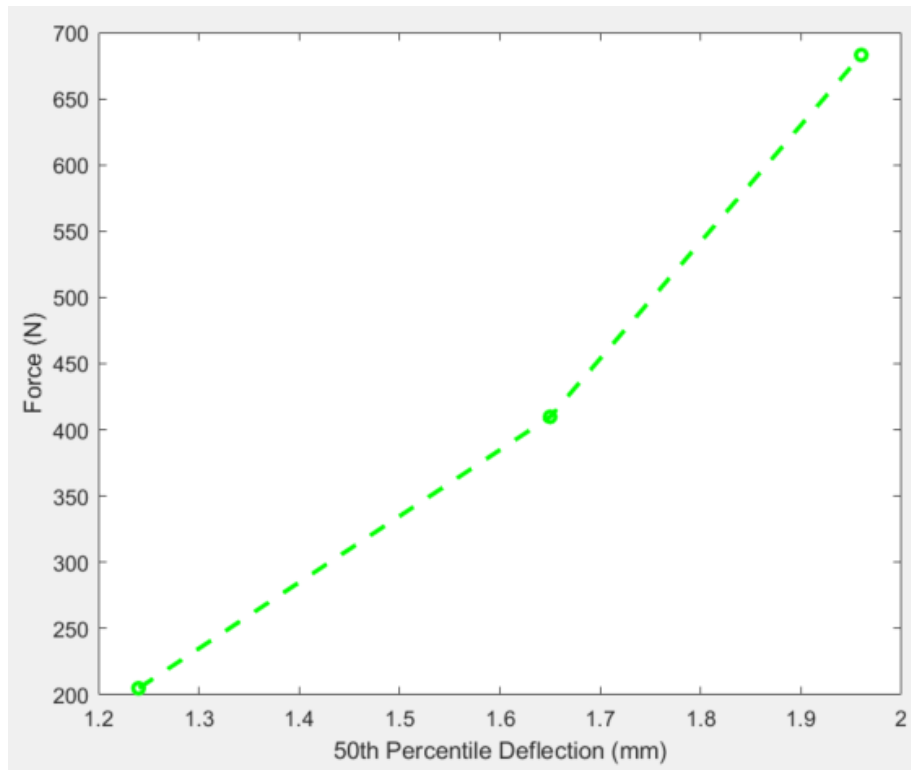


Figure 38: 50th Percentile of Soft Tissue Deflection vs Force Graph of the Second Patient

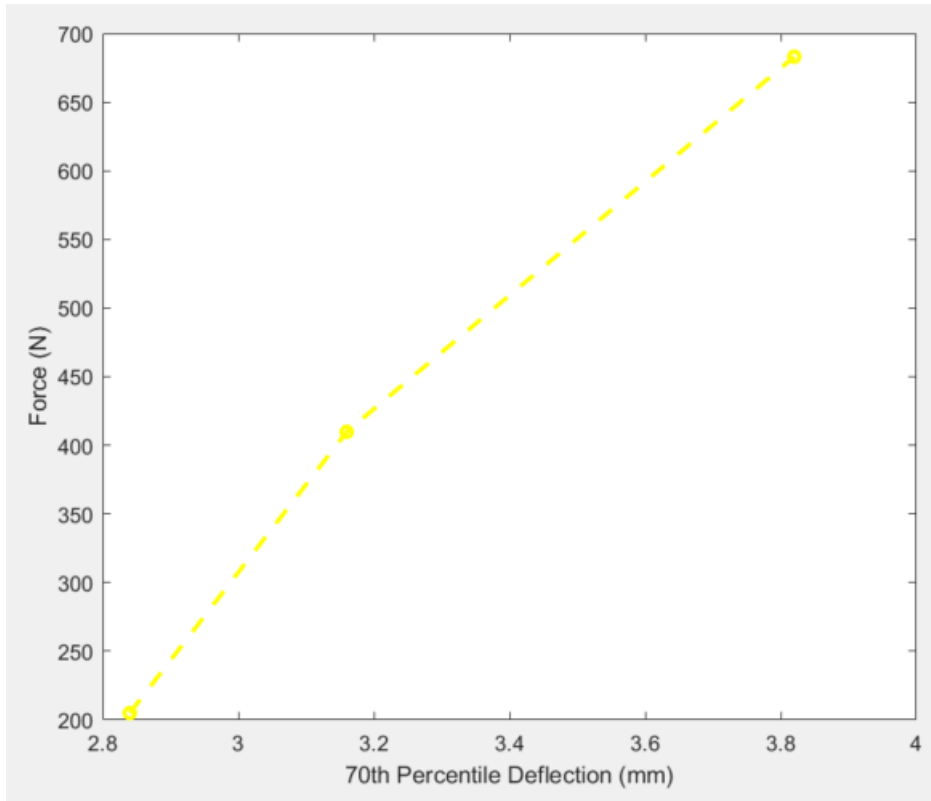


Figure 39: 70th Percentile of Soft Tissue Deflection vs Force Graph of the Second Patient

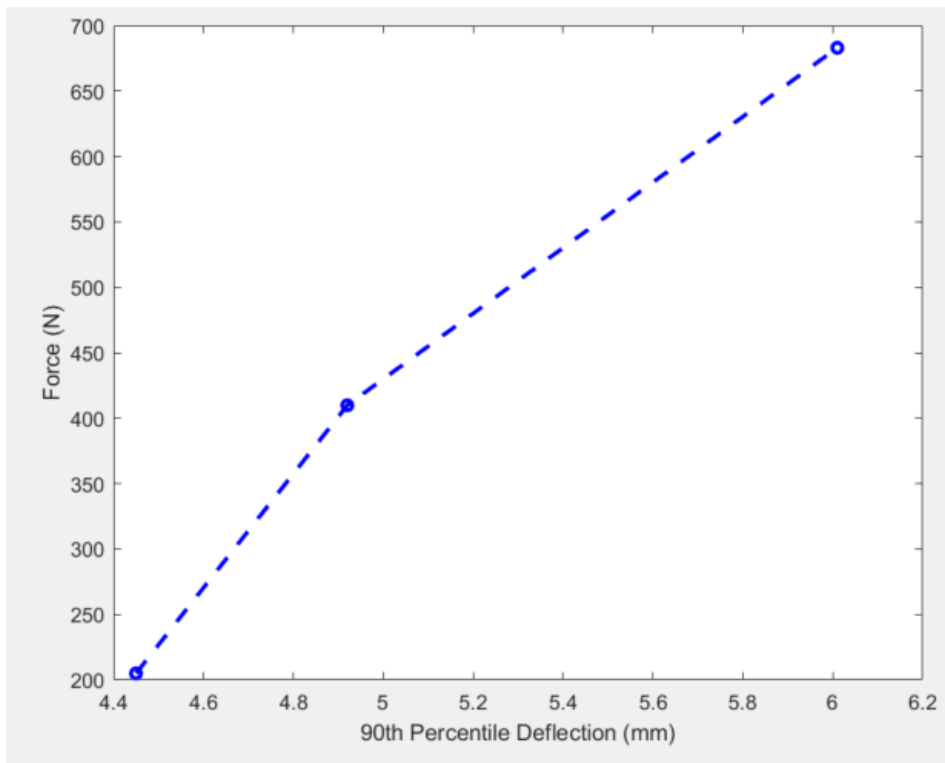


Figure 40: 90th Percentile of Soft Tissue Deflection vs Force Graph of the Second Patient

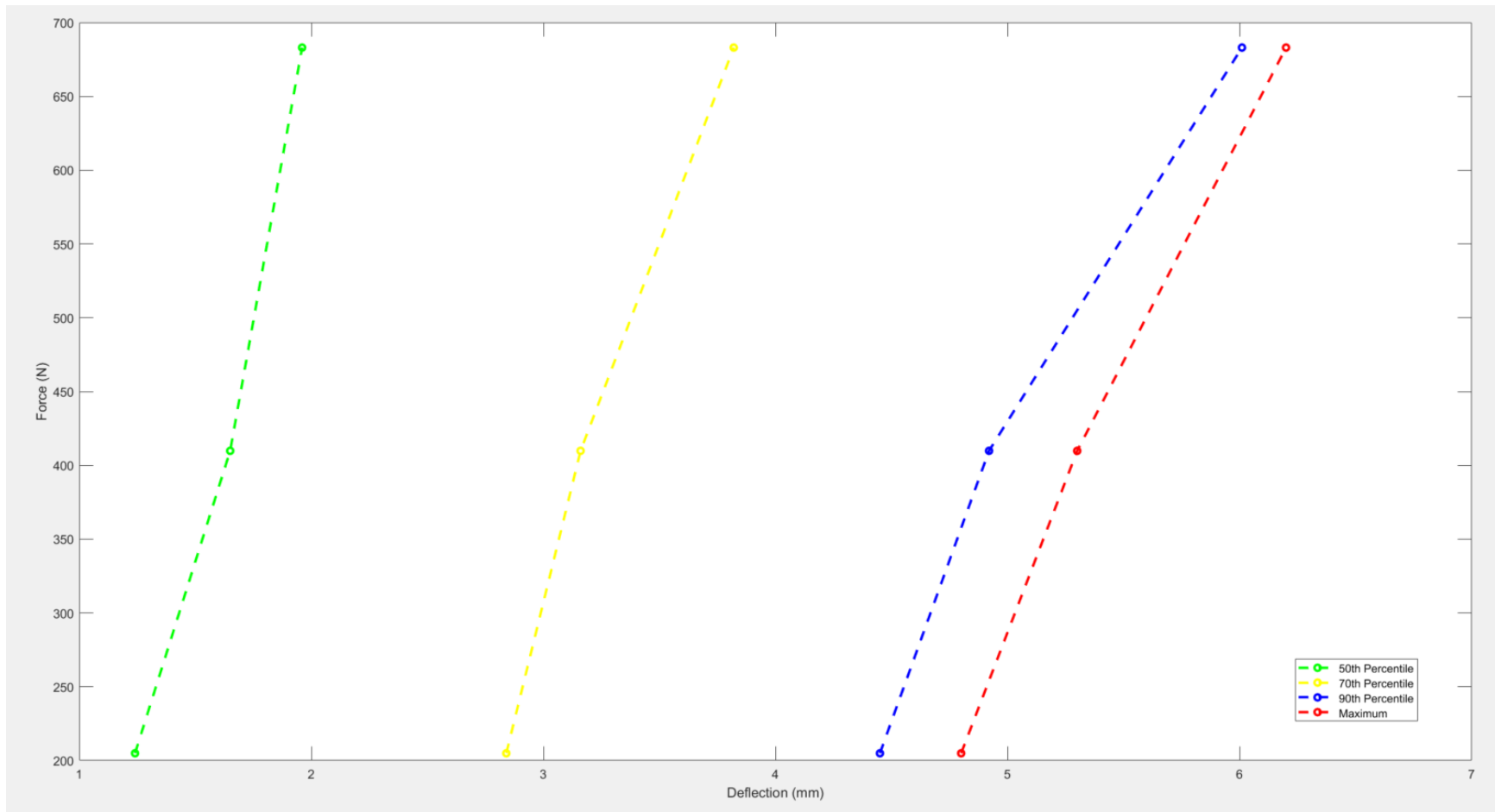


Figure 41: 50th, 70th and 90th percentile of Soft Tissue Deformation vs Force Graph related to the Second Patient

Figure 44 demonstrates the areas of deformation of the second patient related to each percentile: red indicates the 90th percentile of the tissue deformation, yellow areas indicate the 70th percentile of tissue deformation and green areas indicate 50th percentiles of the tissue deformation.

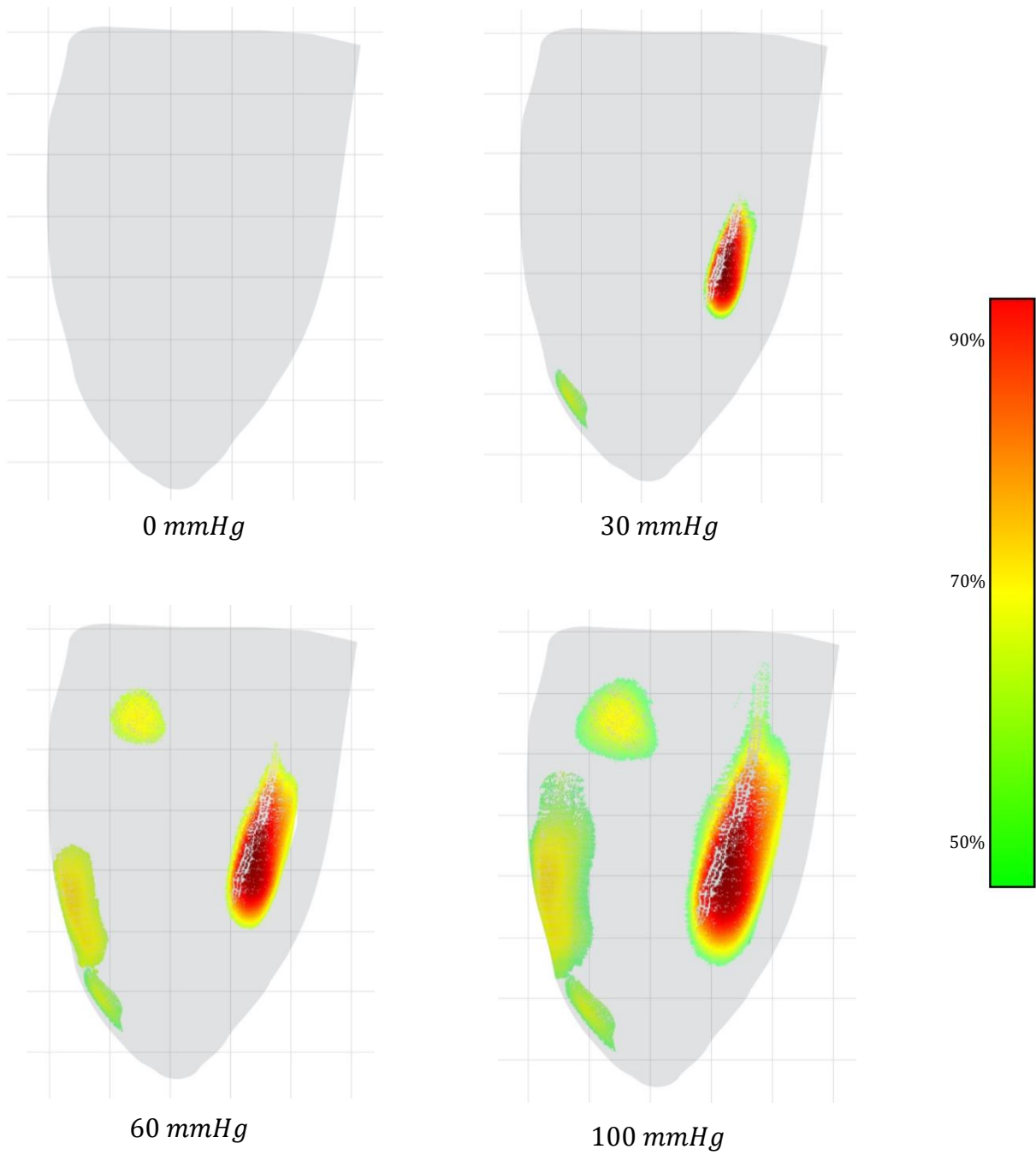


Figure 42: The Areas of Soft Tissue Deformation related to 50th, 70th and 90th Percentile of the Second Patient

SOFT TISSUE DEFORMATIONS OF THE THIRD PATIENT'S RESIDUAL LIMB UNDER COMPRESSIVE LOADS

The area in contact with the sphygmomanometer of the third patient was extracted as 426.72 cm^2 .

The maximum tissue deformations measured at 30 mmHg , 60 mmHg and 100 mmHg were 5.9 mm , 6.5 mm , and 7.8 mm , respectively. The collected soft tissue deformations of the third patient's residual limb were characterized by fitting a piecewise linear model to force-deformation data, assuming that the location of the maximum deformation coincided with the center of the area in contact with the inflated side of the sphygmomanometer (Figure 45).

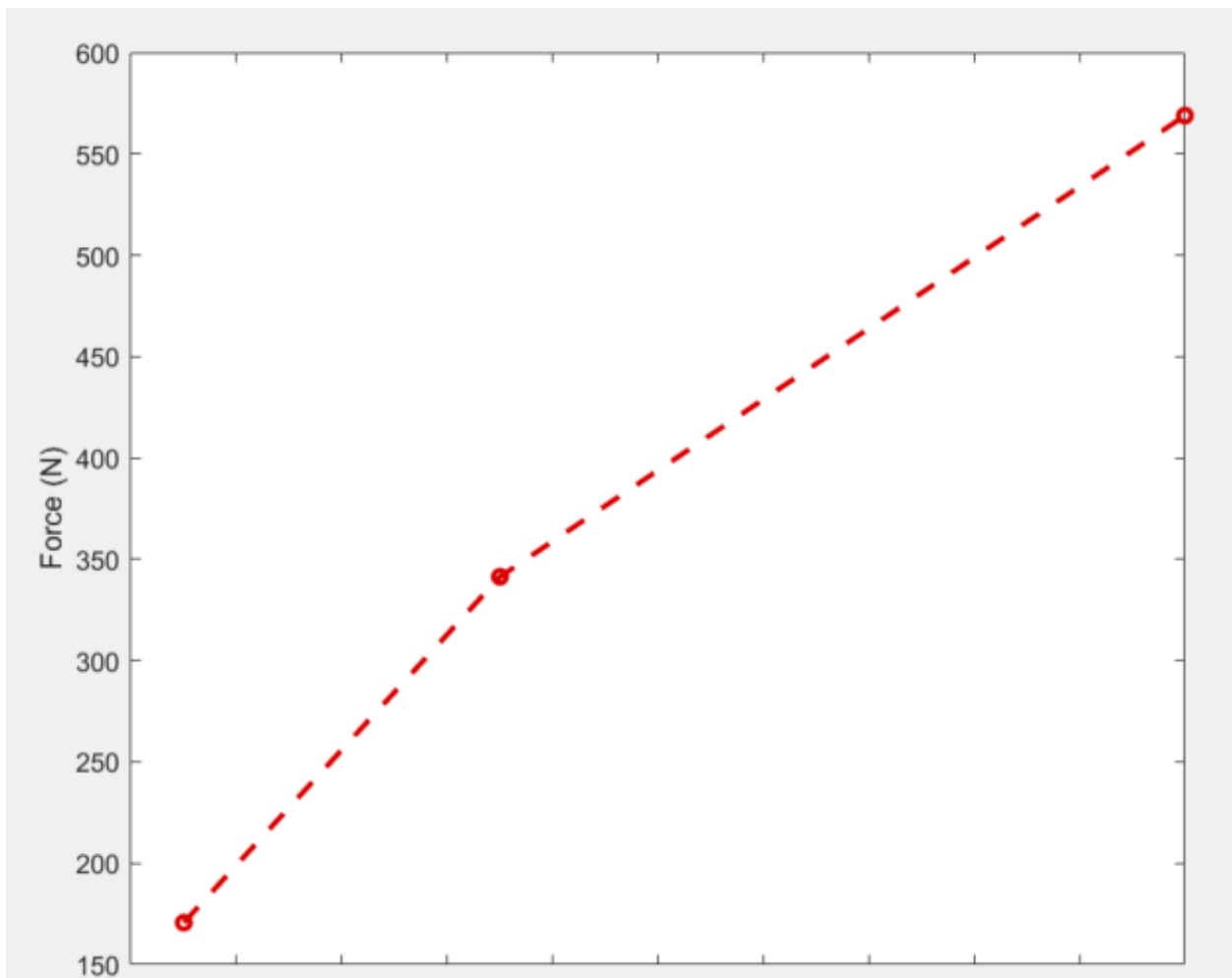


Figure 43: Maximum Soft Tissue Deflection vs Force Graph of the Third Patient

The Table 8 demonstrates the 50th, 70th and 90th percentile of soft tissue deformation related to the third patient for each compressed state.

Table 8: 50th, 70th and 90th percentile of Soft Tissue Deformation related to the Third Patient

Percentile of Tissue Deformation (%)	At 30 mmHg	At 60 mmHg	At 100 mmHg
50	1.73 mm	2.65 mm	2.85 mm
70	4.52 mm	4.92 mm	6.90 mm
90	5.43 mm	6.12 mm	7.46 mm

Figure 46, Figure 47, and Figure 48 demonstrates the 50th, 70th and 90th percentiles of soft tissue deformations with respect to the calculated forces of the third patient. Figure 49 demonstrates each percentile of soft tissue deformation related to the third patient on the same plot.

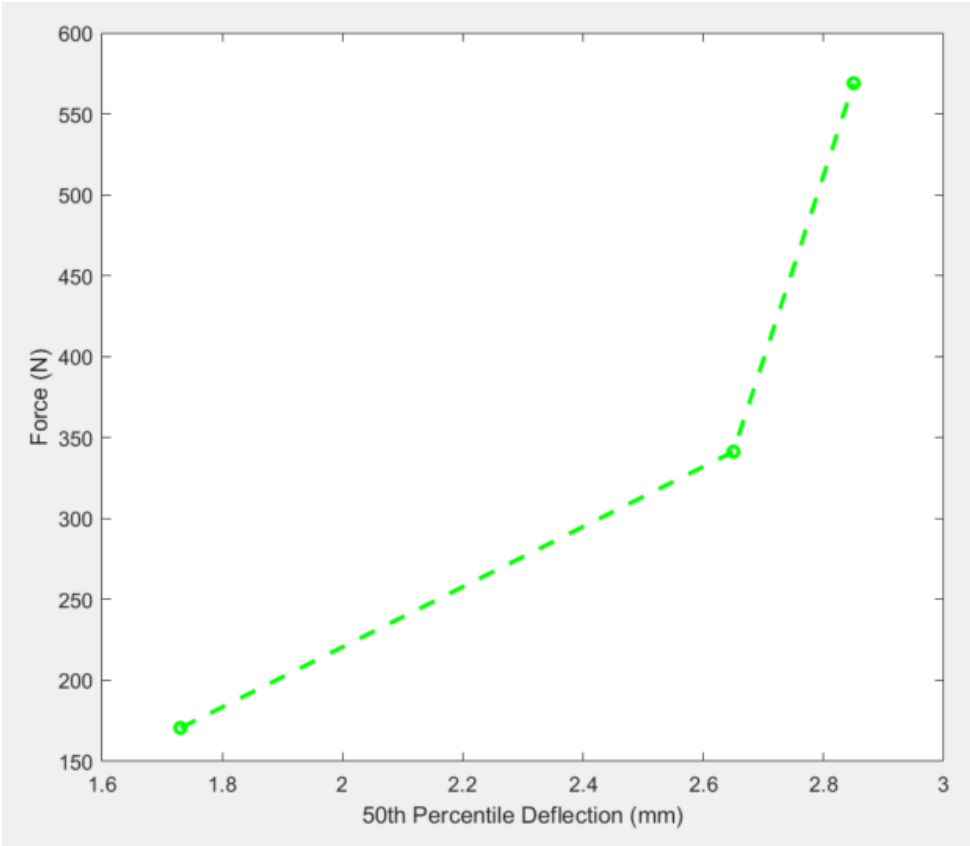


Figure 44: 50th Percentile of Soft Tissue Deflection vs Force Graph of the Third Patient

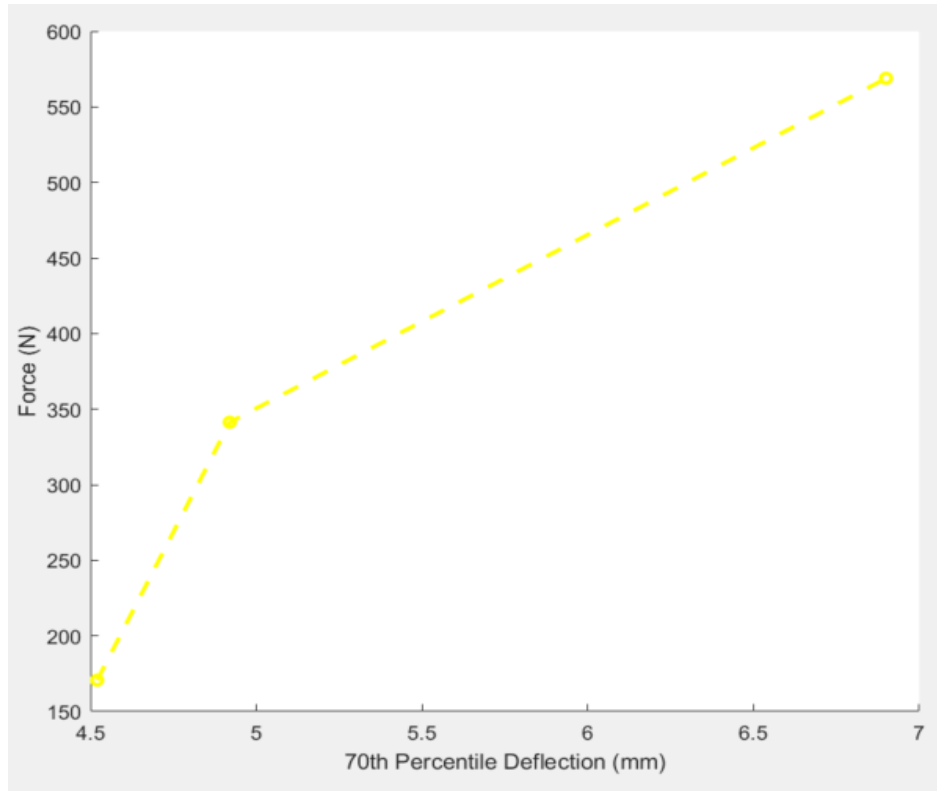


Figure 45: 70th Percentile of Soft Tissue Deflection vs Force Graph of the Third Patient

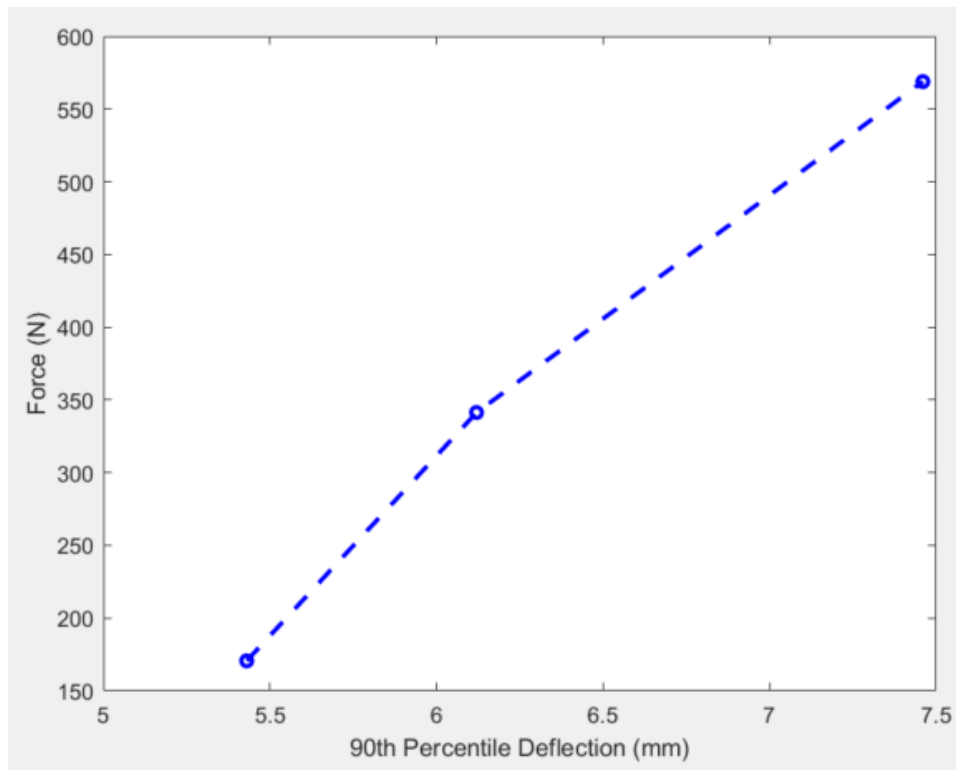


Figure 46: 90th Percentile of Soft Tissue Deflection vs Force Graph of the Third

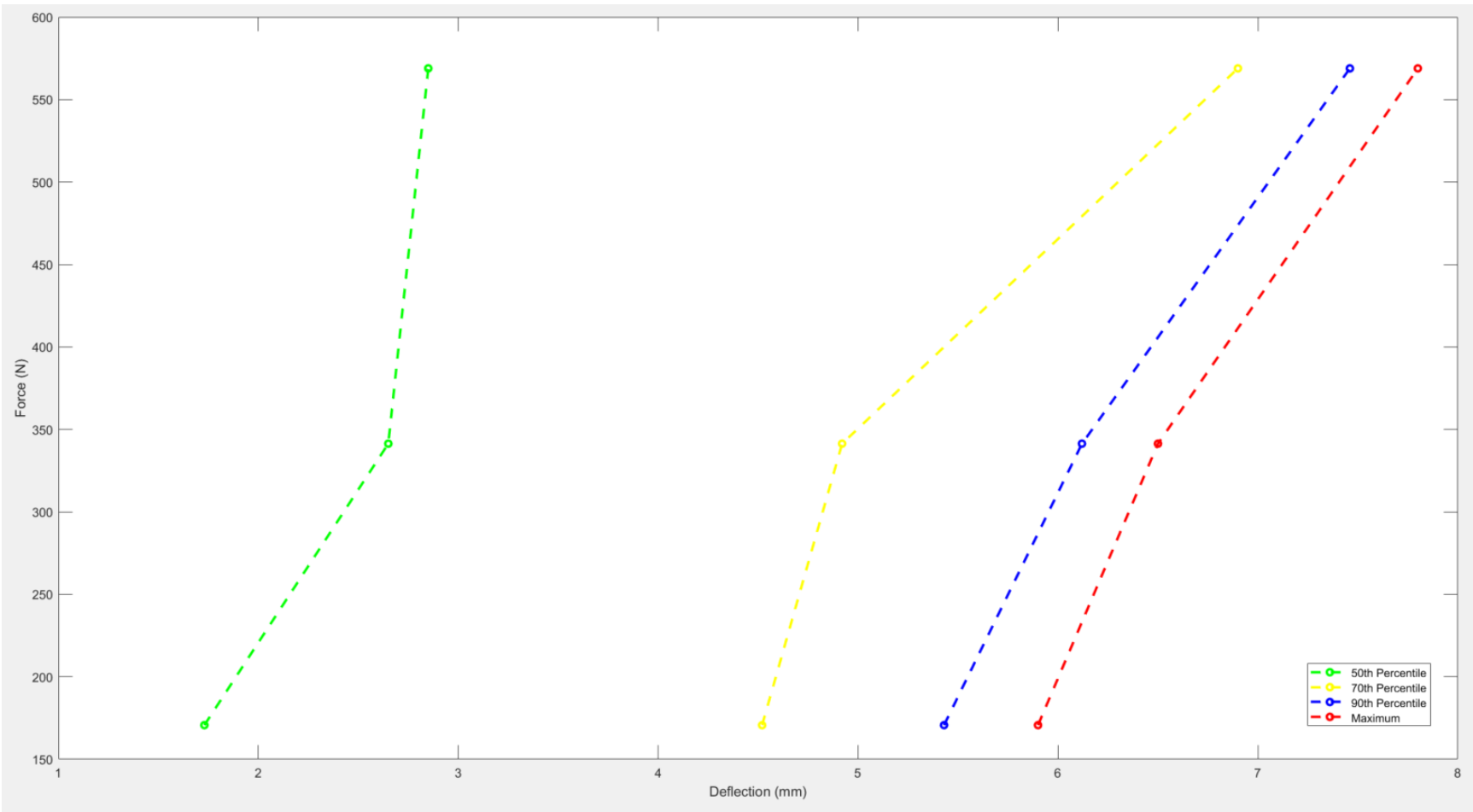


Figure 47: 50th, 70th and 90th percentile of Soft Tissue Deformation vs Force Graph related to the Third Patient

Figure 50 demonstrates the areas of deformation of the third patient related to each percentile: red indicates the 90th percentile of the tissue deformation, yellow areas indicate the 70th percentile of tissue deformation and green areas indicate 50th percentiles of the tissue deformation.

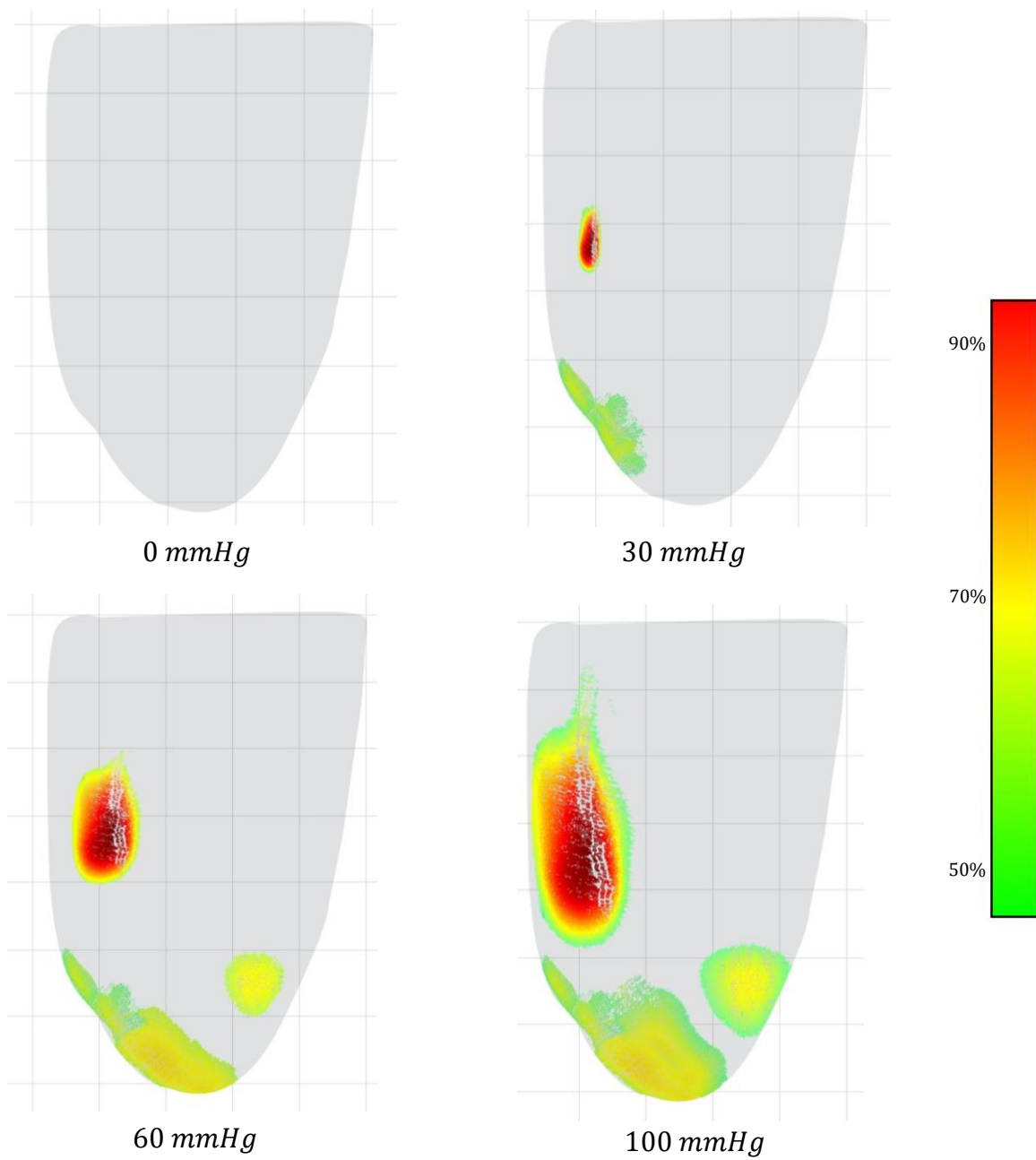


Figure 48: The Areas of Soft Tissue Deformation related to 50th, 70th and 90th Percentile of the Third Patient

DISCUSSION

Soft tissues are incompressible, anisotropic materials which has a nonlinear mechanical response to loads. Most of the researchers has modelled the residual limb soft tissues either as linear elastic 2005 (Zhang and Roberts 2000; Zachariah and Sanders 2000; Wu et al. 2003; Lin et al. 2004; Lee et al. 2004; Jia et al. 2004; Jia et al. 2005; Ramírez and Vélez 2012; Velez Zea et al. 2015; Cagle et al. 2018) or as hyperelastic (Portnoy et al. 2008; Portnoy et al. 2009; Portnoy et al. 2011; Lacroix & Patiño 2011; Zhang et al. 2013).

The focus of the study was to estimate patient-specific soft tissue deformations of the residual limb using medical image data acquired while performing quasi-static loading experiments. The estimated subject-specific soft tissue deformations are related to a bulk tissue structure in the residual limb and could only be considered as true for the given structure.

The material properties could be easily defined through a stress-strain curve, rather than a force-deflection curve. The relationship between the four variables of stress, strain, force, and deflection could be shown through the following formulars:

$$\sigma = \frac{F}{A}$$

Equation 8

$$\varepsilon = \frac{e}{l}$$

Equation 9

Where, σ = Stress, F = Force, A = Area, ε = Strain, e = Deflection, and l = Initial length

Even though the stresses were known as 3999.67 Nm^{-2} (at pressure 30 mmHg), 7999.32 Nm^{-2} (at pressure 60 mmHg) and 13332.24 Nm^{-2} (at pressure 100 mmHg), the strain was not able to be computed with the complications arose in detecting the initial length.

The soft tissue deformation related to each patient was obtained and presented as a series of point deformations corresponding to the triangulation midpoints of the residual limb mesh generated through segmentation. Since there was no exact definition to calculate the initial length with relative to these point deformations, the data was presented through force-deflection curves.

Figure 51 demonstrates the force-deflection curves considering the maximum deflection for the three patients. The applied forces have been varied between the patients due to the differences in the contact area of the sphygmomanometer with the patient residual limb. It could be seen that the force-deflection plots indicate unique shapes for each patient confirming the discrepancies between the soft tissue material properties between patients.

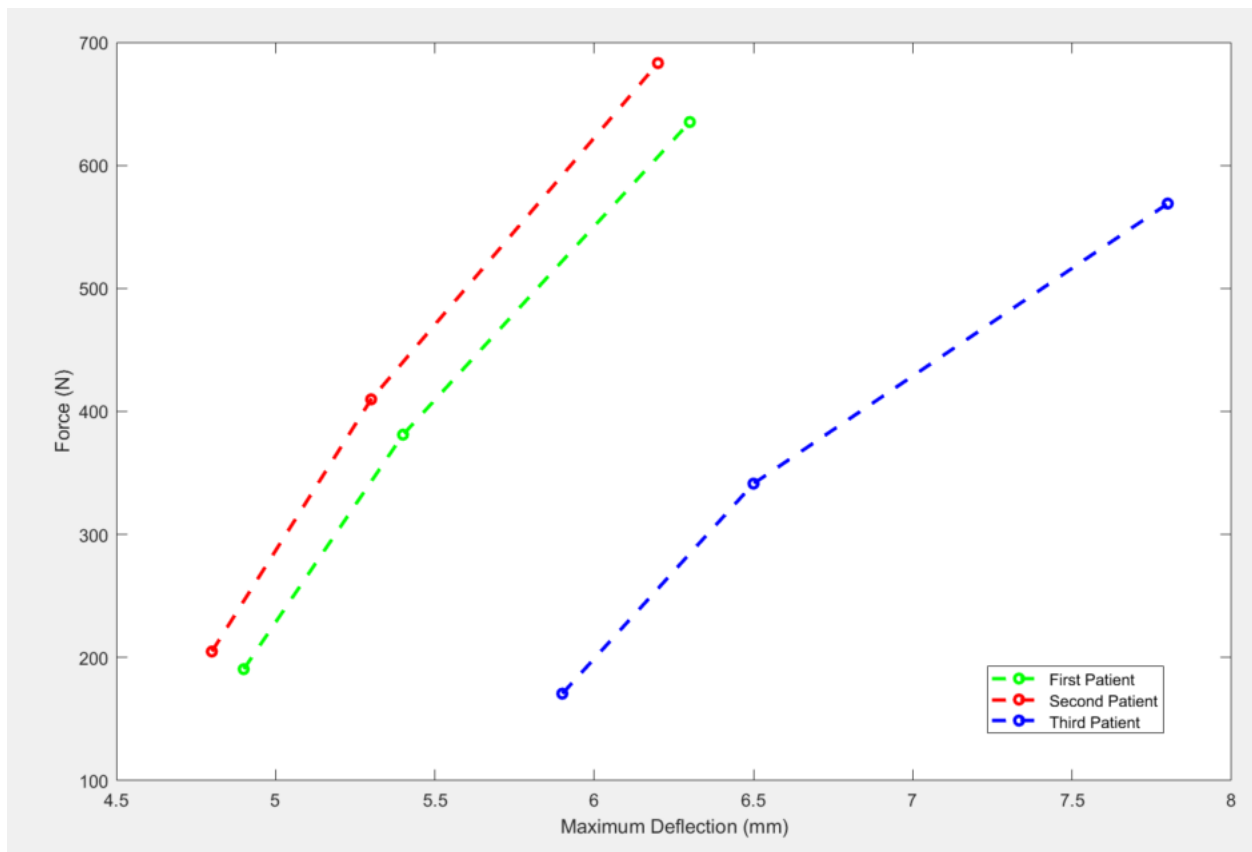


Figure 49: Maximum Soft Tissue Deflection vs Force Graph for the Three Patients

Further, it could be seen that the amount of soft tissue deformation related to the third patient is significantly higher compared to the first and second patients. Even though the initial force is between the range of 165 N - 205 N with a variance approximately of 40 N , the deformations of the patients have ranged from 4.8 mm to 5.9 mm . While the maximum deformation due to the initial force has varied around 0.1 mm among the first two patients, there is a considerable difference of almost 1 mm between the third patient and the other patients.

The third patient's residual limb was unusual as it included a portion of flesh from the heel pad. The surgeons have cut the heel pad and inserted on to the stump of the patient, as the patient had required more flesh on the stump to be acceptable for prosthesis. Thus, there could be a significant variation in the composition in the residual limb soft tissues of the third patient with relative to the other two patients. This change in residual limb soft tissue composition could be recognized as a potential reason for the deviation of the third patient's residual limb soft tissue material properties with respect to the other two patients.

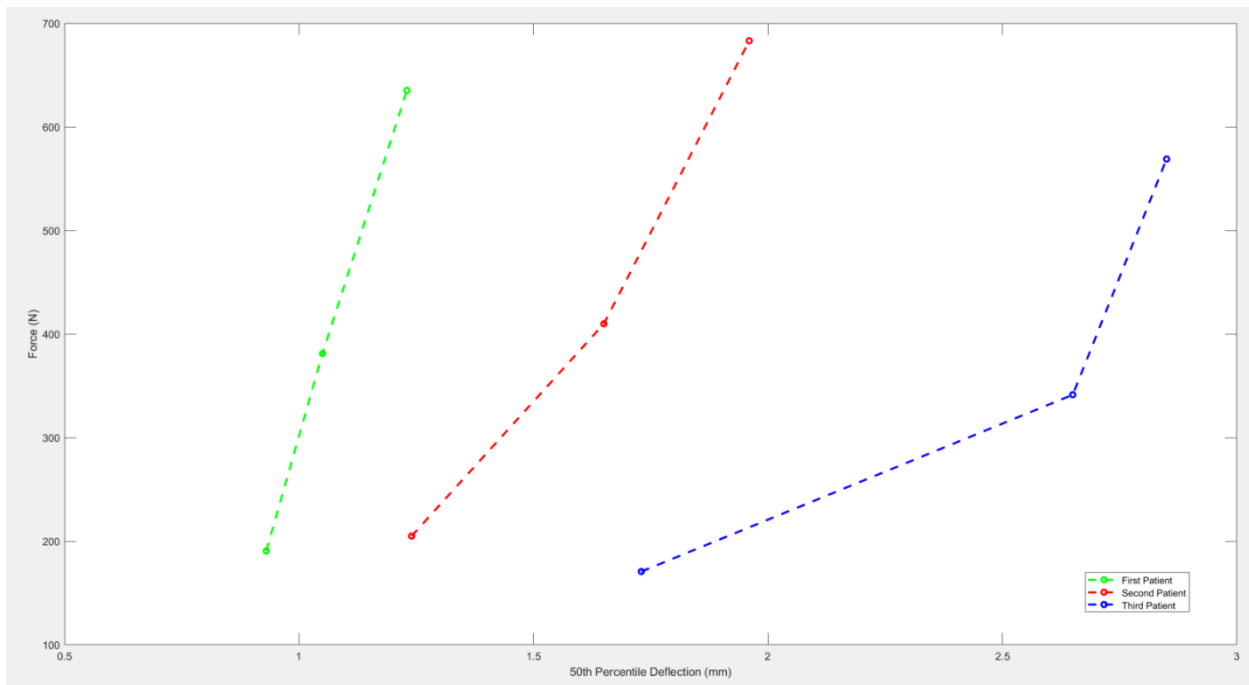


Figure 50: 50th Percentile of Soft Tissue Deflection vs Force Graph for the Three Patients

Figure 52, Figure 53, and Figure 54 demonstrates the force-deflection curves considering the 50th percentile of soft tissue deformation, 70th percentile of soft tissue deformation, and 90th percentile of soft tissue deformation, respectively for the three patients.

According to the Figure 52, the deformation differences between the first and the second patient are approximately at $0.7mm$, $0.6mm$, and $0.7mm$ for each force value. The deformation differences between the second and the third patient are at $0.5mm$, $1mm$, and $0.9mm$ for each force value. Thus, the deviation between soft tissue deformation among the three patients are not clearly apparent at the 50th percentile of soft tissue deformation relative to the maximum soft tissue deformation.

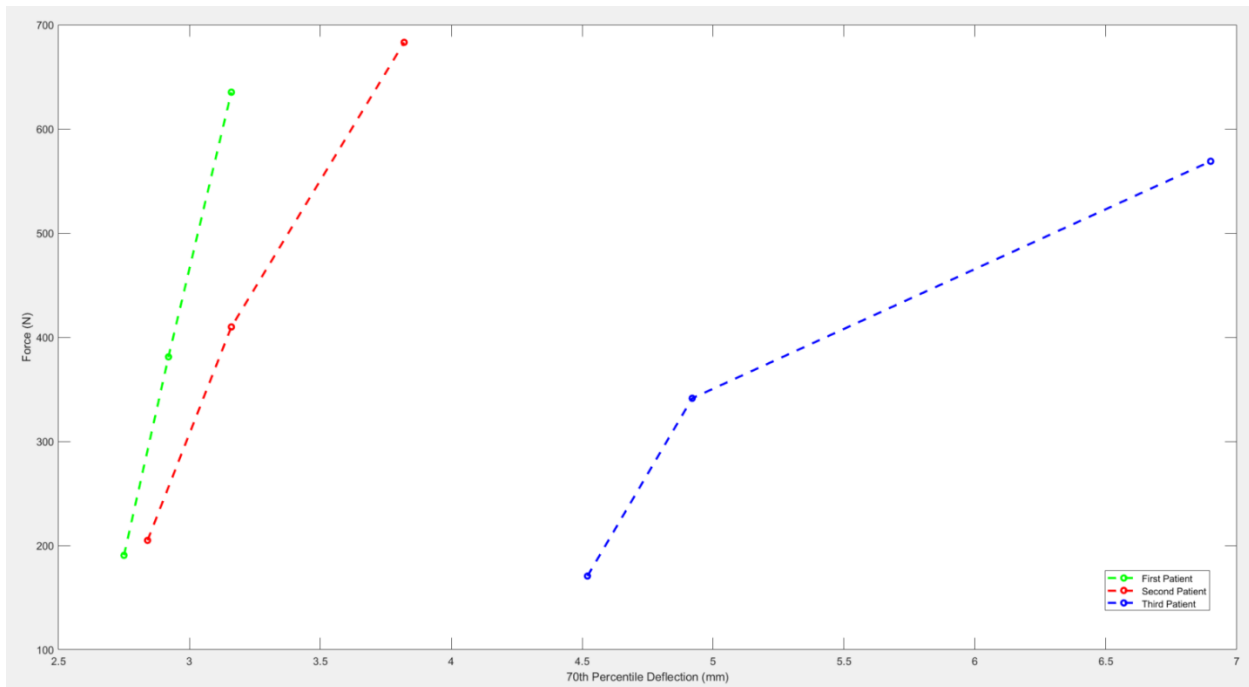


Figure 51: 70th Percentile of Soft Tissue Deflection vs Force Graph for the Three Patients

According to the Figure 53, the deformation differences between the first and the second patient are approximately at $0.1mm$, $0.2mm$, and $0.7mm$ for each force value. The deformation differences between the second and the third patient are approximately at $1.7mm$, $1.8mm$, and $3.1mm$ for each force value. The deformation differences between the first and the third patient are approximately at $1.8mm$, $2mm$, and $3.7mm$ for each force value.

Thus, it could be clearly seen that the deformation difference between the first and the second patient is significantly minor compared to the deformation difference between the third and the other two patients. The variation of residual limb soft tissue material properties of the third patient with relative to the other two patients become more noticeable at the 70th percentile of soft tissue deformation.

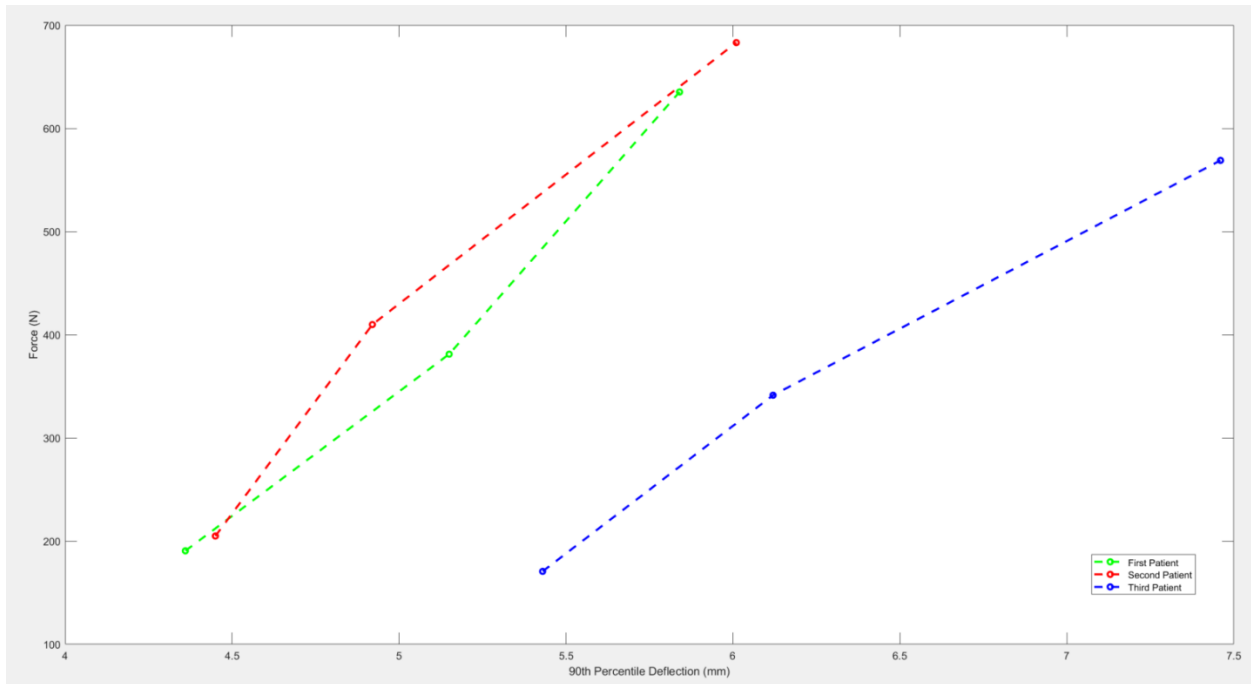


Figure 52: 90th Percentile of Soft Tissue Deflection vs Force Graph for the Three Patients

According to the Figure 54, the deformation differences between the first and the second patient are approximately at $0.1mm$, $0.2mm$, and $0.2mm$ for each force value. The deformation differences between the second and the third patient are approximately at $1mm$, $1.2mm$, and $1.5mm$ for each force value. The deformation differences between the first and the third patient are approximately at $1mm$, $1mm$, and $1.6mm$ for each force value.

It could be seen that towards the higher percentiles of soft tissue deformation, the second patient's residual limb soft tissues deform lower than the first patient's residual limb soft tissues. Further, the deformation difference between the third patient and other two patients has increased confirming the deviation in residual limb soft tissue material properties of the third patient with the heel pad.

A study designed to compare the morphology and biomechanical response of soft tissues in the limb to mechanical loading in individuals with and without transtibial amputation using MR images revealed that the soft tissue deformation was significantly higher ($p < 0.01$) in control limbs than residual limbs. Further, Within the individuals with amputation, deformation was significantly different between their residual and contralateral limbs at the lateral ($p < 0.01$) and posterior ($p < 0.05$) calf sites (Bramley et al. 2021).

Finger-tip palpation has been used to evaluate the state of tissues for centuries. Since the elastic properties for complex tissue compositions were not able to be attained qualitatively through the sense of touch using only fingers, researchers investigated about quantitative extraction of biological tissue elastic properties. (Aleky, Rao and Pandya 2019). Quantitative structural mechanical properties considered two parameters primarily: Young's modulus (ratio between longitudinal stress and strain) and shear modulus (ratio between transverse stress and strain), which were achieved by measuring the applied force and the corresponding deformation. Uniaxial tensile and compression tests were considered the gold standard for quantitative tissue characterization, as the tests were able to determine the relationship between stress and strain (Markowski 1991). Indentation probes (Griffin et al. 2016), tension applicators, compression applicators (Westwood 2001) and rotary shear applicators (Westwood 2003) can be considered as the traditional quantitative material characterization practices. These evaluation procedures are generally destructive, do not accommodate for on-site analysis. Further, they are only capable of simulating a uniaxial compression to an extent. Most of the testing techniques allow us to see the surface deformation. If the material was homogenous throughout the test specimen, then the internal deformation could be inferred based on the external deformation. Since the residual limb soft tissues are not homogenous and is included with different soft tissue types (muscles, skin, fat, etc.) with varying compositions, these evaluation procedures would not be suitable for obtaining data to estimate the material properties.

Since conventional mechanical testing methods are not included with the sufficient amount of spatial resolution, imaging techniques are often used for a more quantitative measurement. Imaging modalities including plain radiography, CT, MRI, and ultrasound are used in conjunction

with clinical examinations of biological tissues either by static or dynamic deformation. Subsequently deducing the resulting strain field through medical images, an inverse calculation is used to obtain the soft tissue material properties (Aleky, Rao and Pandya 2019). The study used MRI scans related to three patients, which were acquired separately while experiencing a series of four quasi-static, uniaxial compression tests; the pressures has been applied through an MRI compatible sphygmomanometer which covered most of the residual limb.

Through a series of MATLAB computations, the areas of the sphygmomanometer in contact with the residual limb soft tissues were measured as 476.45 cm^2 , 512.35 cm^2 , and 426.72 cm^2 for the three patients. The patient specific residual limb soft tissue material properties can be affected by the variation between the sphygmomanometer contact areas. Additionally, a substantial amount of time was also spent on the task of area computation as it was a lengthy and tedious process. The process of area calculation for a single patient included calculating the midpoints related to the triangulations in the residual limb mesh, calculating the level of deformation related to calculated midpoints, filtering the midpoints with a high level of deformation, locating the triangles related to the filtered midpoints, and calculating the area of located triangles. However, the time spent on the task could have been reduced if the uniaxial compression tests were performed through a technique which included a constant area of pressure application.

As indentation is a frequently used method to measure the material properties of soft tissues nondestructively, an MRI compatible indenter can be suggested to replace the MRI compatible sphygmomanometer (Lu and Zheng 2004). The commonly applied method for indentation of soft tissues involves the use of a spherical indenter. As the most significant concern was related to the constant area of pressure application, a rigid, flat-ended, and cylindrical indenter can be recommended for this study. Since the surface area of the indentation probe is significantly lower than the surface area covered by the sphygmomanometer, the pressures that were used initially in the study (30 mmHg , 60 mmHg , and 100 mmHg) would not be desirable. Indentation probe could be applied against multiple well-defined, even residual limb soft tissue areas with low

pressures and slow progression of pressures to achieve the medical images at uncompressed and compressed states.

CONCLUSION

The force-deflection plots achieved in the study indicated unique shapes for each patient confirming the discrepancies between the soft tissue material properties between patients. The obtained soft tissue deformations could aid substantially in biomechanical modelling of residual limb soft tissues. The study anticipates developing accurate computational models of the mechanical contact between the residual limb and encasing socket. Such models can aid current socket design and customization process in an effort to reduce the risk of tissue injury, to lessen the time, materials and workforce required for design and fabrication of a best-fit prosthetic socket, and to improve patient satisfaction rates. The study anticipates employing more patients in the future to understand the variability within the patient population.

REFERENCES

1. Alekya, B., Rao, S. and Pandya, H.J., 2019. Engineering approaches for characterizing soft tissue mechanical properties: A review. *Clinical Biomechanics*, 69, pp.127-140.
2. Alley, R.D., Williams, T.W., Albuquerque, M.J. and Altobelli, D.E., 2011. Prosthetic sockets stabilized by alternating areas of tissue compression and release. *J Rehabil Res Dev*, 48(6), pp.679-96.
3. Andrew, J.T., 2008. Transhumeral and elbow disarticulation anatomically contoured socket considerations. *JPO: Journal of Prosthetics and Orthotics*, 20(3), pp.107-117.
4. Andrews, K.L., Nanosand, K.N. and Hoskin, T.L., 2017. Determining K-levels following transtibial amputation. *Int. J. Phys. Med. Rehabil*, 5(2).
5. Balk, E.M., Gazula, A., Markozannes, G., Kimmel, H.J., Saldanha, I.J., Resnik, L.J. and Trikalinos, T.A., 2018. Lower limb prostheses: measurement instruments, comparison of component effects by subgroups, and long-term outcomes.
6. Bastas, G., 2019. Lower limb amputations. *Essentials of Physical Medicine and Rehabilitation. 4th ed. Philadelphia, PA: Elsevier*.
7. Behrendt, C.A., Sigvant, B., Szeberin, Z., Beiles, B., Eldrup, N., Thomson, I.A., Venermo, M., Altreuther, M., Menyhei, G., Nordanstig, J. and Clarke, M., 2018. International variations in amputation practice: a VASCUNET report. *European Journal of Vascular and Endovascular Surgery*, 56(3), pp.391-399.
8. Berger, A., 2002. How does it work? Magnetic resonance imaging. *BMJ: British Medical Journal*, 324(7328), p.35.
9. Bergström, J., 2015. Elasticity/hyperelasticity. *Mechanics of solid polymers: theory and computational modeling*, pp.209-307
10. Bramley, J.L., Worsley, P.R., Bader, D.L., Everitt, C., Darekar, A., King, L. and Dickinson, A., 2021. Changes in tissue composition and load response after transtibial amputation indicate biomechanical adaptation.

11. Cagle, J.C., Reinhall, P.G., Allyn, K.J., McLean, J., Hinrichs, P., Hafner, B.J. and Sanders, J.E., 2018. A finite element model to assess transtibial prosthetic sockets with elastomeric liners. *Medical & biological engineering & computing*, 56(7), pp.1227-1240.
12. Cheng, S., Marras, I., Zafeiriou, S. and Pantic, M., 2017. Statistical non-rigid ICP algorithm and its application to 3D face alignment. *Image and Vision Computing*, 58, pp.3-12.
13. Childers, W. and Wurdeman, S.R., 2015. Transtibial amputation: prosthetic management. *Atlas of Amputations and Limb Deficiencies: Surgical, Prosthetic, and Rehabilitation Principles. 4th Ed. Rosemont, IL: American Academy of Orthopedic Surgeons*, pp.493-508.
14. Colombo, G., Facoetti, G., Rizzi, C. and Vitali, A., 2013, November. Socket virtual design based on low cost hand tracking and haptic devices. In *Proceedings of the 12th ACM SIGGRAPH International Conference on Virtual-Reality Continuum and Its Applications in Industry* (pp. 63-70).
15. Cone Instruments, 2021. *MRI Conditional Sphygmomanometer - Cone Instruments*. [online] Coneinstruments.com. Available at: <<https://www.coneinstruments.com/mri-imaging-supplies/p/MRIConditionalSphygmomanometer/>> [Accessed 10 June 2021].
16. Cowie, C.C., Rust, K.F., Byrd-Holt, D.D., Gregg, E.W., Ford, E.S., Geiss, L.S., Bainbridge, K.E. and Fradkin, J.E., 2010. Prevalence of diabetes and high risk for diabetes using A1C criteria in the US population in 1988–2006. *Diabetes care*, 33(3), pp.562-568.
17. Dickinson, A.S., Steer, J.W. and Worsley, P.R., 2017. Finite element analysis of the amputated lower limb: a systematic review and recommendations. *Medical engineering & physics*, 43, pp.1-18.
18. Dillingham, T.R., Pezzin, L.E. and Shore, A.D., 2005. Reamputation, mortality, and health care costs among persons with dysvascular lower-limb amputations. *Archives of physical medicine and rehabilitation*, 86(3), pp.480-486.
19. Dillingham, T.R., Pezzin, L.E., MacKenzie, E.J. and Burgess, A.R., 2001. Use and satisfaction with prosthetic devices among persons with trauma-related amputations: a long-term outcome study. *American journal of physical medicine & rehabilitation*, 80(8), pp.563-571.

20. Dillon, M.P., Fortington, L.V., Akram, M., Erbas, B. and Kohler, F., 2017. Geographic variation of the incidence rate of lower limb amputation in Australia from 2007-12. *PLoS One*, 12(1), p.e0170705.
21. Edwards, M.L., 2002. Lower Limb Prosthetics. In *Clinician's Guide to Assistive Technology* (pp. 297-310). Mosby.
22. Engstrom, B. and Van de Ven, C. eds., 1999. *Therapy for amputees*. Elsevier Health Sciences.
23. Esquenazi, A. and Yoo, S.K., 2016. Lower limb amputations—Epidemiology and assessment. *PMR Knowledge Now*, 3.
24. Fatone, S. and Caldwell, R., 2017. Northwestern University Flexible Subischial Vacuum Socket for persons with transfemoral amputation-Part 1: description of technique. *Prosthetics and orthotics international*, 41(3), pp.237-245.
25. Foisneau-Lottin, A., Martinet, N., Henrot, P., Paysant, J., Blum, A. and André, J.M., 2003. Bursitis, adventitious bursa, localized soft-tissue inflammation, and bone marrow edema in tibial stumps: the contribution of magnetic resonance imaging to the diagnosis and management of mechanical stress complications. *Archives of physical medicine and rehabilitation*, 84(5), pp.770-777.
26. Fung, Y.C., 2013. *Biomechanics: mechanical properties of living tissues*. Springer Science & Business Media.
27. Gefen, A., 2009. Reswick and Rogers pressure-time curve for pressure ulcer risk. Part 2. *Nursing Standard (through 2013)*, 23(46), p.40.
28. Griffin, M., Premakumar, Y., Seifalian, A., Butler, P.E. and Szarko, M., 2016. Biomechanical characterization of human soft tissues using indentation and tensile testing. *Journal of visualized experiments: JoVE*, (118).
29. Hall, M.R., Lindsay, R. and Krayenhoff, M. eds., 2012. *Modern earth buildings: Materials, engineering, constructions and applications*. Elsevier.
30. Harker, J., 2006. Wound healing complications associated with lower limb amputation. *World Wide Wounds*, 9.

31. Highsmith, J.T. and Highsmith, M.J., 2007. Common skin pathology in LE prosthesis users. *Journal of the American Academy of PAs*, 20(11), pp.33-36.
32. Ikeda, A.J., Reisinger, K.D., Malkush, M., Wu, Y., Edwards, M.L. and Kistenberg, R.S., 2012. A priori alignment of transtibial prostheses: a comparison and evaluation of three methods. *Disability and Rehabilitation: Assistive Technology*, 7(5), pp.381-388.
33. Jia, X., Zhang, M. and Lee, W.C., 2004. Load transfer mechanics between trans-tibial prosthetic socket and residual limb—dynamic effects. *Journal of biomechanics*, 37(9), pp.1371-1377.
34. Jia, X., Zhang, M., Li, X. and Lee, W.C., 2005. A quasi-dynamic nonlinear finite element model to investigate prosthetic interface stresses during walking for trans-tibial amputees. *Clinical Biomechanics*, 20(6), pp.630-635.
35. Kelly, P., 2013. Solid mechanics part I: An introduction to solid mechanics. *Solid mechanics lecture notes*, pp.241-324.
36. Klute, G.K., Glaister, B.C. and Berge, J.S., 2010. Prosthetic liners for lower limb amputees: a review of the literature. *Prosthetics and orthotics international*, 34(2), pp.146-153.
37. Krajchich, J.I., Pinzur, M.S., Potter, B.K. and Stevens, P.M., 2018. Atlas of Amputations & Limb Deficiencies. Lippincott Williams & Wilkins.
38. Kröger, K., Berg, C., Santosa, F., Malyar, N. and Reinecke, H., 2017. Lower limb amputation in Germany: an analysis of data from the German Federal Statistical Office between 2005 and 2014. *Deutsches Ärzteblatt International*, 114(8), p.130.
39. Lacroix, D. and Patiño, J.F.R., 2011. Finite element analysis of donning procedure of a prosthetic transfemoral socket. *Annals of biomedical engineering*, 39(12), p.2972.
40. Lee, W.C., Zhang, M., Jia, X. and Cheung, J.T., 2004. Finite element modeling of the contact interface between trans-tibial residual limb and prosthetic socket. *Medical engineering & physics*, 26(8), pp.655-662.
41. Lin, C.C., Chang, C.H., Wu, C.L., Chung, K.C. and Liao, I.C., 2004. Effects of liner stiffness for trans-tibial prosthesis: a finite element contact model. *Medical engineering & physics*, 26(1), pp.1-9.

42. Linder-Ganz, E., Engelberg, S., Scheinowitz, M. and Gefen, A., 2006. Pressure–time cell death threshold for albino rat skeletal muscles as related to pressure sore biomechanics. *Journal of biomechanics*, 39(14), pp.2725-2732.
43. Long, I., 1975. Allowing normal abduction of femur in the above-knee amputations. *Orthotics and Prosthetics*, 29, pp.53-58.
44. Magomedov, I.A., Khaliev, M.S. and Elmurzaev, A.A., 2020, November. Application of Finite Element Analysis in medicine. In *Journal of Physics: Conference Series* (Vol. 1679, No. 2, p. 022057). IOP Publishing.
45. Mak, A.F., Zhang, M. and Boone, D.A., 2001. State-of-the-art research in lower-limb prosthetic biomechanics-socket interface: a review. *Journal of rehabilitation research and development*, 38(2), pp.161-174.
46. Manu, 2021a. Rigid ICP registration. *MATLAB Central File Exchange*. [online] Available at: <<https://www.mathworks.com/matlabcentral/fileexchange/40888-rigid-icp-registration>> [Retrieved 9 June 2021]
47. Manu, 2021b. Non-rigid ICP registration. *MATLAB Central File Exchange*. [online] Available at: <<https://www.mathworks.com/matlabcentral/fileexchange41396-nonrigidicp> > [Retrieved 9 June 2021]
48. Markowski, W., Bundesanstalt fuer Materialforschung und Pruefung (BAM), 1991. *Machine and method for uniaxial mechanical material testing*. U.S. Patent 5,005,424.
49. May, M., Hahn, S., Tonn, C., Engels, G. and Hochlenert, D., 2016. Decrease in (major) amputations in diabetics: a secondary data analysis by AOK Rheinland/Hamburg. *Journal of diabetes research*, 2016.
50. Molina, C.S. and Faulk, J., 2020. Lower extremity amputation. *StatPearls [Internet]*.
51. Oleiwi, J.K. and Ahmed, S.J., 2016. Tensile and Buckling of Prosthetic Pylon Made from Hybrid Composite Materials. *Engineering and Technology Journal*, 34(14 Part (A) Engineering).

52. Omid, E., Fuetterer, L., Mousavi, S.R., Armstrong, R.C., Flynn, L.E. and Samani, A., 2014. Characterization and assessment of hyperelastic and elastic properties of decellularized human adipose tissues. *Journal of biomechanics*, 47(15), pp.3657-3663.
53. Orendurff, M.S., Raschke, S.U., Winder, L., Moe, D., Boone, D.A. and Kobayashi, T., 2016. Functional level assessment of individuals with transtibial limb loss: evaluation in the clinical setting versus objective community ambulatory activity. *Journal of rehabilitation and assistive technologies engineering*, 3, p.2055668316636316.
54. Paternò, L., Ibrahimi, M., Gruppioni, E., Menciassi, A. and Ricotti, L., 2018. Sockets for limb prostheses: a review of existing technologies and open challenges. *IEEE Transactions on Biomedical Engineering*, 65(9), pp.1996-2010.
55. Pezzin, L.E., Dillingham, T.R., MacKenzie, E.J., Ephraim, P. and Rossbach, P., 2004. Use and satisfaction with prosthetic limb devices and related services. *Archives of physical medicine and rehabilitation*, 85(5), pp.723-729.
56. Physiopedia Contributors, 2020. *Lower Limb Prosthetic Sockets and Suspension Systems*. [online] Physiopedia. Available at: <https://www.physiopedia.com/Lower_Limb_Prosthetic_Sockets_and_Suspension_Systems#cite_note-:2-10> [10 February 2021].
57. Portnoy, S., Siev-Ner, I., Shabshin, N. and Gefen, A., 2011. Effects of sitting postures on risks for deep tissue injury in the residuum of a transtibial prosthetic-user: a biomechanical case study. *Computer methods in biomechanics and biomedical engineering*, 14(11), pp.1009-1019.
58. Portnoy, S., Siev-Ner, I., Yizhar, Z., Kristal, A., Shabshin, N. and Gefen, A., 2009. Surgical and morphological factors that affect internal mechanical loads in soft tissues of the transtibial residuum. *Annals of biomedical engineering*, 37(12), p.2583.
59. Portnoy, S., Yizhar, Z., Shabshin, N., Itzchak, Y., Kristal, A., Dotan-Marom, Y., Siev-Ner, I. and Gefen, A., 2008. Internal mechanical conditions in the soft tissues of a residual limb of a trans-tibial amputee. *Journal of biomechanics*, 41(9), pp.1897-1909.

60. Ramírez, J.F. and Vélez, J.A., 2012. Incidence of the boundary condition between bone and soft tissue in a finite element model of a transfemoral amputee. *Prosthetics and orthotics international*, 36(4), pp.405-414.
61. Rubin, G., Fischer, E. and Dixon, M., 1986. Prescription of above-knee and below-knee prostheses. *Prosthetics and orthotics international*, 10(3), pp.117-124.
62. Rusinkiewicz, S. and Levoy, M., 2001, May. Efficient variants of the ICP algorithm. In *Proceedings third international conference on 3-D digital imaging and modeling* (pp. 145-152). IEEE.
63. Rzymkowski, C., 2000. "Hybrid" Approach to Modelling of Biomechanical Systems. In *Human Biomechanics and Injury Prevention* (pp. 59-64). Springer, Tokyo.
64. Schoppen, T., Boonstra, A., Groothoff, J.W., de Vries, J., Göeken, L.N. and Eisma, W.H., 2003. Physical, mental, and social predictors of functional outcome in unilateral lower-limb amputees. *Archives of physical medicine and rehabilitation*, 84(6), pp.803-811.
65. Silver, F.H., Christiansen, D.L. and Buntin, C.M., 1989. Mechanical properties of the aorta: a review. *Critical reviews in biomedical engineering*, 17(4), pp.323-358.
66. Vélez Zea, J.A., Bustamante Góez, L.M. and Villarraga Ossa, J.A., 2015. Relation between residual limb length and stress distribution over stump for transfemoral amputees. *Revista EIA*, (23), pp.107-115.
67. Westwood, J.D. ed., 2001. *Medicine meets virtual reality 2001: outer space, inner space, virtual space* (Vol. 81). IOS Press.
68. Westwood, J.D. ed., 2003. *Medicine meets virtual reality 11: NextMed: health horizon* (Vol. 94). John Wiley & Sons.
69. Woo, S.L.Y., Gomez, M.A. and Akeson, W.H., 1985. Mechanical behaviors of soft tissues: Measurements, modifications, injuries, and treatment. *The biomechanics of trauma*, pp.107-133.
70. Wu, C.L., Chang, C.H., Hsu, A.T., Lin, C.C., Chen, S.I. and Chang, G.L., 2003. A proposal for the pre-evaluation protocol of below-knee socket design-integration pain tolerance with finite element analysis. *Journal of the Chinese Institute of Engineers*, 26(6), pp.853-860.

71. Zachariah, S.G. and Sanders, J.E., 2000. Finite element estimates of interface stress in the trans-tibial prosthesis using gap elements are different from those using automated contact. *Journal of Biomechanics*, 33(7), pp.895-899.
72. Zanaty, E.A. and Ghoniemy, S., 2016. Medical image segmentation techniques: an overview. *International Journal of informatics and medical data processing*, 1(1), pp.16-37.
73. Zhang, L., Zhu, M., Shen, L. and Zheng, F., 2013, July. Finite element analysis of the contact interface between trans-femoral stump and prosthetic socket. In *2013 35th annual international conference of the IEEE engineering in medicine and biology society (Embc)* (pp. 1270-1273). IEEE.
74. Zhang, M. and Roberts, C., 2000. Comparison of computational analysis with clinical measurement of stresses on below-knee residual limb in a prosthetic socket. *Medical engineering & physics*, 22(9), pp.607-612.
75. Ziegler-Graham, K., MacKenzie, E.J., Ephraim, P.L., Trivison, T.G. and Brookmeyer, R., 2008. Estimating the prevalence of limb loss in the United States: 2005 to 2050. *Archives of physical medicine and rehabilitation*, 89(3), pp.422-429.

APPENDICES

APPENDIX 1

```
[sourceTibia, f, n, stltitle] = stlread('PD_30_Tibia.stl');
```

```
[targetTibia, f, n, stltitle] = stlread('PD_0_Tibia.stl');
```

```
sourceTibiaF = sourceTibia.ConnectivityList;
```

```
sourceTibiaV = sourceTibia.Points;
```

```
targetTibiaF = targetTibia.ConnectivityList;
```

```
targetTibiaV = targetTibia.Points;
```

```
[sourceFlesh, f, n, stltitle] = stlread('PD_30_Flesh.stl');
```

```
[targetFlesh, f, n, stltitle] = stlread('PD_0_Flesh.stl');
```

```
sourceFleshF = sourceFlesh.ConnectivityList;
```

```
sourceFleshV = sourceFlesh.Points;
```

```
targetFleshF = targetFlesh.ConnectivityList;
```

```
targetFleshV = targetFlesh.Points;
```

```
%rigid icp
```

```
[error, sourceTibiaV2, transform] = rigidICP(targetTibiaV, sourceTibiaV);
```

APPENDIX 2

```
T_mat_rot = transform.T;  
T_mat_trans = transform.c;  
T_mat_trans = T_mat_trans(1,:);  
T_mat = [[T_mat_rot,T_mat_trans']; [0 0 0 1]];  
  
temp_nodes = sourceFleshV';  
temp_nodes(4,:) = 1;  
aligned_nodes = T_mat * temp_nodes;  
aligned_nodes = aligned_nodes(1:3,:);  
sourceFleshV2 = aligned_nodes;
```

APPENDIX 3

```
[registered]  
= nonrigidICP(sourceFleshV2,targetFleshV,sourceFleshF,targetFleshF,10,1)
```

APPENDIX 4

```
d = targetFleshV - registered;  
dsqrt = sqrt(d(:,1).^2 + d(:,2).^2 + d(:,3).^2);  
  
for i = 1:length(registered)  
    if d(i,1) < 0  
        dsqrt(i) = -1 * dsqrt(i);  
    end  
end
```

APPENDIX 5

```
connectsR = boundary(registered,0.95);  
xq = zeros(length(connectsR),3);  
  
for i = 1:length(connectsR)  
  
    a = registered (connectsR (i, 1),:);  
    b = registered (connectsR (i, 2),:);  
    c = registered (connectsR (i, 3),:);  
  
    xm = (a(1) + b(1) + c(1))/3;  
    ym = (a(2) + b(2) + c(2))/3;  
    zm = (a(3) + b(3) + c(3))/3;  
  
    xq(i,:) = [xm,ym,zm];  
  
end  
  
vq = griddatan(registered,dsqrt,xq,'nearest');
```

APPENDIX 6

```
vq_n = zeros(length(connectsR),1);
```

```
for i = 1:length(connectsR)
```

```
    if vq(i) > 3.0
```

```
        vq_n(i) = vq(i);
```

```
    end
```

```
end
```

APPENDIX 7

```
for i = 1:length(connectsR)
```

```
    if vq_n(i) == 0
```

```
        xq(i,1) = 0;
```

```
        xq(i,2) = 0;
```

```
        xq(i,3) = 0;
```

```
    end
```

```
end
```

```
xq = xq(any(xq,2),:);
```

```
vq_n = vq_n(any(vq_n,2),:);
```

APPENDIX 8

```
connectsR_n = zeros(length(connectsR),3);
```

```
for i = 1:length(connectsR)
```

```
    if vq_n(i)~ = 0
```

```
        connectsR_n(i,:) = connectsR(i,:);
```

```
    end
```

```
end
```

APPENDIX 9

```
A = zeros(length(connectsR_n),1);
```

```
for i = 1:length(connectsR_n)
```

```
    if connectsR_n(i,:)~= 0
```

```
        p = registered(connectsR_n(i,1),:);
```

```
        q = registered(connectsR_n(i,2),:);
```

```
        r = registered(connectsR_n(i,3),:);
```

```
        ons = [1 1 1];
```

```
        A(i) = 0.5 * sqrt(det([p(1) q(1) r(1); p(2) q(2) r(2); ons])^2  
            + det([p(2) q(2) r(2); p(3) q(3) r(3); ons])^2  
            + det([p(3) q(3) r(3); p(1) q(1) r(1); ons])^2);
```

```
    end
```

```
end
```

```
Area = sum(A,'all');
```